CAUSES AND CONSEQUENCES OF OFF-AXIS VOLCANISM ON THE EAST PACIFIC RISE 9°25'-9°57'N: IMPLICATIONS FOR THE RAPID THICKENING OF SEISMIC LAYER 2A

A THESIS SUBMITTED TO THE GRADUATE DIVISION OF THE UNIVERSITY OF HAWAI'I IN PARTIAL FULFILLMENT OF THE REQUIREMENTS FOR THE DEGREE OF

MASTER OF SCIENCE

IN

GEOLOGY AND GEOPHYSICS

MAY 2004

By
Tomoko Kurokawa

Thesis Committee:

Margo Edwards, Chairperson
Robert Dunn
Stephen Martel
Scott Rowland

ACKNOWLEDGEMENTS

First and foremost, I would like to thank my family and friends for their warm support and encouragement throughout my study abroad. I am grateful to the chief scientists of the AT7-4 cruise, Hans Schouten, Dan Fornari, and Maurice Tivey at Woods Hole Oceanographic Institution for inviting me on their research cruise and allowing me to use their dataset for my research. I would like to acknowledge the captain and crew of R/V *Atlantis* for their assistance in collecting invaluable data for my study. Special thanks to the AT7-4 scientific party and Hawaii Mapping Research Group at the University of Hawaii for the successful data acquisition and processing. I would like to deeply thank you my advisor Margo Edwards without whose guidance this research would not have been possible. I wish to express my gratitude to Stephen Martel for his patient guidance of my TWODD analyses. Scott Rowland, and Robert Dunn provided stimulating discussions from which this research greatly benefited. *Arigato gozaimasita.*

ABSTRACT

Eruptions at mid-ocean ridges, the linear submarine volcanic chains where Earth's new oceanic crust is created, are confined to a narrow region only a few hundred meters to a kilometers wide that is known as the neovolcanic zone. Whether eruptions occur outside of the neovolcanic zone, and how they contribute to the accretion of the oceanic crust, remains the subject of debate. Off-axis ridges or mounds largely covered with young-looking pillow flows, commonly called "pillow mounds", are considered the most compelling evidence of off-axis volcanism on the fast-spreading East Pacific Rise (EPR). DSL-120A sidescan sonar data collected on the EPR between 9°25' and 9°57'N show abundant large pillow mounds up to 2.5 km long outside of lobate-lava dominated regions that extend from the ridge axis to 1-3 km off-axis. Although small pillow mounds (<0.5 km long) have been observed within 0.5 km of the ridge axis, the distribution of off-axis pillow mounds becomes clear for the first time in the DSL-120A sidescan data. This dataset is the high-resolution (2 m) comprehensive map, which for the first time depicts the morphology of the EPR crest up to 4 km from the ridge axis over a portion of the ridge 60 km long.

To assess the likelihood that off-axis pillow mounds are produced by lava flows that erupt on the EPR flanks as opposed to within the neovolcanic zone, I conducted a mechanical analysis using a boundary element code based on displacement discontinuities for two-dimensional plane-strain analyses (TWODD). The TWODD simulations are built upon previous studies but implement a more plausible ambient stress field for the EPR. Results of the analysis suggest that two independent pathways of

magma from the axial melt lens (AML) are possible. One pathway originates from the center of the upper surface of the AML and reaches the seafloor at the ridge axis; the other initiates from the AML tips and intersects the ridge flank several kilometers off-axis.

TWODD-simulated eruption sites agree with sidescan sonar data showing that pillow mounds occur within a narrow (1.5-km wide) strip parallel to and a few kilometers away from the ridge axis. There are discrepancies in absolute distance between pillow mound locations and TWODD simulated eruption sites, which may be caused by factors not taken into the simulations, such as the heterogeneity of the oceanic crust.

Based on the TWODD results and observations from the DSL-120A sidescan data and near-bottom photographs, I developed a dual-pathway eruption model to explain how off-axis eruptions might contribute to the thickening of the extrusive layer in the oceanic crust. Episodic off-axis eruptions produce pillow mounds that stand high on the ridge flank a few kilometers off-axis while more frequent on-axis eruptions produce lower-relief lobate flows that pave the ridge flank. In this model on-axis eruptions occasionally produce long flows that travel a distance down the ridge flank until they are block by the off-axis pillow mounds, which results the flows to pond on the inward-facing side of the pillow mounds. While the accumulated flows and the pillow mounds are rafted away from the ridge axis by seafloor spreading, new pillow mounds are formed at approximately the same eruptive site, which again functions to block subsequent on-axis flows. The repetition of this process contributes to the rapid thickening of seismic layer 2A within a few kilometers from the ridge axis along the EPR at 9°-10°N.

TABLE OF CONTENTS

Acknowledgements iii

Abstract iv

List of Tables ix

List of Figures x

List of Plates xii

List of Codes xiii

List of Abbreviations xiv

Chapter 1: Introduction 1

Chapter 2: Data acquisition and processing methods 7

2.1 DSL-120A sidescan data 7

2.2 Micro-bathymetry data 10

2.3 Seafloor photographs and videos 10

Chapter 3: Characteristics and distribution of pillow mounds in the DSL-120A sidescan data and from near-bottom observations 13

3.1 Two types of pillow mound identified in sidescan data 14

3.2 Cross-sectional shapes of pillow mounds 15

3.3 Across-axis distribution of prominent volcanic and tectonic features 15

3.3.1 Observations from the field data 15

3.3.2 Statistical analysis 17

3.4 Along-axis distribution of volcanic and tectonic features 18

3.4.1 Observations from the field data 18

3.4.2 Statistical analysis..22

- Distribution of pillow mounds..22
- Terminations of lobate-dominated regions: Potential ponding of lava flows by inward-facing faults and pillow mounds..............24

Chapter 4: Off-axis eruption model for the formation of pillow mounds..............25

Chapter 5: Mechanical analysis..31

5.1 Conceptual model..32

5.2 Boundary element method..34

5.3 Ambient stress field..35

5.4 Sill and ambient stress field..40

5.5 Sill propagation..42

5.6 Simulations representing five locations in the study area....................44

5.7 Results and discussion..46

Chapter 6: Results and Discussion..50

6.1 Comparison and discussion of observational and TWODD results for the distribution of large pillow mounds..50

6.2 Dual-pathway eruption model for the rapid thickening of seismic layer 2A...53

6.3 Limitations of the dual-pathway eruption model....................................56

6.4 Recommendations for future investigations....................................58

Appendix A: Table..60

Appendix B: Figures..64

Appendix C: Plates.. 100

Appendix D: Codes..101

References 123

LIST OF TABLES

Table Page

1. Values for TWODD simulations.. 61

2. Dimensions and geometry of the axial melt lens used in TWODD simulations... 62

3. Characteristics of two types of pillow mounds observed in the study area........... 63

LIST OF FIGURES

Figure Page

1. Map showing the location of the study area.. 74

2. Representative photographs of lava flow morphologies in the study area........ 75

3. Interpretative cross-sectional diagram of layers constructing the oceanic crust and the magma reservoir... 76

4. Across-axis profiles of the thickness of seismic layer 2A........................ 77

5. Photographs of survey instruments used for the AT7-4 cruise 78

6. Schematic diagram showing the sonar signal path of DSL-120A................. 79

7. Map showing survey boundaries of DSL-120.. 80

8. Plot for the basal diameter of pillow mounds verses pillow mound location.... 81

9. Cross-sectional shapes of pillow mounds.. 82

10. DSL-120A sidescan data showing changes of across-axis seafloor morphology changes.. 83

11. Histogram showing the across-axis distribution of pillow mound................ 84

12. Summary maps for small-pillow mounds at the 9°37'N area on the EPR....... 85

13. Summary maps for R4 (9°34'-26'N) on the EPR.................................. 86

14. Histogram showing the along-axis distribution of pillow mounds............... 87

15. Schematic diagram of the formation of pillow mounds by dike intrusion 88

16. Interpretative and conceptual models of magma reservoir for the EPR and the reference frame used in TWODD analysis.. 89

17. Diagram showing mantle convection currents at the base of the crust.......... 90

18. Ambient stress fields induced by two sets of the far-field stress.................... 91

19. Normal and shear basal tractions for the crust with a uniform and non-uniform thickness. 92

20. Stress fields induced by the far-field stresses and a pressurized sill.............. 93

21. Diagram showing effects of the free surface on to a opening of a pressurized sill and parameters used in Chapter 5.5.. 94

22. Stress fields induced by the far-field stresses and a propagating pressurized sill 95

23. Three possible eruption pathways from the AML to the seafloor................. 97

24. Different ambient stress fields for the simulations discussed in Chapter 5.7.... 98

25. Diagram showing the dual-pathway eruption model producing the rapid thickening of seismic layer 2A on the EPR.. 99

LIST OF PLATES

Plate

1. DSL-120A sidescan data and interpretative maps on the EPR 9°25'-9°58'N

....Placed in the back pocket

LIST OF CODES

Code		Page
1.	Body forces and Hafner's basal traction	102
2.	Inserting a pressurized sill	103
3.	Propagating a sill	105
4.	TWODD	108
5.	Base data	119
6.	Other functions	120

LIST OF ABBREVIATIONS

1. ABE – Autonomous Benthic Explorer
2. AML– axial melt lens
3. AST – axial summit trough
4. AT7-4 – R/V Atlantis, Leg 7-4, cruise to East Pacific Rise 9°25'-58'N to collect DSL-120A sidescan data, 2001
5. DSL-120A – a 120 kHz near-bottom side-looking sonar system
6. (N/S) EPR – (North/South) East Pacific Rise
7. JdFR – Juan de Fuca Ridge
8. MOR – mid-ocean ridge
9. R/V – research vessel
10. TWODD– two-dimensional, plane-strain boundary element code
11. WHOI – Woods Hole Oceanographic Institution

CHAPTER 1: INTRODUCTION

The East Pacific Rise (EPR) 9°-10°N is a fast-spreading mid-ocean ridge (MOR) between the Pacific and Cocos plates that has been intensively studied in the last twenty-five years [Figure 1; e.g., *Macdonald et al.,* 1980; *Spiess,* 1980; *Haymon,* 1983, 1993; *Von Damm, et al.,* 1995; *Fornari et al.,* 1998]. The area discussed in this thesis is located between 9°25' and 9°57'N, where the full-spreading rate is 110 mm/year [*Klitgord and Mammerick*, 1982; *Carbotte and Macdonald*, 1992]. This rate has been essentially constant, and spreading symmetric with respect to the ridge axis, for the last 2 my. Across-axis bathymetric profiles of the ridge show a topographic high with a narrow trough at the summit that I refer to as the axial summit trough (AST) following the recent nomenclature of Perfit and Chadwick [1998]. In the study area the AST is less than 200 m wide and is bounded by walls less than 15 m high [*Fornari et al.*, 1998]. It is considered to be a neovolcanic zone where eruptions and high-temperature hydrothermal discharge are concentrated [*Perfit and Chadwick*, 1998]. For this reason, it has been the main locus of studies during the past twenty-five years.

Near-bottom observations from submersible dives and deep-towed camera systems have been used to study the morphological distribution of lava within the AST and on the seafloor as far as 2 km from the ridge axis [*Kurras et al.*, 2000; *Engels et al.*, 2002; *White et al.*, 2002]. Submarine lava flow morphologies are generally categorized into three types: sheet, lobate, and pillow flows [Figure 2; *Perfit and Chadwick*, 1998]. Sheet flows spread out as a continuous sheet during their formation and are generally thin (< 6 cm) with low vertical relief [*Chadwick et al.*, 1999]. In contrast, lobate flows form by budding from the flow front and then inflating upwards, producing terrain with undulating relief of <1 m. Pillow flows grow by being slowly squeezed through a small breakout, which produces the characteristic "toothpaste striations" that form parallel to the direction of flow [*Moore*, 1975]. Individual pillows are typically elongated by one to several meters with a diameter of 0.5-1.0 m [*Ballard and Moore*, 1977]. The floor of the AST is predominantly covered with sheet flows, while the seafloor outside the AST is largely paved with lobate flows [*Kurras et al.*, 2000; *Engels et al.*, 2002; *White et al.*, 2002]. Pillow flows are hardly observed within the AST but are found on the seafloor >200 m from the ridge axis. Some of these pillow flows are observed covering mounds 130±50 m long on the seafloor 200-500 m away from the ridge axis [*White et al.*, 2002].

Magma erupting at the AST originates from a reservoir below the ridge crest. Based on geophysical and petrological evidence, Sinton and Detrick [1992] describe the magma reservoir at the EPR as a thin and narrow melt lens, which is referred to as the axial melt lens (AML; Figure 3) by Kent et al. [1994]. The AML is typically less than 1.5 km wide across the ridge axis and 10 to 50 m thick [e.g., *Kent et al.*, 1993]. Sinton and Detrick [1992] suggest that it overlies a partially solidified mush zone 1-2 km below the seafloor. The AML and the mush zone are flanked by a mostly solidified region within the gabbroic layer called the transition zone. The AML is detected underneath the EPR axis throughout the region discussed in this thesis [*Detrick et al.*, 1987].

Although the AML is continuous along the ridge in the study area, bathymetric maps show that the ridge topography consists of multiple discrete ridges and discontinuity zones. Macdonald et al. [1991] divided these ridges into four orders of segmentation according to their morphological characteristics, the presence or absence of an AML, geochemical anomalies, and the distribution of hydrothermal vents systems. The first order, the largest scale, includes segments bounded by transform faults, while the second to fourth order segments are bounded by overlapping spreading centers (OSCs) with offsets of 2-30 km, OSCs with offsets of 0.5-2.0 km, and axial summit calderas with offsets of <1 km, respectively. According to this segmentation scheme, the study area described in this thesis covers two full and one partial third-order segments, which are considered to be the smallest segments with a unique magmatic system (Plate 1b).

Different levels of volcanic activity have been observed along the 60 km of the study area. The most volcanically active region recently is centered around 9°50'N [e.g., *Haymon et al.*, 1991; 1993]. Using the *Argo* 100 kHz sonar in 1989, Haymon et al. [1991] documented that this region contained the largest number of high-temperature hydrothermal vents ever mapped. Subsequent submersible surveys conducted in 1991 discovered seafloor phenomena indicating a recent volcanic eruption [*Haymon et al.*, 1993]. In contrast, the terrain at 9°30'N is considered to have been inactive over a longer time period [e.g., *Schouten et al.*, 2002].

While it is generally accepted that most eruptions on the EPR occur along the AST, strong indications of off-axis volcanism have been reported from submersible dives [e.g., *Perfit et al.*, 1994; *Macdonald et al.*, 1996]. The most prominent evidence of off-axis eruptions comes from ridges or mounds largely covered with pillow flows that appear darker, glassier and less altered than lava on the surrounding seafloor. These mounds are up to 20 m high and located a few kilometers from the AST. They are termed "pillow mounds" in this study, following the convention of Chadwick and Embley [1994] and Perfit and Chadwick [1998]. Since pillow flows rarely occur in the AST [*Kurras et al.*, 2000; *Engels*, 2001; *White et al.*, 2002], it is unlikely that these pillow mounds form at the ridge axis and then spread to off-axis regions [*Fialko*, 2001; *White et al.*, 2002]. Schouten et al. [2002] propose that pillow mounds form as a result of changes in lava morphology at the distal ends of flows when the magma supply rate declines during the waning stages of an eruption. However, the strong associations of the pillow mounds with ridge-parallel faults [*Goldstein et al.*, 1994; *Perfit et al.*, 1994], as well as the presence of a near-surface off-axis dike detected during a near-bottom gravity survey [*Cochran et al.*, 1999], favor the genesis of pillow mounds by off-axis eruptions. Perfit et al. [1994] present a model that suggests dikes originating from the upper surface of an AML may erupt anywhere on the ridge flank. Fialko [2001] conducted a mechanical analysis to constrain physical mechanisms for the off-axis eruption process. His results show that a dike eruption on the ridge flank can begin at the tips of an AML and propagate in a parabolic trajectory, reaching the seafloor several kilometers from the AST. Gently dipping dikes observed at the Oman ophiolite [*Pollard and Johnson*, 1973; *Francis*, 1982] may correspond to the pathways described in Fialko's [2001] theoretical study.

Pillow mounds formed by off-axis eruptions may contribute to the observed rapid increase in thickness of the oceanic crust near MORs. Seismic studies of the EPR 9°-10°N have detected discrete velocity changes that bound four layers within oceanic crust [*Houtz and Ewing,* 1976; *Rosendahl et al.*, 1976; *Herron,* 1982]. By comparing the depth and thickness of these seismic layers with field observations at ophiolites, the seismic layers have been interpreted to correspond to different lithologic layers. From seafloor surface to ~5 km depth these layers are: a sediment layer (layer 1A), an extrusive volcanic layer (layer 2A), a sheeted dike (layer 2B), and a gabbroic layer (layer 3) [Figure 3; *Houtz and Ewing,* 1976; *Talwani et al.,* 1976]. The thickness of seismic layer 2A varies both along and across the ridge axis [*Harding et al.*, 1993; *Kent et al.*, 1994; *Vera and Diebold*, 1994; *Christeson et al.*, 1996]. Along the EPR axis, the thickness of layer 2A axis is fairly constant, ranging between 150 m and 250 m. The thickest crust along-axis generally is observed at locations with the most robust magmatic activity. In contrast, across-axis seismic profiles show that the thickness of layer 2A increases rapidly, doubling over a distance of 2-3 km in the off-axis direction (Figure 4). Many models have been developed to explain the rapid thickening of layer 2A [*Christeson et al.*, 1992; *Harding et al.*, 1993; *Hooft et al.*, 1996; *Christeson et al.*, 1996]. One group of models propose that the increase in layer 2A thickness results from long lava flows traveling from the ridge axis or from off-axis eruptions [*Christeson et al.*, 1992; *Harding et al.*, 1993; *Hooft et al.*, 1996]. Another model predicts a reduced buoyancy force associated with the AML away from the ridge axis and suggests that the smaller subsidence of layer 2A compared to layer 2B causes the observed increase of layer 2A thickness [*Christeson et al.*, 1996].

In this thesis I investigate the causes and consequences of off-axis eruptions at the EPR 9°-10°N to constrain the processes responsible for the rapid thickening of the seismic layer 2A. I study the distribution of pillow mounds using the first comprehensive, high-resolution sidescan sonar dataset for the EPR between 9°25' and 9°57'N that has significant coverage both inside and several kilometers outside of the AST. I supplement the sidescan data with bathymetry and near-bottom images collected using deep-towed camera systems and the DSL *Alvin* to examine the off-axis eruption model of the pillow mounds. Finally, I simulate the stress field in the oceanic crust using the boundary-element method [*Crouch and Starfield*, 1983]. The simulation is built upon the previously conducted studies [*Pollard and Hozhausen*, 1979; *Fialko*, 2001] but implements a more plausible ambient stress field. My results show that a combination of eruptive processes, occurring at the axis and on the flank of the EPR 9°-10°N, contribute to the rapid thickening of the seismic layer 2A within a few kilometers from the ridge axis.

CHAPTER 2: DATA ACQUISITION AND PROCESSING METHODS

Three datasets from R/V *Atlantis* Voyage 7, Leg 4 (AT7-4) collected in November-December 2001 [*Schouten et al.*, 2001] were analyzed along with supplemental video images and photographs from previous surveys to investigate the distributions and morphology of pillow mounds. Sidescan sonar data acquired by the DSL-120A (Figure 5a) provide a regional perspective of the pillow mounds and surrounding tectonic and volcanic features. Where possible, the sidescan data were checked against by co-registered photographs taken from the camera surveys. Micro-bathymetry data collected using the Autonomous Benthic Explorer (ABE; Figure 5b) provide detailed topography of two representative ridge regions; a region of high volcanic activity around 9°50'N and crestal terrain around 9°30'N with less recent volcanism [*Haymon et al.*, 1993; *Fornari et al.*, 1998]. SeaBeam bathymetry data [*Cochran et al.*, 1999] provide a broader regional context for the topography and locations of large-scale pillow mounds.

2.1 DSL-120A Sidescan Data

A 60.5 x 6.8 km sidescan mosaic of the EPR crest between 9°25'N and 9°57'N was constructed from DSL-120A data collected during the AT7-4 cruise [*Schouten et al.*, 2001, 2002]. The DSL-120A is a 120 kHz deep-towed, near-bottom sonar system with new phase-bathymetry data collection capability relative to the older DSL-120 system [Figure 5a; *Scheirer et al.*, 2000]. The sidescan sonar system produces records of seafloor morphology variations from differences in intensity of the returned acoustic echo [Figure

6; Geyer, 1991]. In this study light and dark grays represent high and low signal returns, respectively. During the survey the system was towed at speeds of 1.0-1.7 knots at ~100 m above the ocean floor. Sonar swaths are ~1 km wide (Figure 6) and oriented sub-parallel to the ridge axis (Figure 7). Where the DSL-120A survey overlapped the ABE survey regions, (9°50'N and 9°28'-29'N, Figure 7), navigation was accomplished with bottom-moored transponders. The remaining portions of the survey lines were navigated using a layback scheme employing acoustic travel time, wire out, and ship position. Navigational corrections for the DSL-120A data were made by shifting some of the DSL-120A track lines a few tens of meters [*Schouten et al.*, 2001]. Comparison of the DSL-120A data with *Argo I* 100 kHz sidescan data collected in 1989 [*Haymon et al.*, 1991; *Fornari et al.*, 1998] demonstrates a high level of morphological correlation between the two datasets. The micro-bathymetry and photographs collected during the AT7-4 cruise show navigational accuracy of ~5 m [*Schouten et al.*, 2001].

Sidescan images gridded at 2 m resolution and plotted at a scale of 1:10,000 were used to identify tectonic and volcanic features based on their acoustic contrast with the surrounding seafloor. Due to the strong specular return directly under the DSL-120A (e.g., at the sonar nadir), areas within 100 m of nadir were not interpreted except in the context of surrounding terrain. In the sidescan data faults appear as approximately ridge-parallel linear acoustic echoes of uniform intensity. With a high length to width ratio, faults may display high or low reflectivity depending on the orientation of the scarp with respect to the insonification direction; faults bounding grabens and horsts display a pair of high and low backscatter lineations indicating either a depression or a topographic high between the lineations. The length of faults varies from less than 100 m to 8 km. I mapped no faults shorter than 200 m unless they were associated with pillow mounds.

Individual pillow mounds in the sidescan data typically have circular to oval shapes. Like horsts or graben, pillow mounds exhibit acoustic contrast resulting from a strong reflection on the side of the mound that faces toward the sonar and an acoustic shadow on the side of the mound facing away from the sonar nadir. Individual pillow mounds (50-300 m in length and less than 30 m in height) often cluster to form larger elongated mounds (300-2,000 m in length and 30-80 m in height). The size of a pillow mound is defined by the perimeter of a coalesced or isolated mound.

To provide a reference point for the observed pillow mounds, the location of the ridge axis was identified in the DSL-120A sidescan data. The discrete lines of irregular acoustic shadows were interpreted as the ASCT, and its boundaries were defined by comparisons to previous interpretations based on the *Argo I* sidescan imagery from 1989 [*Fornari et al.*, 1990, 1998].

After interpreting the sidescan data charts, the ASCT, pillow mounds, and faults were digitized and interpretative maps were generated using the Generic Mapping Tools (GMT) program [Plate 1b; *Wessel and Smith*, 1991]. The extent of pillow mound coverage was calculated from these interpretative maps using the Environment for Visualizing Images (ENVI) program [*Research Systems, Inc.*, 2004]. The areal values used in the analysis are the minimum total area covered by the pillow mounds to account for errors resulting from boundaries blurred during the digitizing process.

The interpretative maps were compared with the ABE micro-bathymetry and SeaBeam bathymetry to estimate height ranges of large-scale pillow mounds, fault scarps, and graben and horst structures within the context of local and regional topography (Plate 1b). Although the grid cell size of SeaBeam (25-75 m; vertical resolution of 10-20 m) is much higher than the grid cell size of the DSL-120A (2 m; vertical resolution of 1-2 m), the comparison provides a useful regional context.

2.2 Micro-Bathymetry Data

During the AT7-4 cruise, micro-bathymetry data were collected by ABE [*Yoerger et al.*, 1999] at the 9°50'N and 9°28'-29'N sites (Figure 7). ABE is an autonomous underwater vehicle that has the ability to follow pre-programmed tracklines over rough terrain using bottom-following algorithms [Figure 5b, *Yoerger et al.*, 1999]. It acquired data for bathymetry, the magnetic field, temperature, and salinity for 327 km of trackline in 11 dives covering a total area of ~14.3 km^2 [*Schouten et al.*, 2001; Figure 7]. Bottom-moored transponders were used to navigate ABE, which surveyed at 20-30 m above the seafloor with 40-60 m line spacing. ABE bathymetry data were gridded at its optimal values: 5 m grid cells contoured at 1 m vertical intervals.

2.3 Seafloor Photographs and Videos

Digital photographs from the AT7-4 cruise were supplemented with visual imagery collected from three previously conducted camera and *Alvin* surveys of the pillow mounds identified on the DSL-120A sonar data.

During the AT7-4 cruise, 14 lines were surveyed with the Woods Hole Oceanographic Institution (WHOI) towed camera system in the 9°50'N and 9°29'N areas where the ABE surveys were conducted (Figure 7). This system was built for the AT7-4 cruise and consists of a modified Aquapix digital camera and a 12 kHz pinger to measure the distance above the seafloor [Figure 5c; *Schouten et al.*, 2001]. The camera system was towed at a speed of 0.2 – 0.5 knots and ~5-7 m above the seafloor as determined from the 12 kHz pinger trace. Lines 1 through 10 were navigated using bottom-moored transponders with an observed offset between camera and ship of 100-550 m. Lines 11 through 14 were navigated using layback in combination with P-Code GPS ship navigation. Digital photographs were taken every 15 seconds. At 5 m above the seafloor, each frame covers ~4.8 by 6.4 m of seafloor along the track. This approach yielded 80-100% ground coverage, with a maximum of 1-2 m spacing between images [*Kurras et al.,* 2000]. Lava observed in the photographs was categorized into three major types, pillow, lobate, and sheet (Figure 2). Relevant tectonic features such as faults and fissures were noted and geographically co-registered on the DSL-120A sidescan data to provide a more detailed context for the local topography around pillow mounds.

Digital photographs of pillow mounds between 9°53'-54'N, 1 km east of the ridge axis, were collected during R/V *Atlantis* Voyage 3, Leg 34 (AT3-34) in May 1999 (Figure 7) using a previous version of the Woods Hole Oceanographic Institution Towed Camera System [*Fornari et al.*, 1998]. The system was navigated using P-Code GPS ship navigation and towed at 0.5 knots ~5-7 m above the seafloor as determined from the 12 kHz pinger trace. Digital photographs were taken every 15 seconds and covered 4 by 6 m of seafloor along the track [*Kurras et al.*, 2000]. These photographs were analyzed using the same method as photos from the AT7-4 cruise.

Video images of smooth and bulbous pillow mounds within 500 m of the ASCT around 9°37'N were collected during DSV *Alvin* dives 3525 and 3528 in 2000 (Figure 7).

The submersible traversed the region at an average speed of 0.5 knots 5-8 m above the seafloor. Using a long-baseline transponder net combined with bottom-lock Doppler sonar, navigation for the dives had a relative positional accuracy of 1-2 m [*Engels et al.*, 2003]. Video images were sampled every 15 seconds and analyzed for lava type.

Interpretations regarding for the pillow mounds in the area of 9°30.5'-32'N on the east flank of the EPR were checked using video imagery and transcripts recorded during DSV *Alvin* dives 2489 and 2495 in 1992 (Figure 7). The navigation for these dives was not accurate enough to confidently correlate the *Alvin* data with features observed on the DSL-120A sidescan imagery; therefore, this dataset was used with careful consideration to investigate only large, prominent features depicted in the data.

CHAPTER 3: CHARACTERISTICS AND DISTRIBUTION OF PILLOW MOUNDS IN THE DSL-120A SIDESCAN DATA AND FROM NEAR-BOTTOM OBSERVATIONS

The DSL-120A sidescan data collected during the AT7-4 cruise imaged the EPR crest, extending as far as 3.5 km west of the AST on the Pacific plate and 4.0 km east on the Cocos plate from 9°25'-57'N (Figure 7). These data comprise the first high-resolution (2 m) comprehensive sidescan coverage of the region outside of the neovolcanic zone [*Schouten et al.*, 2001]. The data reveal distinct across- and along-axis changes in seafloor morphology. In particular, the distribution of pillow mounds becomes clear for the first time: large pillow mounds are more common a few kilometers off-axis than close to the axis (Plate 1). The areal coverage of pillow mounds in the study area is approximately 4% (12.8 km^2 of the 356.7 km^2 total area surveyed).

In this chapter I first describe the morphological characteristics of two types of pillow mounds including the plan-view shapes depicted in sidescan data as well as the cross-sectional shapes depicted in ridge-perpendicular bathymetric profiles from *Alvin* altimeter data and SeaBeam bathymetry. I then discuss across- and along-axis seafloor morphology changes, focusing on pillow mound distribution. Near-bottom images from deep-towed camera systems and *Alvin* dives are used to identify the lava morphology. The purpose of this analysis is to document whether pillow mound morphology or distribution varies systematically to constrain models for their formation.

3.1 Two types of pillow mounds identified in the sidescan data

Pillow mounds are identified in the sidescan data as individual mounds or groups of mounds or ridges that exhibit smooth to bulbous textures in different sizes. The smallest individual pillow mounds are circular to oval in plan view with basal diameters of ~50-300 m. Pillow mounds with basal diameters less than 200 m generally display strong acoustic contrast that produce bulbous textures whereas those with basal lengths >200 m exhibit a more uniform acoustic appearance. Mounds with both bulbous and smooth textures occur as isolated constructs but typically coalesce to form oval structures as long as 1 km or elongate linear ridges as long as 2.5 km with their long axes trending sub-parallel to the AST. Isolated and coalesced pillow mounds commonly occur in linear groups that align nearly parallel to the AST and reach lengths to 10 km long. Pillow mounds may overprint or be incised by nearly ridge-parallel faults and grabens.

In general, the size of pillow mounds increases with increasing distance from the AST (Figure 8). Based on their basal diameter, I have classified pillow mounds in two categories: small- and large-scale pillow mounds. Small-scale pillow mounds have basal diameters $\leqq$0.5 km, heights of 10-30 m and are observed from as little as 0.2 km away from the AST in the survey region. Large-scale pillow mounds have basal diameters of between 0.5 and 2.5 km, heights of 20-80 m and occur only at distances greater than 1.5 km from the AST.

3.2 Cross-sectional shapes of pillow mounds

Pillow mounds show two types of ridge-perpendicular bathymetric profiles in SeaBeam bathymetry and *Alvin* altimeter data. Type-1 profiles are relatively symmetric and dome shaped (Figure 9a); Type-2 profiles are characterized by a one-sided slope that faces away from the AST (Figure 9b). Both profile types have widths <500 m, but Type 1 have a lower relief (10-30 m) than Type 2 (20-80 m). Pillow mounds with Type-2 profiles are more common in the study area, thus, in this thesis if a pillow mound is described without profile information, it has a Type-2 profile.

3.3 Across-axis distribution of prominent volcanic and tectonic features

The sidescan data display a variety of volcanic and tectonic features in the study area. This section describes the most prominent features including the AST, a near-axis region dominated by lobate lava flows, lava channels, large inward-facing faults, and pillow mounds. The morphological descriptions are followed by a statistical analysis of pillow mound distribution.

3.3.1 Observations from the field data

A nearly continuous cluster of thin lineations located approximately in the middle of the survey area and striking (Figure 10) ~352° throughout most of the survey area are interpreted to be the AST (Plate 1b). The inferred location of the AST in the sidescan data was confirmed using previously collected datasets [Haymon et al., 1993; Fornari et al., 1998; *Schouten et al.,* 2002] and photographic images.

Outside of the AST, to distances of 1.5-3.0 km on either plate, the sidescan data display overlapping terraces with uniform medium reflectivity, bounded by curvilinear edges that exhibit stronger reflectivity (Figure 10) on the side of the terrace farthest from the AST. Relief of these terraces is as low as 1 m based on ABE bathymetric data. The terraces may be up to 400 m wide along-axis and 300 m long across-axis. The outermost terraces are, in places, terminated by large inward-facing faults (>15 m high) characterized by uniform high or low reflectivity lineations (Figure 10). In other locations, the terraces overprint lineations so that this terrain stretches without interruption from the AST to the base of large-scale pillow mounds or to the edge of the survey area [*Schouten et al.*, 2001; 2002]. Photographic images show that the terraces are covered by lobate flows, and the curvilinear edges correspond to flow fronts. This terraced terrain is henceforth referred to as the lobate-dominated region.

Within the lobate-dominated region, abundant low reflectivity features are observed (Figure 10). The low reflectivity features occur between 0 and 2.5 km from the AST. From photographic images, some of these features are identified as ~1 m deep lava channels floored by sheet flows. Some of the channel floors are exposed due to the collapse of its roof and pieces of collapsed roof are often found at the edge of the channel floor. The largest channel features are ~500 m long and ~100 m wide.

The seafloor outside of the lobate-dominated region displays mostly lower reflectivity and near-bottom images show that the seafloor in these areas has a thicker sediment cover (Figure 10). Ridge-parallel faults and both small- and large-scale mounds become abundant in this area.

3.3.2 Statistical analysis

Statistical analysis was used to quantify the abundance of pillow mounds depicted in the sidescan data as a function of distance from the AST. The surveyed region was divided into fifteen 500 m-wide corridors parallel to the AST, from the AST to the edges of the survey area. The northernmost 9 km of the surveyed area does not have an AST [*Haymon et al.*, 1991] so the reference point there is defined relative to the projected position of the AST. Pillow mound coverage is expressed as a percentage of the total area within each corridor. Percent coverage was used instead of the number of pillow because (i) the area within each 500 m corridor is not constant due to the survey geometry, (ii) pillow mound sizes differ significantly, and (iii) some pillow mounds are only partially mapped due to the survey boundaries.

The surveyed region extends from the AST as far as 3.5 km west on the Pacific plate and 4.0 km east on the Cocos plate (Figure 11). The average area covered by pillow mounds on the Pacific and Cocos plates is 3.8% and 6.2%, respectively. This difference is most likely a function of survey geometry. If the 3.5-4.0 km bin on the Cocos plate is excluded to make the off-axis distances the same for both plates, the average for the Cocos plate drops to 3.6%. On the Pacific plate, the abundance of pillow mounds increases significantly from 0.7% in the 0-0.5 km bin, to 3.6% in the 2.5-3.0 km bin, to 17.6% in the 3.0-3.5 km bin. Pillow mound abundance on the Cocos plate also increases but more irregularly from 0.17% in the 0-0.5 km bin, to 3.35% in the 1.5-2.0 km bin, to 8.95% in the 3-3.5 km bin, and 28.2% in the 3.5-4.0 km bin (Figure 11). The overall increase in number of pillow mounds observed with increasing distance from the AST on both the Pacific and Cocos plates suggests the mounds form at a few kilometers distance from the EPR axis.

3.4 Along-axis distribution of volcanic and tectonic features

The distributions of volcanic and tectonic features within the survey area vary with latitude on the Cocos and the Pacific plates. The survey area was divided into four regions (R1 to R4; Plate 1b) for the purpose of describing the how the distribution of pillow mounds and the extent of the lobate-dominated region change as a function of latitude (Plate 1b). This division reflects the 3rd order segmentation defined by Macdonald et al. [1998] and White et al. [2002]; according to their definitions, this study area covers two full and one partial 3rd-order segments and three 3rd-order OSCs (Plate 1b). Descriptions of the along-axis variations in seafloor morphology are followed by statistical analysis of the along-axis pillow mound distribution and the boundary types of the lobate-lava dominated region.

3.4.1 Observations from the field data

The northernmost region (R1) of the dataset used to analyze along-strike variations consists of the northern 15% of the study area (9 km) between 9°58'-53'N (Plate 1b). This region is defined as a 3rd-order OSC by the lack of an AST [OSC-1 on Plate 1b, *Macdonald et al.*, 1998; *White et al.*, 2002]. This region shows an extensive lobate-dominated region on the Pacific plate and abundant pillow mounds on the Cocos plate. The seafloor on the Pacific plate within R1 is almost completely covered by lobate flows from the AST to the western boundary of the surveyed area at 3.5 km. Three small-scale pillow mounds are located at 0.5 km from the AST (Plate 1); these pillow mounds are incised by grabens and faults. White et al. [2002] described these pillow mounds as smooth convex-upward hemispherical domes with an average width of 130±50 m and height of 20±10 m.

In contrast to the rare occurrence of pillow mounds on the Pacific plate, two groups of large-scale pillow mounds are observed at distances of 2 and 3 km from the AST on the Cocos Plate. The inner group is composed one small- and three large-scale pillow mounds all of which have Type 1 profiles rising as much as 30 m higher than the ridge crest. A graben <50 m wide bisects the northern half of the northernmost mound; the rest of the pillow mounds are not dissected. The outer group of mounds is composed of several small- and large-scale pillow mounds. Faults are scarce near this group until ~200 m east of the pillow mounds where the faults are overprinted by some of the small mounds.

R2 is located between 9°53'-44'N (Plate 1b) and represents one of the three 3rd order segments in the study area. This area contains the most prominent terrace shaped lobate flow fronts displayed in the sidescan data (Figure 10). On the Pacific plate the lobate-dominated region extends 1.5-2.0 km off-axis to the base of the first major inward-facing faults, but on the Cocos plate the boundary of the lobate-dominated terrain is ambiguous due to the quality of the sonar data, which was compromised due to system noise along one swath in this region. Pillow mounds within 3 km of the axis are absent except for one pair of mounds located 1.5 km off-axis at 9°45'N on the Pacific plate. A graben is located the western sides of these mounds. On the Pacific plate, small- and large-scale mounds are found >3 km from the axis and most of them overprint faults. On the Cocos plate, one large- and three small-scale pillow mounds are observed in the sedimented area ~3 km off-axis from the AST. Approximately 0.5-1.0 km east of these mounds, several small- and a few large-scale pillow mounds are situated on the floors of grabens that are 50-80 m deep and 600-800 m wide in the SeaBeam bathymetry.

R3 is located between 9°44'-34'N and covers two 3rd-order OSCs (OSC-2 and OSC-3 on Plate1b), plus one full and one partial 3rd-order segment (S2 and S3 on Plate1b). This region exhibits a relatively symmetric distribution of lobate-dominated terrain with respect to the AST, extending 2-3 km from the axis on both plates. In some places, the lobate-dominated region appears to be terminated by inward-facing faults. In other places, the lobate-dominated terrain extends past the inferred location of inward-facing faults to the base of large-scale pillow mounds farther off-axis. Although pillow mounds in R3 are more abundant on the Pacific plate, this may result from the greater survey coverage on the Pacific plate. On the Pacific plate approximately 2 km west of the AST, two large-scale mounds overprint local faults and a graben at 9°43'N (Plate 1b). More than 3 km off-axis are two groups of large-scale pillow mounds separated by several small-scale pillow mounds, none of which are faulted. On the Cocos plate, only the area between 9°44'and 40'N was surveyed up to 4 km east from the AST. This area shows several small- and large-scale pillow mounds on the outward-facing wall of a graben. Within the remainder of R3 on the Cocos plate where the survey reached only to 2.5 km from the AST, a group of small-scale pillow mounds is aligned 150-300 m east of the 3rd-order OSC at 9°37'N (Figure 12a). Some of these pillow mounds are dissected by faults that exhibit approximately the same strike as the pillow mounds. *Alvin* dives 3525 and 3528 traversed over some of the pillow mounds. The bathymetry profiles created from the dive altitude (or total water depth) data show all of the pillow mounds stand 5-10 m higher than the top of the ridge trough wall and show either Type 1 or 2 profile (Figure 12).

The southernmost region (R4), located between 9°34'-26'N, covers the remaining part of S3 that was not covered in R3 (Plate 1b). This region displays a significant asymmetry in seafloor morphology with respect to the AST. The Pacific plate is predominantly covered by lobate flows up to 3 km from the axis and lava channels are more abundant in this region than anywhere else in the survey area. These channels extend as far as 2.5 km off-axis. In contrast, the lobate-dominated region on the Cocos plate extends <1 km off-axis, the minimum extent observed in the entire field area. The edge of this region on the Cocos Plate stands ~6 m higher than the top of the ridge trough wall in the ABE bathymetry. The seafloor outside the lobate-dominated region on the Cocos Plate consists of sedimented areas with abundant faults and grabens. In this most highly tectonized region of the entire study area, three groups of pillow mounds occur at distances of 1.5, 2.3, and 4.0 km from the AST. The innermost group is composed of four small-scale pillow mounds and mostly overprints the local faults. The middle group is composed of four large-scale pillow mounds. These mounds are the most faulted mounds in the study area; however, individual mounds within this group show different amount of tectonization. The outermost group is composed of two large-scale pillow mounds. The southern of these two mounds is located on the floor of a 750-m-wide, 180-m-deep graben, whereas the northern pillow mound is situated on the outward-facing wall of the graben. Both of these mounds overprint the local faults. The two pillow mounds are separated by a uniformly high backscatter region ~1.6 km-long on the sidescan data that was identified as sheet flow terrain during *Alvin* dives. *Alvin* observations indicate that the southern pillow mound is a ~20 m high construct that appears younger-looking than the surrounding lava flows, suggesting this feature formed *in situ* as the result of off-axis dike eruptions [*Goldstein et al.*, 1994; *Perfit et al.*, 1994]. This interpretation is supported by a near-bottom gravity study of Cochran et al. [1999]. They found large parallel linear Bouguer gravity anomalies at the southern pillow mound and concluded that the anomalies were product of a near-surface dike that fed the off-axis eruption that created the mound [*Cochran et al.*, 1999].

3.4.2 Statistical analysis

<u>Distribution of pillow mounds</u>

In this analysis, the surveyed region was divided into sections 1 km long (along-axis) and <1.5 km and >1.5 km from the AST on both the Pacific and Cocos plates because 1.5 km marks the threshold at which large pillow mounds begin to appear. The regions south of 9°29'N and north of 9°56'N are omitted from the analysis due to asymmetric mapping coverage in these areas. Pillow mound coverage is expressed as a percentage of the total area for the all regions (Figure 14a and b). For the regions >1.5 km, both total survey area and pillow mound area are shown in Figure 14c because the total survey area varies due to survey geometry. The statistical analysis suggests that there are two distinct populations of pillow mounds, one forming near the AST and associated with 3rd-order OSCs and the other forming farther from the axis and showing no systematic distribution along the strike of the AST.

Statistical results show that pillow mounds within 1.5 km of the AST occur in four areas on either the Pacific or Cocos plates: 9°55'N and 9°45'-46'N on the Pacific plate, 9°35'-37'N and 9°29'-31'N on the Cocos plate (Figure 14a). The northern three areas correspond to the present-day 3rd-order OSCs, consistent with the interpretation of White et al. [2002] who proposed that near-axis pillow mounds form through the eruption of lava transported from a smaller and colder axial magma chamber near the segment end that erupts with a lower effusion rate, forming pillow flows. The 9°29'-31'N area is not defined as a 3rd-order OSC; however, this area is considered to have been inactive over relatively long period [e.g., *Schouten et al.*, 2001]. Therefore, pillow mounds in the 9°29'-31'N area may have formed from the same process as the pillow mounds located at 3rd-order OSCs. These findings suggest small-scale pillow mounds located within 1.5 km from the AST form near magmatically starved magma reservoirs.

For areas 1.5 km or more from the AST, the pillow mounds show distinct groupings as a function of latitude on both Pacific and Cocos plates (Figure 14b). On the Pacific plate, the regions from 9°52'-45'N and 9°40'-33'N display up to 19% pillow mound coverage whereas, on the Cocos plate, the regions from 9°56'-53'N, 9°48'-42'N, and 9°33'-29'N display up to 23% pillow mound coverage. There is no noticeable correlation between pillow mound location and present-day 3rd-order segmentation. Additionally, pillow mounds are distributed asymmetrically with respect to the AST on the two plates. While there is some overlap of the pillow-mound abundant areas between the two plates (9°52'-40'N), in most locations abundant pillow mounds occur on only one plate. This result may again reflect the asymmetric shape of the survey (Figure 14c). For example, the area from 9°40'-34'N on the Cocos plate where few pillow mounds are observed was surveyed only as far as ~2.5 km from the AST compared to ~3-3.5 km on the Pacific plate, a region which shows abundant pillow mounds. In summary, there is no apparent pattern for the along-axis distribution of pillow mounds that are located more than 1.5km from the AST.

Terminations of lobate-dominated regions: Potential ponding of lava flows by inward-facing faults and pillow mounds

The sidescan data show that lobate-dominated regions extend from the AST as far as the survey boundaries in some areas. In other locations the lobate-dominated regions terminate against large-scale pillow mounds or inward-facing faults (Plate 1b). I calculated percentages of each boundary type observed on the Pacific plate for the total survey length of 60 km. Calculations were not performed for the Cocos plate because of the poor quality of sonar data in a swath located ~1-2 km away from the AST. Results for the Pacific Plate show that lobate flows extend to the survey boundary for 16 % of the total length of the survey area. Flows end at inward-facing faults and pillow mounds in 44.5% and 15.5% of the total length, respectively. Twenty-four percent of the terminations cannot be categorized. This distribution does not correlate with present 3rd-order segmentation; furthermore, it shows that along more than half of the total survey length lobate flows accumulate within 2-3 km from the AST by being blocked by the pillow mounds or inward-facing faults.

CHAPTER 4: OFF-AXIS ERUPTION MODEL FOR THE FORMATION OF PILLOW MOUNDS

Field observations as well as seismic and geodetic monitoring document the close association of dike intrusions and faults [*Rubin and Pollard*, 1988; *Rubin*, 1992]. The results of analog experiments by Mastin and Pollard [1988] suggest that two zones of elevated tensile stress develop at the seafloor surface on either side of an intruding dike (Figure 15a). If normal faults form above an intruding dike, they tend to develop along these zones prior to the dike reaching the surface [*Pollard et al.*, 1983]. In some cases grabens form above a dike. If the dike penetrates to the seafloor, an eruptive fissure forms (Figure 15b). Terrestrial observations also show that magma commonly erupts along one of the graben-bounding faults [*Duffield et al.*, 1982]. Depending on the volume and rate of the eruption, lava flows may construct a mound, fill some or all of a pre-existing graben, or both (Figure 15b). In a MOR environment, if a mound is formed by this process outside of the AST, the original mound surface is likely to be covered by subsequent lava flows from the AST (Figure 15c). Depending on the volume of these subsequent flows, they may pond against the on-axis side of the mound or inundate the mound.

The morphology of lava that erupts onto the seafloor is determined by a combination of three factors: underlying local slope, lava viscosity, and effusion rate [*Gregg and Fink*, 1995]. To quantify the effects of each factor, Gregg and Fink [2000] conducted laboratory simulations using polyethylene glycol in a cold sucrose solution. Their results show that on all slopes between 1° and 60°, pillow flows form at the lowest effusion rates, lobate flows at intermediate rates, and sheet flows at the highest rates. Griffiths and Fink [1993] propose upper thresholds for the eruption rate for pillow flow formation of <1 m^3/s for a point source and <3 m^2/s per unit length for a line source. Noting that the viscosities of most lava flows at MORs are similar, Perfit and Chadwick [1998] hypothesize that effusion rate has the biggest influence on the flow morphology. However, their study and the majority of other studies investigating submarine lava viscosity examine samples collected within 2-3 km of the ridge axis. Virtually no systematic sampling of lava farther than 3 km from the ridge axis has been undertaken.

If dike intrusion produces an eruption, a high initial effusion rate may form sheet or lobate flows during the early stages of the eruption [*Gregg and Fink,* 1995]. As the effusion rate wanes later in the eruption, pillow flows are more likely to be produced. Concurrently, the eruption becomes localized into a few discrete vents [*Richter et al.*, 1970; *Swanson et al.*, 1979]. In such a scenario, pillow lavas might be expected to cluster near point-source vents during the late stages of an eruption, overlying previously erupted sheet and lobate flows.

If an eruption initiates with a low effusion rate, pillow lava probably forms during the early stages creating linear accumulations along the eruptive fissure. Perfit and Chadwick [1998] suggest that low effusion rate eruptions occur on the seafloor where eruptions are infrequent. They argue that because each dike intrusion imposes new compressive stresses on the surrounding crust, for magma to erupt where intrusions are frequent, a higher internal magma pressure with a correspondingly higher effusion rate is necessary. According to this hypothesis, low effusion rate eruptions can only occur in regions where dike-related stresses are low, such as outside the ridge axis. Perfit and

Chadwick [1998] also speculate that off-axis lava flows have higher viscosities because magma must travel a longer distance through potentially cooler crust in order to erupt a few kilometers off axis. Higher viscosity tends to favor pillow formation [*Gregg and Fink, 1995*].

There have not been any detailed near-bottom studies of the off-axis pillow mounds; however, some pillow mounds at and near the ridge axis have been studied on intermediate and super-fast spreading ridges [*Perfit and Chadwick*, 1988 and *White et al.*, 2000, respectively]. Detailed near-bottom observations and findings from these two studies provide the morphological characteristics of pillow mounds and help explain the processes responsible for the formation of off-axis pillow mounds.

The first study was conducted on the northern Cleft segment of the JdFR. The Cleft segment is the southernmost segment of the JdFR with a full-spreading rate of 45 mm/year, considered to be intermediate in the spectrum of spreading rates [*Embley et al.,* 1991]. Intermediate-spreading ridges may or may not have a steady-state magma reservoir [*Perfit and Chadwick*, 1998]. An eruption on the Cleft segment in the mid-1980's was detected through the discovery of unusually large and shallow hydrothermal plumes [*Baker et al.*, 1987; *Baker et al.*, 1989]. Subsequent near-bottom observations using a deep-towed camera system and submersible dives allowed Chadwick and Embley [1994] to study "zero-age" pillow mounds in the neovolcanic zone, a 3-km wide axial summit graben where volcanic activity was concentrated [*Embley et al.,* 1991]. The near-bottom data depict pillow mounds with smooth, symmetric shapes distributed along narrow grabens associated with eruptive vents in the broader axial summit graben. These narrow grabens are 10-100 m wide and 5-15 m deep where not overprinted by lava flows.

Chadwick and Embley [1994] interpret some of the narrow grabens to be newly formed whereas others appear to have been reactivated by the eruption. The shapes and sizes of the pillow mounds within the grabens vary from small circular mounds, 50 m in basal diameter and 2 m in height, to elongated steep-sided ridges that are 4.2 km long, 500 m wide, and ~60 m high. The pillow mounds actually consist of intermingled lobate and pillow flows in approximately equal abundance. The peaks of the pillow mounds in the Cleft segment are covered by ponded lobate flows whereas the steepest slopes are dominated by pillow flows. Chadwick and Embley [1994] suggest that these pillow mounds are built by magma rising up through the mounds, erupting at the summit, and flowing down the sides. Although no distinct vent structure is visible at the apex of these pillow mounds, low-temperature hydrothermal vents with biological communities and hydrothermal sediments that commonly develop near eruptive fissures [*O'Neill*, 1998] indicate a sustained heat supply.

White et al. [2000] investigated another group of pillow mounds located on the southern EPR between 17°11'S and 18°37'S. This segment of the EPR spreads at a full rate of ~140 mm/year [*DeMets et al.*, 1990] and is thought to have a more robust supply of magma than the northern EPR. High-resolution DSL-120 sidescan and bathymetry data show that pillow mounds are located outside the AST, 200-400 m east of the ridge axis; they are sub-circular topographic highs with an average diameter of 200 m and height of 20 m that align parallel to the ridge axis. Some of the pillow mounds coalesce and form a ridge subparallel to the ridge axis. These coalesced pillow mounds are dissected by ridge-parallel fissures in the 17°53'S area. Using near-bottom photographs from the *Argo II* system, White et al. [2000] also document that the pillow mounds are associated with active hydrothermal venting.

Based on the observations of Chadwick and Embley [1994] and White et al. [2000] and land-based analogs cited in this chapter, I expect pillow mounds formed by off-axis eruptions to show some of the following characteristics:

- A discrepancy between lava age/glassiness and/or a difference in the amount of sediment cover on the two sides of the pillow mound if subsequent on-axis lava flows covered the on-axis side of the pillow mound slope.
- Ridge-parallel normal faults near pillow mounds, or pillow mounds located on the floor of, or overprinting, ridge-parallel grabens.
- In the sonar data, sub-circular or ridge-parallel elongate shapes that have smooth or bulbous surface textures.
- Pillow mounds with dome-shaped cross-sections (Figure 15a-top). If the side of the pillow mound closest to the ridge axis has not been overprinted by subsequent lava flows from the upslope eruptive events, the cross-sectional shape will be almost symmetric. If the axis-facing side of the pillow mound has been inundated by subsequent eruptions, only the downslope side will retain the original pillow mound morphology (Figure 15c-top). If the volume of the subsequent lava is not enough to inundate the pillow mound, the pillow mound will be partially covered having a cross-sectional shape that is asymmetric with the upslope side shorter than the downslope side (Figure 15c-bottom).

- Depending on the local heat supply, there could be active or extinct hydrothermal vents or hydrothermal sediments on the pillow mounds.
- If pillow flows form in the waning stages of an eruption, the stratigraphy of the pillow mound will show pillow flows overlying sheet or lobate flows.

CHAPTER 5: MECHANICAL ANALYSIS

Many of the pillow mound characteristics observed in the DSL-120A sidescan data and described in Chapter 3 meet the morphological criteria for pillow mounds built by off-axis eruptions, examined in Chapter 4. For an off-axis eruption model to be viable, it should allow magma originating from a thin AML to erupt at the ridge summit as well as on the ridge flank. To assess models for the off-axis formation of pillow mounds, plausible stress fields for the study area are analyzed using a code based on a two-dimensional, plane-strain boundary element code [TWODD; *Crouch and Starfield*, 1983]. The analysis accounts for several key factors: 1) elastic deformation of the crust; 2) gravitationally-induced stresses due to the weight of the rock and the overlying water; 3) a seafloor free of shear tractions with a ridge topography; 4) normal and shear tractions at the base of the lithosphere that are reasonable for the tectonic setting of a MOR; and 5) the presence of a sill-like magma body below the ridge crest. The analysis does not consider: 1) variations in the rigidity of the crust [*Vera et al.*, 1990; *Nicolas et al.*, 1996; *Dunn et al.*, 2000]; and 2) thermal effects [*Madsen et al.*, 1984; *Wilson* 1992; *Eberle et al.*, 1998].

A few previous studies have analyzed the mechanical interaction between a fluid-filled fracture and a free surface [*Pollard and Hozhausen*, 1979; *Fialko*, 2001]. TWODD analyses applying a lithostatic ambient stress field and a flat seafloor show the feasibility of an off-axis eruption originating from a sill tip [*Fialko*, 2001]. Fialko [2001] proposes that these eruptions form pillow mounds on the flank of the EPR. This study builds upon the results of Fialko [2001] by also considering the effects of a gravitationally induced stress due to the weight of the overlying water, ridge topography, and tractions at the base of the lithosphere. This chapter first discusses the conceptual model and boundary element method to set up the problem. The analysis and a discussion follow. The source codes for the analysis are found in Appendix D.

5.1 Conceptual Model

Based on geophysical and petrological evidence, Sinton and Detrick [1992] considered a magma reservoir at a fast-spreading MOR to be a thin and narrow melt lens below the ridge crest (Figure 16a). This lens would be typically less than 1.5 km wide (across the ridge axis) and 10-50 m thick [e.g., *Kent et al.*, 1993]. The melt lens overlies a partially solidified mush zone 1-2 km below the seafloor. The melt lens and the mush zone are surrounded by a mostly solidified region within the gabbroic layer called a transition zone. These regions are inferred to be weaker than the surrounding crust [*Vera et al.*, 1990; *Nicolas et al.*, 1996; *Dunn et al.*, 2000].

The geometry and parameters of the mechanical model are based on the conceptual model of Figure 16a, which in turn is based on the results of Sinton and Detrick [1992] and Kent et al. [1993]. The crust is treated as homogeneous, isotropic, and linear elastic. The large width-to-thickness ratio of the melt lens allows it to be treated as a pressurized sill below the ridge crest (Figure 16b). The ridge topography for the model is based on across-axis bathymetry profiles of the 9°50'N and 9°30'N regions generated from SeaBeam data [*Macdonald et al.,* 1993]. The ridge is represented as a 0.5-km high and 20-km wide isosceles triangle with a slope of 3° (Figure 16c). The ridge crest is located 2.5 km below the sea surface. The crust has a uniform thickness of 5 km from the ridge base [*Barth and Mutter,* 1996]. Its base is treated as the base of the lithosphere due to the rise of the asthenosphere below the MORs [e.g., *Turcotte and Morgan*, 1992].

Upper mantle convection currents are considered by some to exert normal and shear tractions on the base of the lithosphere at MORs [e.g., *Turcotte and Morgan*, 1992]. The relative motion of the mantle and lithosphere vary among different models. In an active mantle-upwelling model, the upwelling of the mantle generates shear tractions at the base of the lithosphere (Figure 17a), driving the plates apart. In this model, the relative displacement of the mantle with respect to the lithosphere at the upper part of the convection cell is away from the MOR (Figure 17b; Figure 17a at α=90°). Contrastingly, in a passive mantle-upwelling model, the mantle rises in response to the plates being pulled apart. Even though the absolute displacements of both the lithosphere and the mantle are away from the MOR (Figure 17c) in the passive case, the relative displacement of the mantle with respect to the lithosphere is toward the MOR. This case is found at the upper part of the convection cell at α=-90°/270° (Figure 17a).

To simulate the effect of mantle convection currents near the MOR, normal and shear tractions acting on the base of the crust [*Hafner*, 1951] are introduced in the model. By varying the model parameters, a range of ambient stress fields can be produced, including fields for both active and passive mantle-upwelling models. The active mantle-upwelling model is considered here. The positive x-direction is horizontal and the positive y-axis points down (Figure 16c). The plane $y = 0$ defines the sea surface. The ridge is symmetric across the plane $x = 0$, which corresponds to α=90° (Figure 17a). Tensile stresses are defined as positive.

5.2 Boundary Element Method

The boundary element method (BEM) is a powerful technique for analyzing displacement fields and the state of stress around fractures and faults [*Crouch and Starfield*, 1983]. BEM solutions accounting for body forces (e.g., gravity) and topography match well with analytical solutions [*Martel and Muller*, 2000]. To simulate a crack, the boundary element code TWODD [*Crouch and Starfield*, 1983] relies upon a discrete approximation to a continuous distribution of displacement discontinuities. The boundaries of a body are defined by a series of segments or elements, and the normal and shear tractions are specified for each element. A constant discontinuity in displacement is solved for each element such that the specified traction boundary conditions are met. As a result of the displacement discontinuity across a given element, stresses are induced in the surrounding body. TWODD relies on the principle of superposition to find the total stress field perturbation in the body due to the effect of all the elements. Solutions for a fractured material subject to body forces are found by superposing the solution due to the body forces along with the stress perturbation due to the fractures [*Martel*, 2000]. For the problem at hand, two cracks come into play. The melt lens is represented by a pressurized crack. The seafloor near the ridge is represented by a long crack free of shear tractions, with the normal traction equal to the pressure exerted by the overlying water.

5.3 Ambient stress field

The ambient stress field is important to consider in this study because it may influence where magma accumulates in the crust. This stress field reflects the stresses due to gravity (i.e., body forces) and normal and shear tractions at the base of the crust. I first examine the effects of gravity then superpose the effects of the normal and shear tractions. In this study, the contribution of gravity is discussed in terms of two different sections. Section I is the area below the ridge flank but above the ridge base, and Section II is the region below the ridge base (Figure 16c). Several models have been proposed to explain the axial topographic high at the EPR including buoyant uplift from a narrow zone of concentrated partial melt extending from the mantle [*Madsen et al.*, 1984; *Wilson* 1992; *Eberle et al.*, 1998], or uplift caused by dynamic, extensional stresses in the upper crust [*Eberle and Forsyth*, 1998]. In this study, the stresses in the ridge are simplified and treated as if the ridge formed by the accumulation of erupted lava flows [*Martel*, 2000]. Based on this assumption, in Section I, the ambient horizontal stress depends only on the water pressure [see *Martel*, 2000]. The body forces arising from gravity for each section are:

Section I

$$\sigma^{I}_{yy} = \rho_w g y_w + \rho_c g y_c, \tag{1}$$

$$\sigma^{I}_{xx} = \rho_w g y_w, \tag{2}$$

$$\sigma^{I}_{xy} = 0, \tag{3}$$

Section II

$$\sigma^{II}{}_{yy} = \rho_w g y_w + \rho_c g y_c, \tag{4}$$

$$\sigma^{II}{}_{xx} = 0, \tag{5}$$

$$\sigma^{II}{}_{xy} = 0, \tag{6}$$

where

ρ_w = density of water,

ρc = density of the crust,

g = gravitational acceleration,

y_w = height of the overlying water column (a function of x),

y_c = thickness of the overlying crust (also a function of x).

Values used for each parameter are listed in Table 1.

The body forces by themselves cause the most compressive stress (σ_2) to be vertical in and beneath the ridge (Figure 18a). Since dikes would propagate perpendicular to the most tensile stress (σ_1), trajectories in the direction of σ_2 represent the most likely magma path. Figure 18a shows the most tensile stress represented with contour lines. The horizontal stresses below and above a depth of 0.9 km from the ridge crest are tensile and compressive, respectively. This stress field indicates that if any cracks exist, magma would rise upward from the base of the crust to a depth of 0.9 km.

To account for the effects of normal and shear tractions at the base of the crust induced by upper mantle convection currents under the lithosphere I rely on the solutions for normal and shear stresses provided by Hafner [1951]:

$$\sigma^{H}{}_{xx} = \sin \alpha x \; \{ -k_1 f_1(y) + k_2 f_2(y) \};\tag{7}$$

$$\sigma^{H}{}_{yy} = \sin \alpha x \; \{ -k_1 f_3(y) - k_2 f_4(y) \};\tag{8}$$

$$\sigma^{H}{}_{xy} = \cos \alpha x \; \{ k_1 f_4(y) - k_2 f_1(y) \};\tag{9}$$

where

$$\left.\begin{aligned} f_1(\mathrm{y}) &= \sinh \alpha(y-y_{wmax}) + \alpha(y-y_{wmax}) \;\cosh \alpha(y-y_{wmax}); \\ f_2(\mathrm{y}) &= 2 \cosh \alpha(y-y_{wmax}) \; + \alpha(y-y_{wmax}) \;\sinh \alpha(y-y_{wmax}); \\ f_3(\mathrm{y}) &= \sinh \alpha(y-y_{wmax}) \; - \alpha(y-y_{wmax}) \;\cosh \alpha(y-y_{wmax}); \\ f_4(\mathrm{y}) &= \alpha(y-y_{wmax}) \;\sinh \alpha(y-y_{wmax}); \end{aligned}\right\}\tag{10}$$

$$\left.\begin{aligned} k_1 &= (A\alpha\mathrm{c} \cosh \alpha\mathrm{c} - B\alpha\mathrm{c} \sinh \alpha\mathrm{c} + A \sinh \alpha\mathrm{c}) \,/\, (\sinh^2\alpha\mathrm{c} - \alpha^2\mathrm{c}^2); \\ k_2 &= (A\alpha\mathrm{c} \sinh \alpha\mathrm{c} - B\alpha\mathrm{c} \cosh \alpha\mathrm{c} + B \sinh \alpha\mathrm{c}) \,/\, (\sinh^2\alpha\mathrm{c} - \alpha^2\mathrm{c}^2); \end{aligned}\right\}\tag{11}$$

y_{wmax} = depth from the sea surface to the ridge base;

c = thickness of the crust;

$\alpha = 2\pi/L$, horizontal angular position;

L = full wavelength of sinusoidal variations of the stress components;

A and B = maximum values of normal and shear tractions at the base of the crust, respectively.

All three of Hafner's stress components are a function of angular position (α) and vary sinusoidally in the horizontal direction (Figure 17a). In the vertical direction they vary according to more complicated hyperbolic functions (f_1 to f_4). The half wavelength ($L/2$) represents the width of a mantle convection cell.

When the Hafner contribution for stresses below the ridge is included, the ambient stress states for Section I remain the same, but those for Section II become:

$$\sigma^{II}_{yy} = \rho_w g y_w + \rho_c g y_c + \sigma^{H}_{yy}, \tag{12}$$

$$\sigma^{II}_{xx} = \sigma^{H}_{xx}, \tag{13}$$

$$\sigma^{II}_{xy} = \sigma^{H}_{xy}. \tag{14}$$

The parameters A and B in equation (11) control the character of Hafner's stress field. At a given distance x, certain values of A and B create a stress field where σ^{H}_{xx} is most tensile at the crust base and most compressive at the ridge base. Accordingly, σ_2 trajectories are vertical at the crust base but become horizontal at some depth. This stress state would allow magma to rise from the crust base and accumulate at the greatest depth where σ_2 trajectories are horizontal. In this study, this depth, henceforth called the trajectory-flipping depth, is considered to be a possible location for formation of a horizontal melt lens. Different values of A and B locally cause the most compressive stresses to be vertical through the crust outside the ridge region, allowing dikes to propagate all the way to the seafloor.

The presence or absence of gravitational body forces largely influences the values of A and B required to produce a flip in the compressive stress trajectories. Here, I search for values of A and B that, in the presences of body forces, cause the most compressive stress trajectories to change from vertical to horizontal beneath the ridge without creating regions elsewhere where the most compressive stress is vertical through the crust. In the ambient stress field induced by just gravity, the horizontal body forces in the crust (σ^{II}_{xx}) are nil (equation 5), but the vertical body force (σ^{II}_{yy}) is a large compressive stress on the order of 10^7 Pa at a depth of 2 km. To allow the most compressive stress trajectories to flip from vertical to horizontal while accounting for gravity, B must be equal to or larger than 10^8 Pa, and A must lie in a range of 0 to 10^3 Pa. For a crustal thickness of 5-8 km, the trajectory-flipping depth appears at 42-36 % of the crustal thickness from the ridge crest (i.e., at a depth of 2.1-2.9 km below the ridge crest). In the following analyses, A=10^3 Pa and B=10^8 Pa. The other model parameters that may influence the trajectory-flipping depth are the wavelength of the mantle convection cell (L) and the density of the crust (ρ_C). Theoretical analysis of convection cells indicates that L in the active mantle-upwelling model is four times larger than the thickness of the convection layer [*Turcotte and Morgan*, 1992]. According to the findings of petrological and geochemical studies, the oceanic crust is generated by an average of 10-15% partial melting of the sub-ridge mantle [*Turcotte and Morgan*, 1992]. Understanding the sub-ridge mantle as the convection layer, a 5-km thick crust requires a mantle convection layer that is 50 km thick assuming 10% partial melting. Since L is four times larger than the thickness of the convection layer, L becomes 200 km. Using 200 km as the minimum value of L and increasing it systematically in repeated simulations, I found the trajectory-flipping depth to be insensitive to values of L in a range of 200-3,600 km. Values of ρ_C ranging between 2,500 kg/m^3 and 2,950 kg/m^3 [e.g., *Kent et al.*, 1993] were also found not to have a significant effect on the trajectory-flipping depth, so I used a value of 2,500 kg/m^3 for my simulations. Using the values specified for other parameters in bold font in

Table 1, I obtained a possible melt-lens depth of about 2.1 km below the ridge crest (Figure 18b).

For this analysis the oceanic crust is modeled with non-uniform thickness, being thickest below the ridge axis and of uniform thickness (5 km) outside the ridge flank (Figure 16c). The oceanic crust below the EPR probably has a more uniform thickness [e.g., *Barth and Mutter,* 1996]. However, if the boundary conditions for the base of a crust with an upper surface like that of Figure 16c but a uniform thickness of 5 km are defined with normal and shear tractions as shown in Figure 19, the simulations in this study remain valid for a crust of uniform thickness.

5.4 Sill and ambient stress field

Accumulated magma at the trajectory-flipping depth forms the AML below the ridge crest and, as it is pressurized, perturbs the ambient stress field. The AML is simulated in a form of a horizontal sill with a uniform internal pressure. In a case of the sill with a dominant vertical opening, the driving pressure (ΔP) in the sill is defined as [*Pollard and Segall*, 1987]:

$$\Delta P = -\Delta\sigma^{s}{}_{yy}; \tag{15}$$

where

$$\Delta\sigma^{s}{}_{yy} = \sigma_{yy} - \sigma^{s}{}_{yy};$$

$\sigma^{s}{}_{yy}$ = vertical stress in a sill.

For a two-dimensional sill in an infinite body, the driving pressure (ΔP) is [*Pollard and Segall*, 1987]:

$$\Delta P = \mu \Delta U_{max} / (2S(1 - \nu)); \tag{16}$$

where

ΔP = driving pressure (i.e., the pressure in excess of the ambient value of σ_{yy});

μ = shear modulus;

$\mu = E / 2(1 + \nu)$;

E = Young's modulus;

ΔU_{max} = maximum vertical opening of the initial sill;

S = half-width of the initial sill;

ν = Poisson's ratio.

Values used for each parameter are listed in Table 1. Equation 16 provides a useful estimate for sill driving pressures in a half-space if the sill depth is large relative to the sill half-width, and that is the case here.

In this study, ΔU_{max} is considered to be the thickness of the AML; it ranges from 10-50 m according to Kent et al. [1993]. In the following analyses, U_{max} is set to 50 m. The sill with a 350-m-half-width S is inserted directly below the ridge crest at a depth of 2 km (Figure 20a), with ΔP=9.5x10^8 Pa. The total pressure in the sill is 18.7x10^8 Pa (i.e., σ_{yy} in the sill equals -18.7x10^8 Pa).

As a result of the pressurized sill, σ_2 trajectories directly above the center of the sill (Figure 20a) have rotated 90° and are now vertical. This opens the possibility of vertical dikes propagating up from the center of the AML. Although compressive horizontal stresses exceeding 7×10^8 Pa are induced immediately above the sill (Figure 20b), they are smaller than the total pressure in the sill itself. Under these conditions, a vertical dike might be able to propagate up from the AML utilizing existing zones of weakness. Where σ_2 trajectories directly above the center of the sill are flipped from vertical to horizontal (Figure 20c), the maximum shear stress (τ_{max}) of ~ 10^8 MPa is much less than the driving pressure. In other words, the difference between the principal stresses is relatively small in this region. This means that the stress trajectories could be rotated to vertical if a dike were intruded. The conditions are such that if a vertical dike were to grow from the AML, it could continue to propagate upward until it erupts at the ridge summit. This dike propagation scenario is henceforth called Type A.

5.5 Sill Propagation

Although the pressurized sill perturbs the ambient stress field and allows a dike to propagate up from the center of the sill, the tips of the sill show a strong tensile stress concentration (Figure 20b). Thus, crack growth is favored at the sill tips. In a lithostatic ambient stress state, a sill is predicted to propagate laterally until the sill half-width is about equal to the sill depth *H* [*Pollard and Hozhausen*, 1979; *Fialko*, 2001]. Once the sill half-width exceeds *H*, the sill would begin to interact with the seafloor and propagate upward towards the surface. Eventually it would erupt on the surface at a distance of approximately 3*H* from the original center of the sill [*Pollard and Hozhausen*, 1979; *Fialko*; 2001]. Pollard and Holzhausen [1979] explain that this sill propagation path occurs as a result of asymmetric displacements of the sill walls, the upper wall being displaced more than the lower wall. In an infinite body, the upper and lower walls of a sill are equally displaced but in opposite directions (Figure 21a). However, for a shallow sill, the upper sill wall moves up more than the lower wall moves down (Figure 21b). Associated with this asymmetric opening is an asymmetric sill-parallel displacement, or shearing, of the upper and lower walls that causes the sill to propagate out of plane up towards the seafloor.

In my simulations, a sill tip was constrained to propagate in a direction perpendicular to the most tensile stress concentric about the sill tip. Growth increments were set to 10 m. The sill was allowed to propagate out of a horizontal plane only when the most tensile stress 10 m from the sill tip deviated by one degree or more from vertical. Based on these conditions, I found that the sill propagates essentially laterally at both tips until its half-width reaches a certain distance (S_{max}; Figure 21c), consistent with the findings of Pollard and Hozhausen [1979] and Fialko [2001]. While the sill half-width is increased to S_{max}, ΔP for the element composing the extended portion of the sill is kept constant. As the sill half-width increases, σ_2 trajectories directly above the center of the sill become horizontal again (Figure 20a and 22a). This stress change would work against a Type-A eruption scenario.

Once the sill half-width reaches S_{max} and the sill begins to propagate upward, only one tip is allowed to continue to propagate, following the methodology of Fialko [2001]. The driving pressure for the elements along the upward part of the propagation path is decreased in proportion to the changes in elevation. This approach differs from Fialko's [2001] in which ΔP is maintained constant for elements between a depth of H and $H/2$ and is linearly decreased to zero between a depth of $H/2$ and 0 (seafloor). The sill propagating upward eventually erupts on the seafloor at a distance of $3H$ from the ridge crest. This single-sided sill propagation scenario is henceforth called Type B1.

As one tip propagates, the most tensile stress concentration at the non-propagating tip becomes greater than at the propagating tip (Figure 22). This indicates that mechanical conditions favor sill propagation at both tips. When propagation occurs in two directions using a sill with an initial half-width of 350 m and an initial thickness of 50 m, the distance to the eruption site (D) is approximately 2% greater than Type-B1 scenario. This two-sided sill-tip propagation scenario is henceforth called Type B2.

5.6 Simulations representing five locations in the study area

Using the case of the sill with 350 m half-width as a springboard, five simulations are performed to represent five locations between 9°50'-30'N in the study area (Table 2). The simulations are conducted using the same approach and values for the model parameters as in the springboard case (see Table 1) except for the driving pressure (ΔP), half-width (S), and emplacement depth (H) of the sill, and the location of the sill center with respect to the ridge axis. The driving pressure is held constant in each simulation in a range of $5.3\text{x}10^8$ - $5.7\text{x}10^8$ Pa. Values for the last three parameters rely on the findings of a seismic study by Kent et al. [1993]. The half-widths of sills is set in a range of 125-600 m (Table 2), with H ranging from 1.4 to 1.7 km below the ridge crest. These depths are shallower than the trajectory-flipping depth of 2.1 km that resulted from the ambient-stress-field simulation; however, producing a trajectory-flipping depth of 1.4-1.7 km in a 5 km-thick crust would require values of A and B that would locally cause σ_2 trajectories to be vertical through the crust. Therefore, I decided to conduct the simulations using values that produced a trajectory-flipping depth of 2.1 km. The location of the sill center with respect to the ridge axis is offset between 100 and 500 m to one side of the ridge axis in four simulations to reflect the findings of Kent et al. [1993; Table 2].

Each of the five simulations generated stress changes qualitatively similar to those for the 350 m half-width sill. These results indicate that eruptions of Type A, B1, and B2 would also be possible under the conditions of the five simulations. Here, I discuss the values of *D* produced from the five simulations, first not considering the sill offset with respect to the ridge axis and then considering the sill offset. When the sill offset is not applied, the range of *D* in the simulations is 4.8-5.4 km (Table 2). The resulting distances largely reflect the range of the sill emplacement depth (see section 5.5). In a Type-B2 eruption, a sill propagates laterally until it attains a certain half-width before it starts to propagate upward. Therefore, the initial sill half-width does not have much influence on *D*. Sills with initial half-widths of 125 m and 350 m at the same emplacement depth both yielded a *D* value of 5.2 km. This is because the 125 m half-width sill propagates laterally to 340 m before turning toward the surface. Even a 0.6 km-half-width sill emplaced 100 m deeper than narrower sills produced a *D* value of 5.4 km. The increase in *D* of 0.2 km is mostly due to the deeper sill-emplacement depth.

Accounting for sill offsets in the four simulations causes *D* to become slightly larger (4.5-5.9 km; Table 2) than in cases where the sill is not offset with respect to the ridge axis. More importantly, the offset sill geometry produces asymmetric eruption sites with respect to the ridge axis. Among the four simulations with an offset sill, the largest difference between the values of *D* on the two plates occurs for the simulation corresponding to 9°30'N. The center of the sill is placed 500 m west of the ridge axis, resulting a difference of 1 km in D on the Pacific and Cocos plates. In summary, the offset of the sill geometry resulted in a slight increase of the range of D. However, the narrow range of D (~1.5 km) shows, with the ranges of half-width and emplacement depth of the AML detected in the study area, that Type-B2 eruptions occur at relatively similar distances from the ridge axis in the simulations.

5.7 Results and Discussion

The results of the TWODD analysis imply that as an AML is pressurized dikes could propagate towards the seafloor along two paths. One path originates from the upper surface of the AML near its center and continues to the ridge axis (Type A, Figure 23a). The other path initiates from the tips of the AML (Type B1, Figure 23b; Type B2, Figure 23c) and propagates laterally away from the ridge axis in both directions until the sill attains an S_{max}. Once the sill reaches this half-width, it starts to propagate towards the surface, probably on both sides of the AML, in a roughly parabolic trajectory that reaches the seafloor several kilometers from the ridge axis.

Of the several model parameters, some exert a greater influence than others in determining the distance to the eruption site. One important parameter to be considered is B, the maximum value of normal basal traction. As shown in equations (7), (8), (10), and (11), the contributions to σ_{xx} and σ_{yy} due to basal tractions are proportional to B. For a constant value of A, if B increases, then σ_{xx} and σ_{yy} become more compressive in the region below the ridge in Section II. The increase of compressive stress is greater for σ_{xx} than for σ_{yy}. As a result, an increase of B inhibits the upward propagation of the sill in the upper part of the crust, thus increasing D. The sill emplacement depth (H) and the driving pressure of a sill (ΔP) also influence D. An approximately 3% increase in D is achieved by a 5% increase of H, with H in a range of 1.4-2.0 km. An increase of ~3% in D is also achieved by increasing ΔP by a factor of five from 1.9×10^8 Pa (ΔU_{max}=10m) to 9.5×10^8 Pa (ΔU_{max}=50m). These findings show that D is more sensitive to changes in H than changes in ΔU_{max}.

The three new factors introduced in this study also influence the location of the off-axis eruption site in the simulations. To evaluate the effects of each factor on D, I ran three simulations using a 350 m half-width sill at a depth of 2 km below the ridge crest for different ambient stress fields (Figure 24). The first simulation, simulation 1, was conducted to compare my results with the findings of Fialko [2001] and to evaluate the effect of the normal and shear tractions at the base of the crust. In simulation 1 (Figure 24b) the basal tractions are for $A=10^3$ Pa and $B=10^8$ Pa (see equation 11), whereas the simulation by Fialko [2001] accounts for no basal tractions (Figure 24a). In both simulations, the seafloor is flat and water pressure is ignored. The value of D in my simulation 1 is 20% greater than what Fialko's calculations would predict. This increase in D reflects the influence of the basal tractions. In simulation 2, the seafloor is flat and experiences pressure due to a >2.5-km tall water column above it (Figure 24c). A comparison of simulations 1 and 2 shows that the effect of the water pressure reduces D by 1%. Simulation 3 accounts for the topography of the ridge but does not account for water pressure (Figure 24d). A comparison of simulations 1 and 3 shows that the topography of the ridge reduces D by 9% compared to simulation 1 where the seafloor is assumed to be flat. These comparisons indicate that the influence of the basal tractions is more pronounced than the effects of ridge topography and water pressure in determining the distance to a predicted off-axis eruption site.

Several conditions were not represented in the simulations that I conducted. A significant factor that was not considered was the variable rigidity of the crust. The crust was treated as homogeneous in this study; however, the crust below the AML is considered to be weaker than the surrounding crust [*Vera et al.*, 1990; *Nicolas et al.*, 1996; *Dunn et al.*, 2000]. One potential effect of this weak zone under the influence of tectonic tensile stresses is an enhanced horizontal displacement below the melt lens. This horizontal displacement would resemble that produced by a vertical opening-mode crack beneath the AML. The total stress field induced by a sill and a sub-sill vertical crack reflects the contribution of each component. If the stress field created by the sill dominates, then the total stress field would be similar to that produced by the sill alone. In contrast, if the stress field due to the weak zone dominates, then the total stress field above the AML would be similar to one associated with the tip of a vertical crack. Pollard et al. [1983] have shown that a tensile stress concentration arises at the tip of a dike in a half-space and a crack is most likely to initiate from that point. Based on their analysis, the weak zone below the AML would enhance the occurrence of Type-A eruptions.

In summary, my TWODD analysis shows that stress fields that allow both on- and off-axis eruptions are induced by the normal and shear tractions at the base of the crust and a pressurized AML. The tractions produce a stress field that allows magma to rise from the base of the crust and accumulate at a fixed depth, enabling the formation of an AML. Then the pressurized AML itself perturbs the ambient stress field, enabling the initiation and propagation of magma-driven fractures along two paths: one to the ridge crest and the other to the ridge flank several kilometers from the ridge axis.

CHAPTER 6: RESULTS AND DISCUSSION

The goal of this thesis is to investigate the causes and consequences of off-axis volcanism at the EPR between 9°25' and 9°57'N in order to constrain the processes responsible for the rapid thickening of seismic layer 2A. For this purpose, I analyzed the DSL-120A sidescan sonar data to document the distribution of pillow mounds and performed TWODD analyses to study dual-pathway eruptions. In this chapter, I compare and discuss the eruption sites predicted by the simulations with the locations of large off-axis pillow mounds observed in the DSL-120A sidescan data. I then introduce a dual-pathway eruption model to explain the rapid thickening of seismic layer 2A and discuss its validity.

6.1 Comparison and discussion of observational and TWODD results for the distribution of large off-axis pillow mounds

TWODD simulations were conducted to model off-axis eruption sites where large pillow mounds are likely to form. In both the simulation and the sidescan data, the pillow mounds closest to the ridge lie within a narrow (1.5-km wide) strip parallel to the ridge axis (Table 2). However, the distance from the ridge axis to the pillow mounds is about two times greater in the simulation than in the sidescan data (4.5-6.0 km vs. 2.0-3.5 km, respectively). This discrepancy in distance between the predicted and observed locations may result from several factors that the simulation did not take into account. Among these factors, the most significant may be the heterogeneity of the oceanic crust. Many studies show that the seafloor at the EPR is highly fractured in a direction parallel to the ridge axis [e.g., *Macdonald*, 1982; *Edwards et al.*, 1991; *Wright et al.*, 1995]. Sills propagating in the EPR crust have the opportunity to exploit these zones of pre-existing weakness. In the study area, the majority of fissures and faults occur more than 1.5-2 km away from the ridge crest. If either an inward- or outward-facing fault [*Carbotte and Macdonald*, 1990] with a few meters of throw is located on the EPR flanks, its dip angle and depth of penetration [*Langley*, 2000] could allow a sill to erupt closer to the ridge axis than the modeled location.

One site in the sidescan data is particularly suggestive of pillow mound formation being influenced by a zone of pre-existing weakness. Near 9°31'N, large-scale pillow mounds are found in a 180-m deep graben (Figure 13b). Since it is known that the intrusion of a dike 0.5-1.0 m in width on land can cause no more than 1 m of vertical displacement in the surrounding material [*Rubin and Pollard*, 1988], the depth of this graben is inconsistent with dike-induced genesis [*Sigurdsson*, 1980]. This suggests that the graben existed prior to the formation of the pillow mound. If this hypothesis is correct, magma may have utilized pre-existing faults as a pathway to the seafloor and erupted closer to the ridge axis than it would have in unfractured crust.

Another aspect of the simulation results that agrees with observations derived from the sidescan data is the asymmetric distribution of the pillow mounds with respect to the ridge axis. At two out of five sites for which simulations were conducted, the sidescan data have enough sonar coverage to detect pillow mounds on both sides of the ridge axis (Table 2). At 9°50'N, Kent et al. [1993] observed an AML in seismic data that had its center shifted 250 m to the east from the ridge-axis midpoint. When this AML geometry was incorporated into my TWODD simulation, the resulting eruptive sites were asymmetric with respect to the ridge axis. Pillow mounds were predicted to occur closer to the ridge axis on the Pacific plate than on the Cocos plate (4.5 and 5.0 km, respectively). This modeling result agrees with observations in the sidescan data, which show pillow mounds closer to the ridge axis on the Pacific plate than on the Cocos plate (3.0 and 3.4 km, respectively). Similarly, at 9°45'N, Kent et al. [1993] observed an AML that had its center shifted 100 m to the east from the ridge-axis midpoint. The simulation of this AML geometry also produced an asymmetric distribution of eruption sites with respect to the ridge axis (4.9 and 5.0 km on the Pacific and Cocos plates, respectively). The sidescan data show a greater asymmetry than the simulation predicted, with mounds located 1.7 and 3.4 km from the ridge axis on the Pacific and Cocos plates, respectively. It is possible, however, that the pillow mound located 1.7 km from the axis on the Pacific plate does not have an off-axis origin. Although it is slightly larger than 0.5 km and is classified as a large-scale pillow mound, its morphology and location close to a 3rd-order OSC suggest that this pillow mound may have formed closer to the ridge axis and subsequently been rafted to the present location. The next closest pillow mound from the AST on the Pacific plate is 3.2 km off-axis and is part of a large linear pillow-mound group, which is more consistent with an off-axis origin. If this pillow mound is considered the Pacific-plate partner of the mound 3.4 km off-axis on the Cocos plate, there is a smaller amount asymmetry in the mounds distribution. Therefore, the TWODD simulations at both 9°50'N and 9°45'N reproduce the asymmetric distribution of off-axis volcanism about the ridge crest.

6.2 Dual-pathway eruption model for the rapid thickening of seismic layer 2A

The TWODD analysis shows two possible eruption pathways from the AML to the seafloor. One pathway originates at the center of the AML and propagates to the ridge axis (Type A; Figure 23a). This is the generally accepted pathway for magma that constructs a large proportion of extrusive layer 2A on the EPR. The other pathway initiates at the tips of the AML and follows a roughly parabolic trajectory until it breaches the crustal surface several kilometers off-axis (Type B2; Figure 23c). As inferred from the comparison of modeled and observed off-axis pillow mound sites, during eruptions like those described for Type-B2 magma may follow zones of pre-existing weakness, reaching the seafloor closer to the AST than predicted for a homogeneous crust.

An important implication of dual-pathway eruptions is that each type of eruption forms different volcanic products on the seafloor. Near-bottom observations in the study area have shown that the seafloor near the AST is paved mainly by lobate flows and partly by sheet flows [*Kurras et al.*, 2000; *Engels et al.*, 2002; *White et al.*, 2002]. Both types of flows are considered to be products of on-axis Type-A eruptions. Particularly voluminous flows may inundate the axial trough and travel off-axis for many kilometers [*Macdonald et al.*, 1989; *Gregg and Fornari*, 1998]. In contrast, off-axis Type-B2 eruptions are associated with pillow mounds formed over eruptive vents [e.g., *Perfit et al.*, 1994; *Macdonald et al.*, 1996]. In the dual-pathway eruption model, the combination of these on-axis and off-axis eruptions contributes to the rapid thickening of seismic layer 2A on the EPR. While episodic Type-B2 dike eruptions produce pillow mounds on the ridge flank a few kilometers from the ridge axis (Figure 25-I), more frequent Type-A eruptions produce lobate flows at the AST and pave the ridge flank. On-axis eruptions occasionally produce long lava flows that are blocked by the pillow mounds constructed by previous Type-B2 eruptions, producing ponded lobate flows on the inward-facing sides of the mounds (Figure 25-II). While more lava from the AST paves the ridge flank, the pillow mounds and accumulated lobate flows are rafted away by seafloor spreading (Figure 25-III). More pillow mounds are formed by Type-B2 eruptions, and again produce topographic barriers for lava flows sourced at the ridge axis (Figure 25-IV). Some flows from the on-axis eruption may inundate the pillow mound (Figure 25-V). As this process is repeated, layer 2A reaches its full thickness within a few kilometers of the ridge crest (Figure 25-VI-VIII). In combination with inward-facing faults, the off-axis pillow mounds create the barriers necessary to allow ponded on-axis flows to rapidly thicken the extrusive layer of the oceanic crust within a few kilometers of the EPR axis.

Observations from the DSL-120A sidescan data and SeaBeam bathymetry support the dual-pathway eruption model. In the area between 9°53'-58'N, the Cocos plate exhibits two series of large-scale pillow mounds 2 and 3 km off-axis (Plate 1b). Ridge-perpendicular bathymetry profiles produced from SeaBeam data show that the inner and outer groups of pillow mounds have Type-1 and Type-2 profiles (Figure 9), respectively. Based on my model, the inner group was formed in the most recent series of Type-B2 eruptions; the Type-1 profiles of the pillow mounds in this group are due to the fact that the pillow mounds have not yet been inundated by long lava flows from the ridge axis (Figure 25-I). On the other hand, Type-2 profiles of the pillow mounds in the outer group suggest that Type-A lava flows ponded against the on-axis side of the pillow mounds before the inner group was formed (the closest pillow mound from the AST on Figure 25-VI).

To check whether this dual-pathway model is reasonable, I estimated the frequency of Type-B2 eruptions. SeaBeam bathymetry data show that large-scale pillow-mound heights range between 20-80 m in the study area. I assume a Type-B2 eruption site 3 km from the AST, with eruptions occurring at constant time intervals and forming pillow mounds with an average height of 50 m. I also assume that lava produced by Type-A eruptions would fill the seafloor between the AST and the pillow mounds, accumulating up to the summit of the pillow mounds. Using the full-spreading rate of 110 mm/y [*Klitgord and Mammerick*, 1982; *Carbotte and Macdonald*, 1992], approximately seven layers of accumulated Type-A flows are required to produce to a 200-m thick layer 2A at the eruptive vent 3 km off-axis. This results in a maximum Type-B2 eruption interval of ~7 ka. Based on this estimate, if the pillow mounds have not been covered with lava flows from on-axis eruptions, they should be observed with an average spacing of ~400 m beyond the Type-B2 eruptive site. As mentioned above in the discussion of pillow-mound profiles, the two series of large-scale pillow mounds between 9°53'-58'N on the Cocos plate observed in the sidescan data appear to have formed in separate Type-B2 eruptions. These pillow mounds are spaced ~1 km apart, consistent with the calculated spacing given that eruption intervals fluctuate. Thus, the estimated off-axis eruption frequency supports the dual-pathway eruption model for the doubling the thickness of seismic layer 2A on the EPR.

This discussion of off-axis eruption frequency raises a question about the volume of lava produced via off-axis volcanism. Although most of the magma on the

EPR erupts at the AST, it has been proposed that the contribution of off-axis volcanism to the crustal accretion process is appreciable [*Perfit and Chadwick*, 1998]. One large-scale pillow mound 20-m high at 9°30'N depicted in the sidescan data and observed during submersible dives requires approximately 7.9 x 10^6 m^3 of lava. Compared to this estimated volume, Gregg et al. [1996] report that the 1991 on-axis eruption between 9°46'-51'N produced 4 x 10^6 – 6 x 10^6 m^3 of lava. This rough estimate suggests that the volume of lava erupted off-axis is similar to the volume of lava erupted during a single event on the ridge axis. This indicates that off-axis eruptions are, by themselves, unable to account for the rapid thickening in seismic layer 2A; rather, it is the combination of off-axis eruptions and ponded flows that erupt from the axis that account for the increase in thickness.

6.3 Limitations of the dual-pathway eruption model

The proposed dual-pathway eruption model is built upon observations derived from the first high-resolution, comprehensive sidescan dataset covering both the axis and the flanks of the EPR, as well as results of TWODD simulations of the stress field in the oceanic crust. The model agrees well with observed ridge-perpendicular pillow-mound bathymetric profiles and is consistent with estimated off-axis eruption frequencies. However, it does not explain certain features observed in the sidescan data or some aspects of layer 2A thickening observed in across-axis seismic profiles.

As described in chapter 3, 44.5% of the lobate-dominated regions are bounded by inward-facing faults 1-2 km away from the AST, while only 15.5% are bounded by large-scale pillow mounds. This shows that inward-facing faults are more likely to be responsible than Type-B2 pillow mounds for blocking Type-A lava flows. In addition, a few pillow mounds, including the largest in the study area (Figure 13), occur in deep grabens and therefore do not form significant barriers to Type-A lava flows. Although these pillow mounds make up only a small fraction of the total pillow-mound population, they probably do not contribute to the thickening of seismic layer 2A. Furthermore, while the sidescan data show that pillow mounds become abundant after a distance of 3 km from the AST (Figure 11), seismic layer 2A often attains its full thickness within 1.5-3.0 km of the AST [Figure 4; *Harding et al.*, 1993]. Thus, dual-pathway eruptions may not be the dominant process for the thickening of layer 2A. On the other hand, the small fluctuations in the thickness of layer 2A depicted in the across-axis seismic profiles may represent discrete pillow mounds that have retained their original Type-1 bathymetric profiles.

Hooft et al. [1996] proposed a stochastic model for the emplacement of dikes and lava flows at the AST to explain the rapid thickening of seismic layer 2A without any blocking mechanism. This model is based on a bimodal distribution of lava flows. They suggest that frequent short flows confined in the AST and occasional long flows from the AST traveling via lava tubes and breaching to the surface a few kilometers off-axis build up layer 2A. According to their model, 95% of the total erupted lava volume is confined in the AST; only 5% of the lava that makes up layer 2A comes from the long flows that appear as off-axis eruptions. This ratio is in agreement with the observed areal coverage of the pillow mounds in the study area, which is approximately 4%. However, the model proposed by Hooft et al. [1996] requires the mean volume of each long lava flow to be ~20 times that of a short flow. Such voluminous off-axis flows are not observed in my study area. Furthermore, Hooft et al. [1996] assume a uniform flow thickness with a thinning of accumulated layers with increasing distance off-axis. These assumptions contradict terrestrial observations, for example, at Mauna Loa, Hawaii, where lava flows are observed to increase thickness towards a distal end of the flow [*Lipman and Banks*, 1987]. It therefore seems likely that a combination of the dual-pathway and stochastic models best accounts for the rapid thickening of seismic layer 2A on the EPR.

6.4 Recommendations for future investigations

Data, simulations, and analyses have been presented that support the dual-pathway eruption model for the rapid thickening of seismic layer 2A on the EPR; however, the fact remains that few on-axis and no off-axis eruptions have ever been witnessed. The model developed in this thesis for dual-pathway eruptions would benefit from additional study, and I therefore conclude with some suggestions for future investigations. (1) Determining the age differences or stratigraphic relationships between off-axis pillow mounds and the flows that accumulate on their inward-facing slopes would constrain the model. If the dual-pathway model is correct, the pillow flows should be older than the ponded flows. (2) Additional, extensive mapping outside of the study area with instruments that could both image the seafloor and penetrate into shallow sediment layers could reveal stepwise increases in the amount of sediment cover that are predicted by the dual-pathway model. My model predicts that the seafloor between the ridge axis and the nearest large-pillow mound is constantly repaved with lava flows from the AST. Sediment starts to accumulate in this region when a new pillow mound is formed on the on-axis side of the existing pillow mound. Based on the sedimentation rate of 16 m/10^6 yr [*Lonsdale and Spiess*, 1980] and the estimated longest interval for the off-axis pillow mound formation of 7 ka, the sediment thickness would increase in steps of approximately 11 cm from one pillow-mound-bounded region to the next with increasing distance from the ridge axis. 3) Additional TWODD simulations will undoubtedly provide insights into the processes that cause the alternation of pathways between Types A and B2, further refining the hypothesis.

APPENDIX A: Tables

Table Captions

Table 1:

Values for TWODD calculations. Bold values are the ones used in the final simulations.

Table 2:

Table showing dimensions and geometry of the melt lens used in TWODD simulations.

Table 3:

Table showing characteristics of two types of pillow mounds observed in the study area.

Table 1

	Symbol	Magnitude	Dimensions
Density of water	ρ_w	1,000	kg/m^3
Density of crust	ρ_c	**2,500**-2,950[*1]	kg/m^3
Gravitational acceleration	g	-9.8	m/s^2
Full wavelength of the sinusoidal variation of the stress components	L	**200**-3,600	km
Maximum values of normal component at the bottom	A	0-$\mathbf{10^3}$	Pa
Maximum values of shear component at the bottom	B	$\mathbf{10^8}$-10^{10}	Pa
Young's modulus	E	2.5×10^{10}	Pa
Poisson's ratio	ν	0.25	n/a
Maximum vertical opening of a sill	ΔU_{max}	10-50[*2]	m

*1: e.g., Christeson et al., 1996
*2: e.g., Kent et al., 1993

Table 2

Geometry and dimensions of the AML				Distance (km) to a modeled off-axis eruption site [*3]			Distance (km) to the observed nearest large pillow mound [*4]	
Latitude [*1]	Half-width (m)*1	Depth (km)*2	Symmetry across the ridge axis [*1]	Pacific	Cocos	No AML offset	Pacific	Cocos
9°50'N	250	1.4	Offset to East for 250 m	4.5	5.0	4.75	3.0	3.4
9°45'N	250	1.5[#]	Offset to East for 100 m	4.9	5.1	5.0	1.7/3.2	3.4
9°40'N	350	1.6	Offset to West for 200 m	5.4	5.0	5.2	3.3	None (2.5)
9°35'N	125	1.6[#]	symmetric	5.2	5.2	5.2	3.5	None (2.5)
9°30'N	600	1.7	Offset to West for 500 m	5.9	4.9	5.4	None (3.0)	1.7/3.0

*1: Kent et al., 1993.

*2: Estimated minimum axial melt lens depth below the ridge crest from Kent et al., 1993.

#: Estimated minimum melt lens depth may be biased due to the uncertainty of layer 2A depth [*Kent el al.*, 1993].

*3: Results of TWODD analysis.

*4: Results from the DSL120A sidescan data. The second value is the distance to the next nearest pillow mound. The number in parentheses is the distance to the survey boundary.

Table 3

Type	Shape	Basal diameter	Height	Distance from AST
Small-scale pillow mound	oval	≤ 0.5 km	≤ 30 m	≤ 0.2 km
Large-scale pillow mound	oval to ridge	> 0.5 and ≤ 2.5 km	20-80 m	≥ 1.5 km

APPENDIX B: Figures

Figure Captions

Figure 1:

Map showing the location of the study area relative to major plate boundaries and continental landmasses.

Figure 2:

Representative photographs of lava flow morphologies in the study area: a) and b) pillow flows; c) lobate flows; and d) sheet flows. Scale for c) and d) are the same.

Figure 3:

Interpretative cross-sectional diagram of layers constructing the oceanic crust and the magma reservoir below the EPR 9°-10°N. Modified from Sinton and Detrick [1992].

Figure 4:

Across-axis profiles of the thickness of seismic layer 2A for the EPR 9°50'N and 9°30'N. Modified from Harding et al. [1993].

Figure 5:

Photographs of survey instruments used during the AT7-4 cruise; a) DSL-120A; b) ABE; and c) deep-towed camera system.

Figure 6:

Schematic diagram showing the sonar signal paths that DSL-120A sends out and receives. Sonar swath and nadir are labeled. Modified from http://www.divediscover.whoi.edu.

Figure 7:

Map showing survey boundaries of DSL-120A and ABE data plus track lines for camera tows and *Alvin* dives.

Figure 8:

Plot showing the basal diameter of pillow mounds verses pillow mound location as a function of distance from the AST for both Pacific and Cocos plates. The basal diameter of a pillow mound is measured on the long axis, which generally trends nearly parallel to the EPR axis. Pillow mounds with a basal diameter less than 200 m are not included.

Figure 9:

Type 1 (a) and Type 2 (b) ridge-perpendicular bathymetric profiles of pillow mounds observed in the study area derived from SeaBeam bathymetry [*Cochran et al.*, 1999]. Profiles not to scale.

Figure 10:

DSL-120A sidescan data between 9°46' and 9°50'N at a spatial resolution of 2 m showing changes of across-axis seafloor morphology with respect to distance from the AST.

Figure 11:

Histogram showing the across-axis distribution of pillow mound areal coverage calculated as a percentage of the total bin area in 500 m-wide corridors. The 3.5-4.0 km bin on the Cocos plate is colored differently from the rest to indicate that there is no counterpart on the Pacific plate.

Figure 12:

Summary maps for small-scale pillow mounds at the 9°37'N area showing (a) DSL-120A sidescan data at 2-m spatial resolution, (b) an enlargement of the region in the blue box in (a) overlaid with photographic data collected by *Alvin* dives 3525 and 3528 (Photo analysis by Engels et al. [2002]), and (c) bathymetric profiles constructed from *Alvin* altimeter data shown with photo analysis. Profile A is shown with the original depth data. The other profiles are shown with a vertical offset of 15 m for each profile.

Figure 13:

Maps for R4 showing pillow mounds in the outermost group and the northern three mounds of the middle group. (a) DSL-120A sidescan data at a spatial resolution of 2 m with interpretation, and (b) SeaBeam bathymetry [*Cochran et al.*, 1999] contoured at 10 m intervals with interpretation.

Figure 14:

Histogram showing the along-axis distribution of pillow mounds in the study area. Vertical dimension of each bar represents 1-km distance along-axis. On each histogram, the left and right sides represent the data for the Pacific and Cocos plates, respectively. (a) and (b) The pillow mound coverage is calculated as a percentage of the total area in each 1 km bin for the regions <1.5 km and >1.5 km from the ridge axis. (c) Pillow mound coverage by area (red bars) within the total survey area (light yellow bars). The *x*-axis represents area in km^2. The latitude and the 3^{rd} order segments are labeled on the *y*-axis. The 3^{rd} order segments are labeled as OSC1-3 and S1-3, OSC (over spreading center) and S (segment), following the definition by Macdonald et al. [1998] and White et al. [2002].

Figure 15:

Schematic diagram depicting the formation of off-axis pillow mounds by off-axis dike intrusion: a-stage 1) Formation of two zones of maximum tensile stress at the seafloor on either side of a dike plane [after *Mastin and Pollard*, 1988]; b-stage 2) A graben develops between these zones. Lava erupted from a fissure either constructs a pillow mound on the graben floor (top) or overflows the graben (bottom). Cross-sectional (top) and plan (bottom) views are shown for each case; c-stage 3) Subsequent on-axis flows fill the seafloor between the AST and the pillow mound, ponding against the pillow mound barrier or the graben walls (bottom), or inundating the mound (top). Figure is not to scale.

Figure 16:

(a) Interpretative model of magma reservoir for the EPR in across-axis. Modified from Sinton and Detrick [1992]. (b) Conceptual model produced from the interpretative model for the TWODD analysis in this study. (c) Diagram showing the reference frame and the ridge geometry used in this study. The ridge is represented as a 0.5-km high and 20-km wide isosceles triangle with a slope of 3°. The area below the ridge surface is divided into sections I and II, with y_w and y_c representing the thickness of water column and crust, respectively.

Figure 17:

Diagram showing the absolute and relative displacements of the mantle with respect to the lithosphere at the base of the lithosphere. (a) Mantle convection currents at the upper part of the cell at $\alpha=90°$ and $\alpha=-90°/270°$ represent the relative displacement of the mantle to the lithosphere for the active and passive magma-upwelling models, respectively. Small horizontal and vertical arrows represent normal and shear tractions at the base of the lithosphere, respectively. Modified from Hafner [1951]. (b) An active mantle-upwelling model. (c) A passive mantle-upwelling model. Black arrows represent absolute displacement whereas green arrows represent the relative displacement of the mantle with respect to the lithosphere.

Figure 18:

Most compressive stress trajectories overlain with contours of the most tensile stress produced by two different ambient stress fields: (a) Body forces alone; and (b) Body forces with the superposed effects of normal and shearing tractions acting on the base of the crust.

Figure 19:

Normal (solid lines) and shear (dashed lines) tractions at the base of the crust necessary to produce the ambient stress field described in section 5.3. The black lines show the values for the base of the crust with a non-uniform thickness. The red lines represent the values for the base of the crust with a uniform thickness of 5 km.

Figure 20:

Compressive stress trajectories and stress magnitudes. A 350 m half-width sill represented by a thick black line segment with a uniform internal pressure (-9.5×10^8 Pa) is inserted at 2 km below the ridge crest slightly above the depth (2.1 km) where σ_2 trajectories turn to horizontal after superposing Hafner's stress onto the stress field induced by the body forces. (a) Most compressive stress trajectories. (b) Most compressive stress trajectories overlain with contours of the most tensile stress. (c) Most compressive stress trajectories overlain with contours of τ_{max}.

Figure 21:

Diagram showing (a) symmetric opening of a pressurized sill in an infinite body with arrows showing symmetric displacements of the sill walls; (b) asymmetric opening of a pressurized will with a free surface closer to the upper sill side with arrows showing asymmetric displacements of the sill walls; and (c) dimensions of a sill emplacement site and its trajectory. The thick line segment represents a sill. Dashed lines represent sill propagation trajectories. D is a distance from the ridge axis to the off-axis dike eruption site. H is a sill emplacement depth from the ridge summit. S is a half-width of the sill. S_{max} is the maximum horizontal half-width of the sill before the sill begins to propagate upward.

Figure 22:

Compressive stress trajectories overlaid with the most tensile stress. The most tensile stress is contoured for every 4 x 10^8 Pa. The original sill and its trajectory path are represented by a black line. (a) Both sill tips propagate laterally until the sill half-width reaches a width of 495 m from its original half-width of 350 m. (b)-(d) One of the sill tips continues to extend to the ridge surface while the other tip ceases to grow.

Figure 23:

Three possible pathways for magma to breach the seafloor from the axial melt lens simulated in the form of a sill: (a) Pathway propagating directly from the center of the sill to the ridge crest (Type A); (b) Pathway propagating from one of sill tips to the ridge flank (Type B1); and (c) Pathway propagating from both sill tips to the ridge flank (Type B2). The brown line segments represent a sill. Dashed lines represent the magma paths.

Figure 24:

Diagrams showing different ambient stress fields for Fialko's simulation and simulation 1 to 3: (a) Fialko's simulation has flat topography but no basal tractions and no water pressure; (b) Simulation 1 has flat topography and basal tractions but no water pressure; (c) Simulation 2 has flat topography, basal tractions, and water pressure; and (d) Simulation 2 has ridge topography, basal tractions, but no water pressure. The blue box and arrows represent water pressure and the basal tractions, respectively. Light and dark browns represent the oceanic crust and mantle, respectively.

Figure 25:

Diagram showing the dual-pathway eruption model producing the thickening of seismic layer 2A within a few kilometers from the AST. (I) Off-axis eruption forms a pillow mound on the ridge flank. (II) Lava erupted at the AST (e.g., lobate flows) inundates the AST, travels to the off-axis directions, and accumulates on the axis side of the pillow mound. (III) The pillow mound and accumulated lava flows are rafted away by seafloor spreading. (IV) A new off-axis dike erupts and forms another pillow mound in proximity to the first pillow mound site. (V) Some flows from the AST may inundate the pillow mound. (VI)-(VIII) Process I – III repeat and result in thickening of layer 2A at the off-axis eruption site. Figure is not to scale.

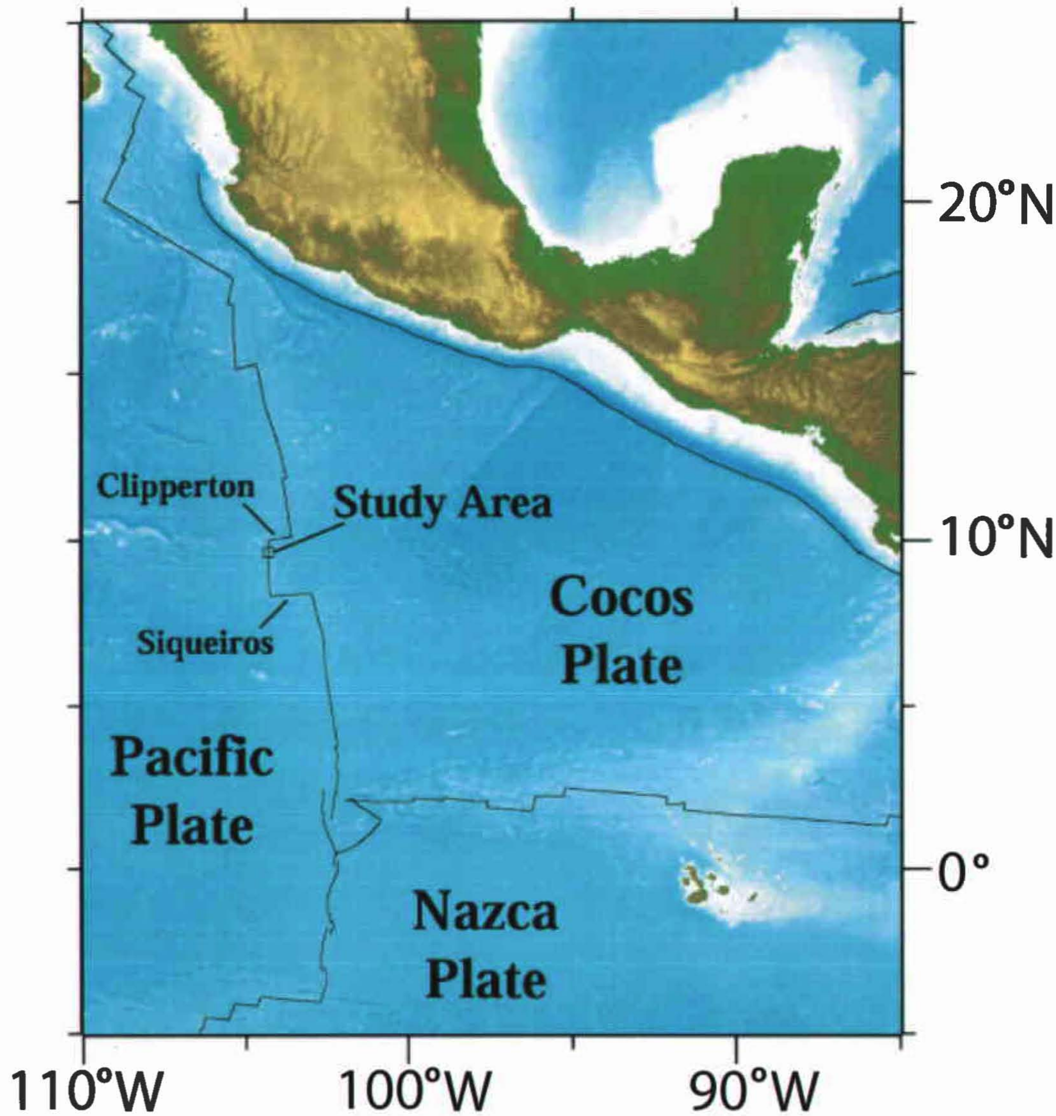
20°N
10°N
0°
110°W
100°W
90°W
Clipperton
Study Area
Siqueiros
Cocos
Plate
Pacific
Plate
Nazca
Plate

Figure 1

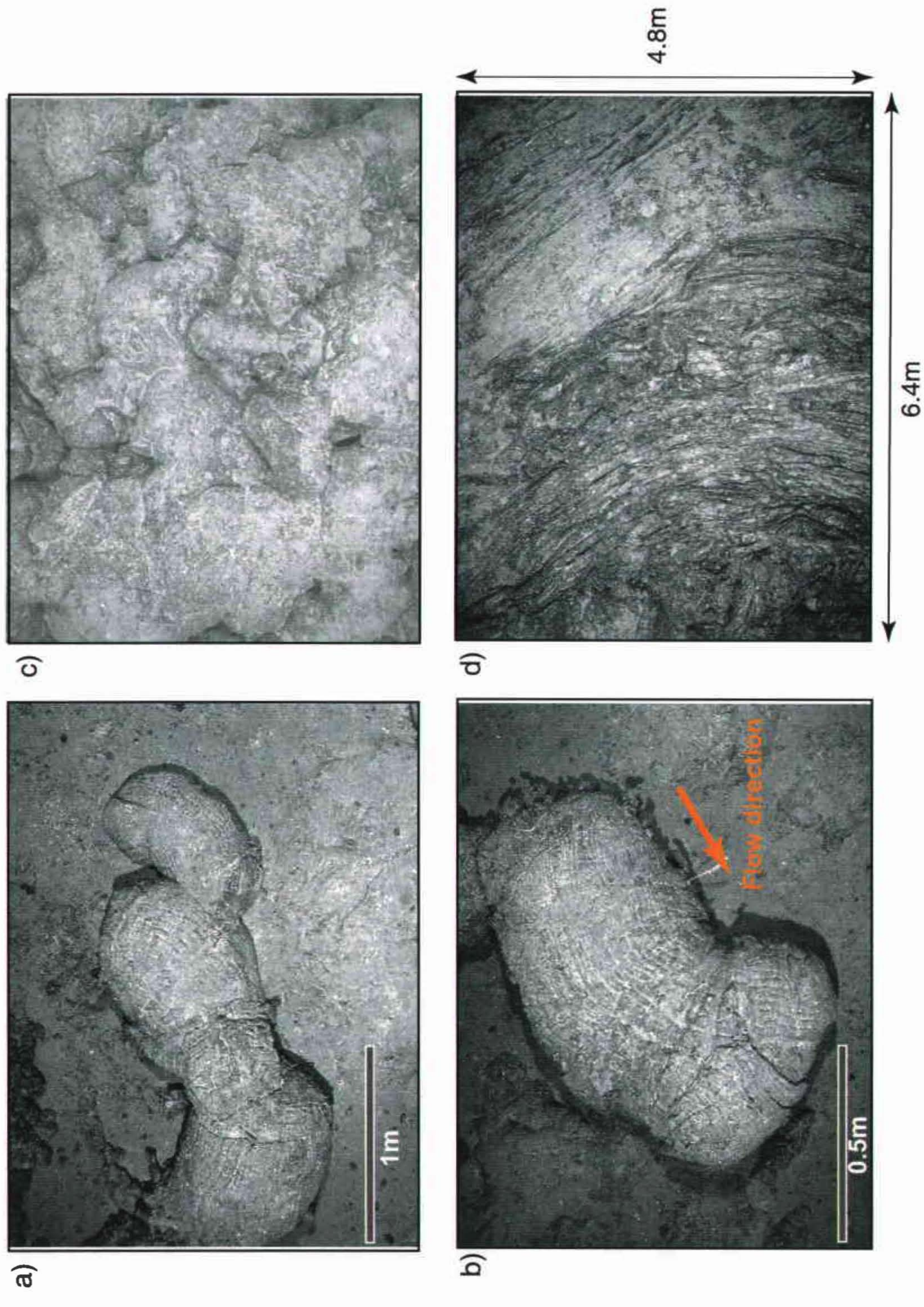

Figure 2

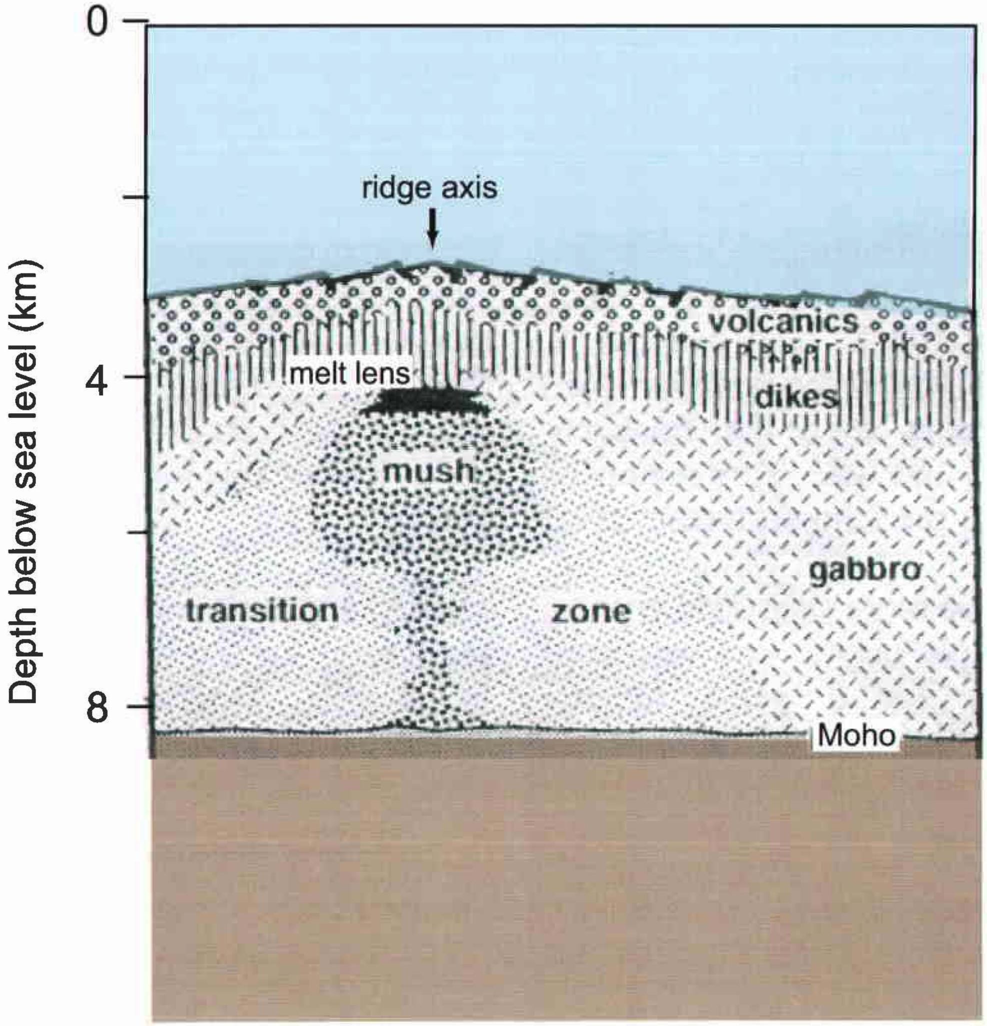
0
4
8
Depth below sea level (km)
ridge axis
volcanics
melt lens
dikes
mush
gabbro
transition
zone
Moho

Figure 3

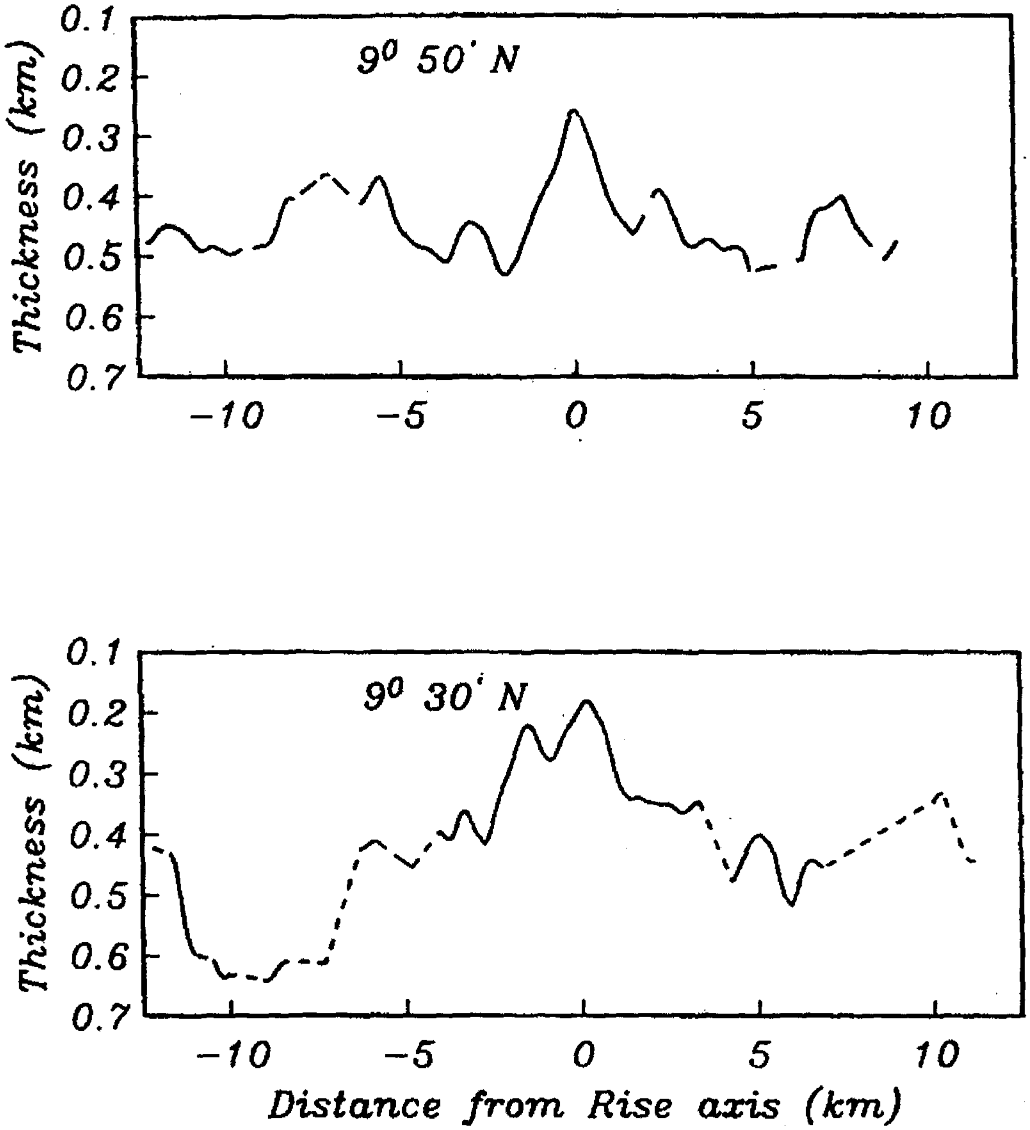
9⁰ 50' N
9⁰ 30' N
Thickness (km)
0.1
0.2
0.3
0.4
0.5
0.6
0.7
-10
-5
0
5
10
Distance from Rise axis (km)

Figure 4

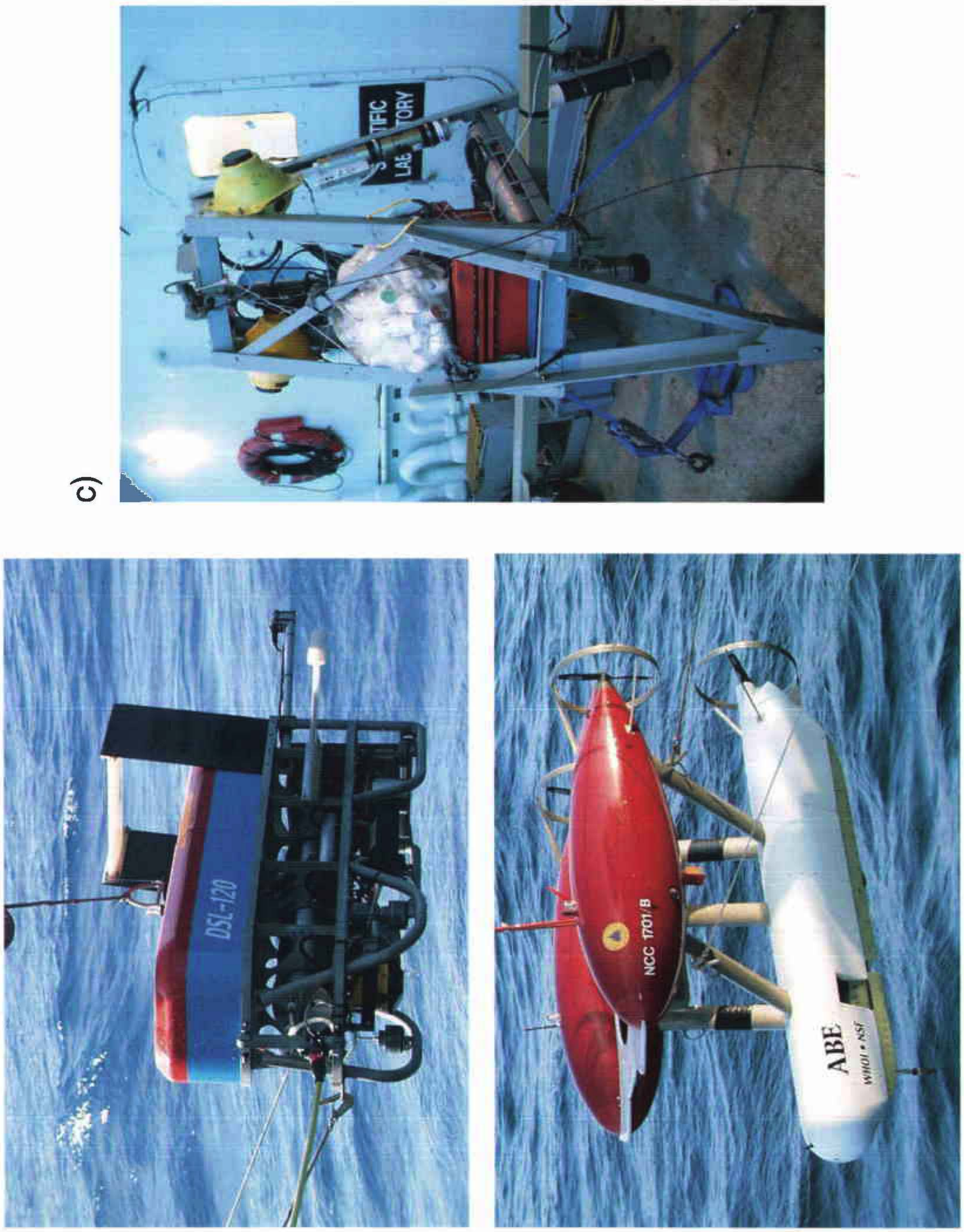

a) b) c)

Figure 5

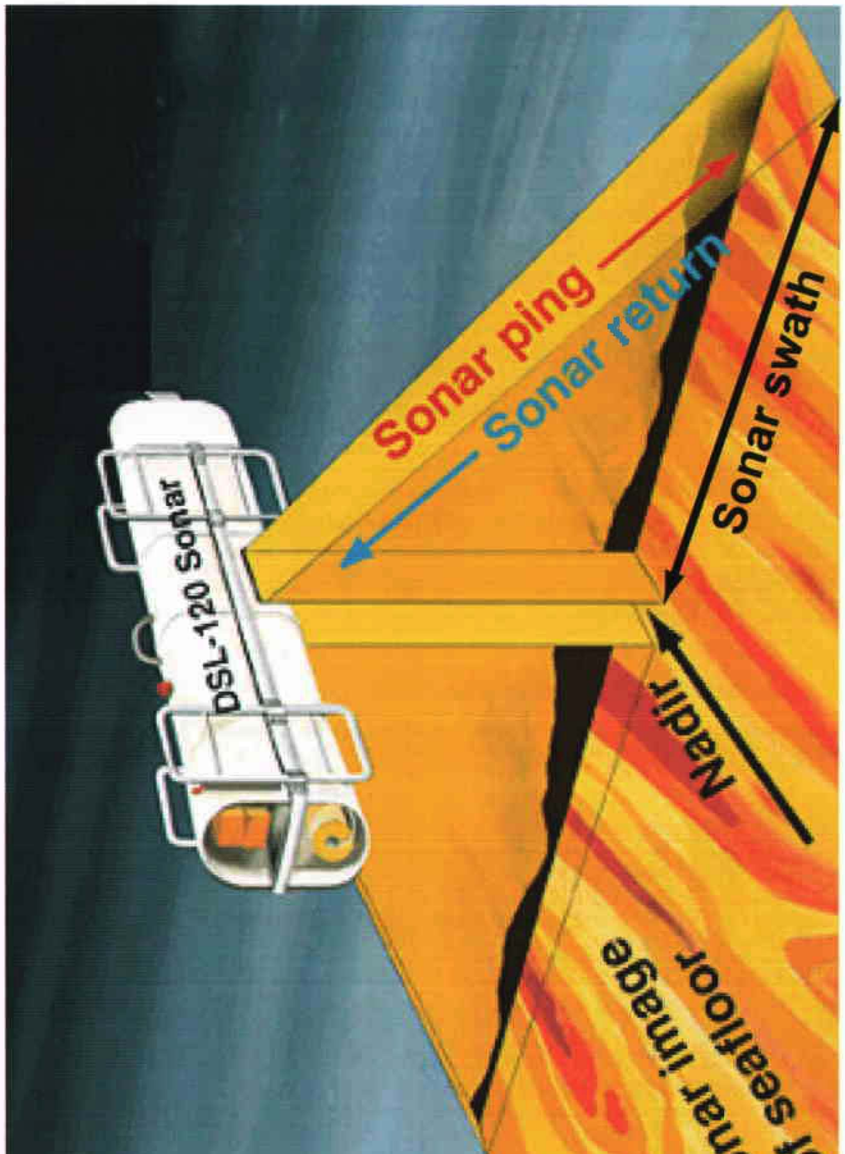
DSL-120 Sonar
Sonar ping
Sonar return
Sonar swath
Nadir
Sonar image
of seafloor

Figure 6

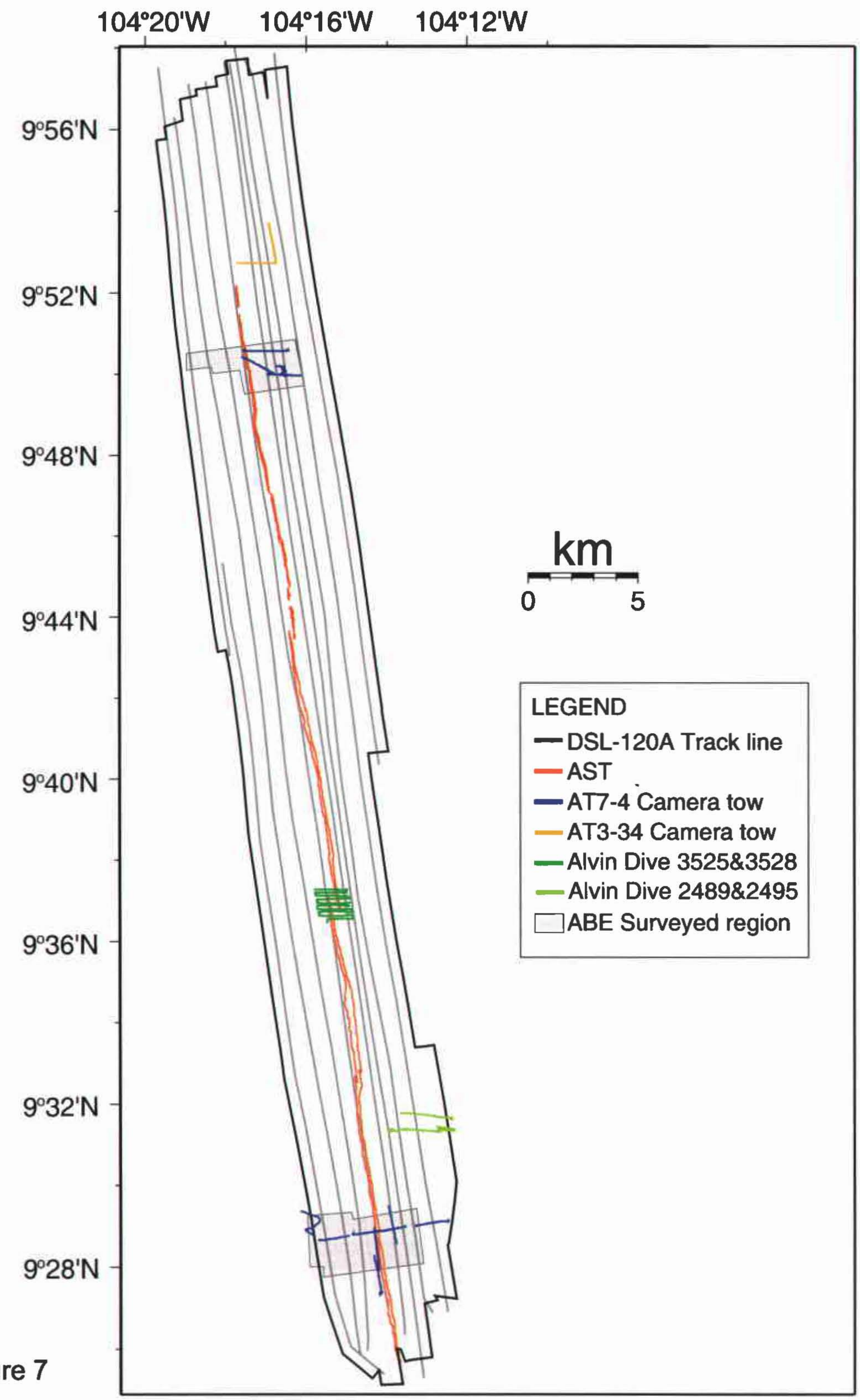
104°20'W
104°16'W
104°12'W
9°56'N
9°52'N
9°48'N
9°44'N
9°40'N
9°36'N
9°32'N
9°28'N
km
0
5
LEGEND
DSL-120A Track line
AST
AT7-4 Camera tow
AT3-34 Camera tow
Alvin Dive 3525&3528
Alvin Dive 2489&2495
ABE Surveyed region

Figure 7

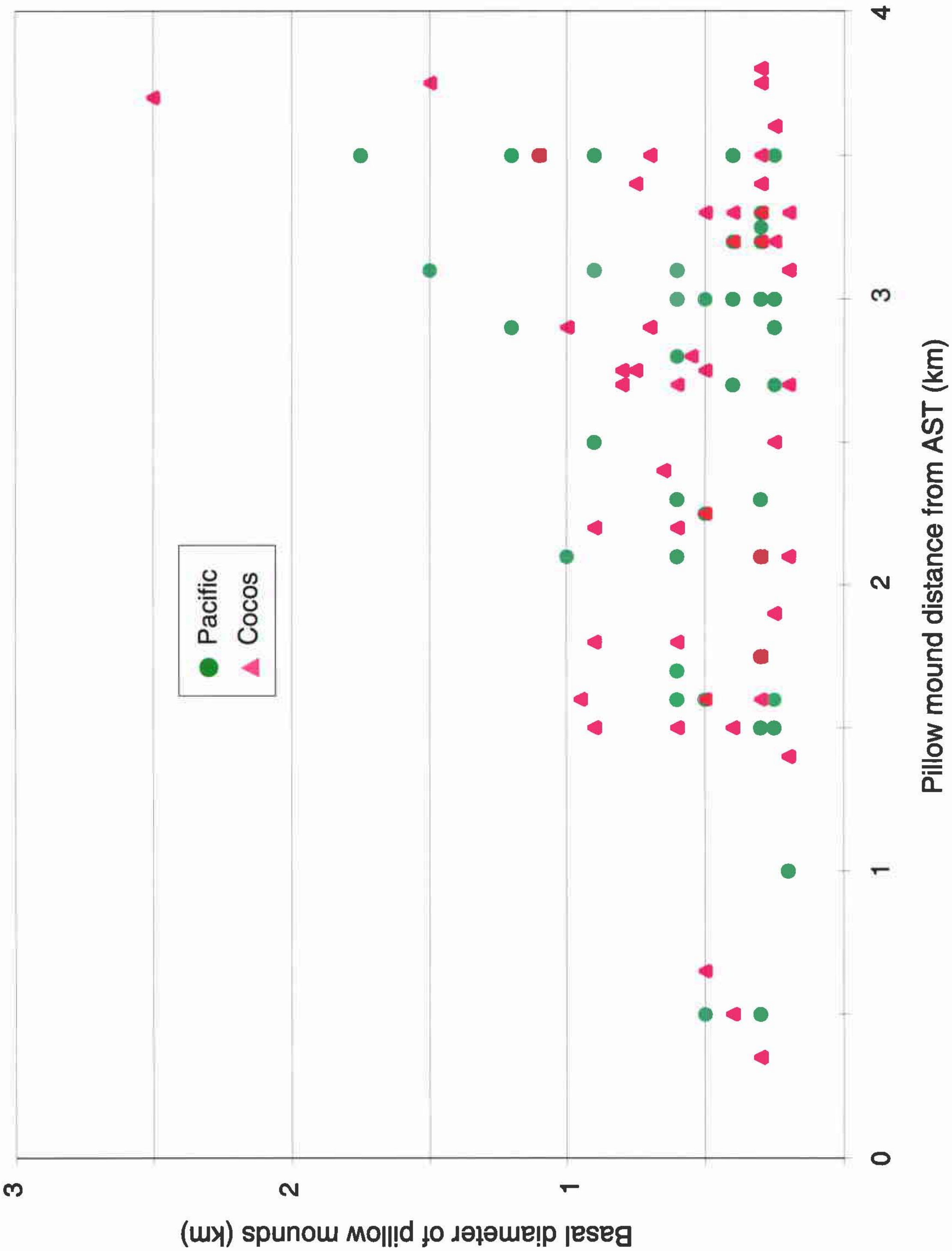
Pacific
Cocos
Pillow mound distance from AST (km)
Basal diameter of pillow mounds (km)
0
1
2
3
4
1
2
3

Figure 8

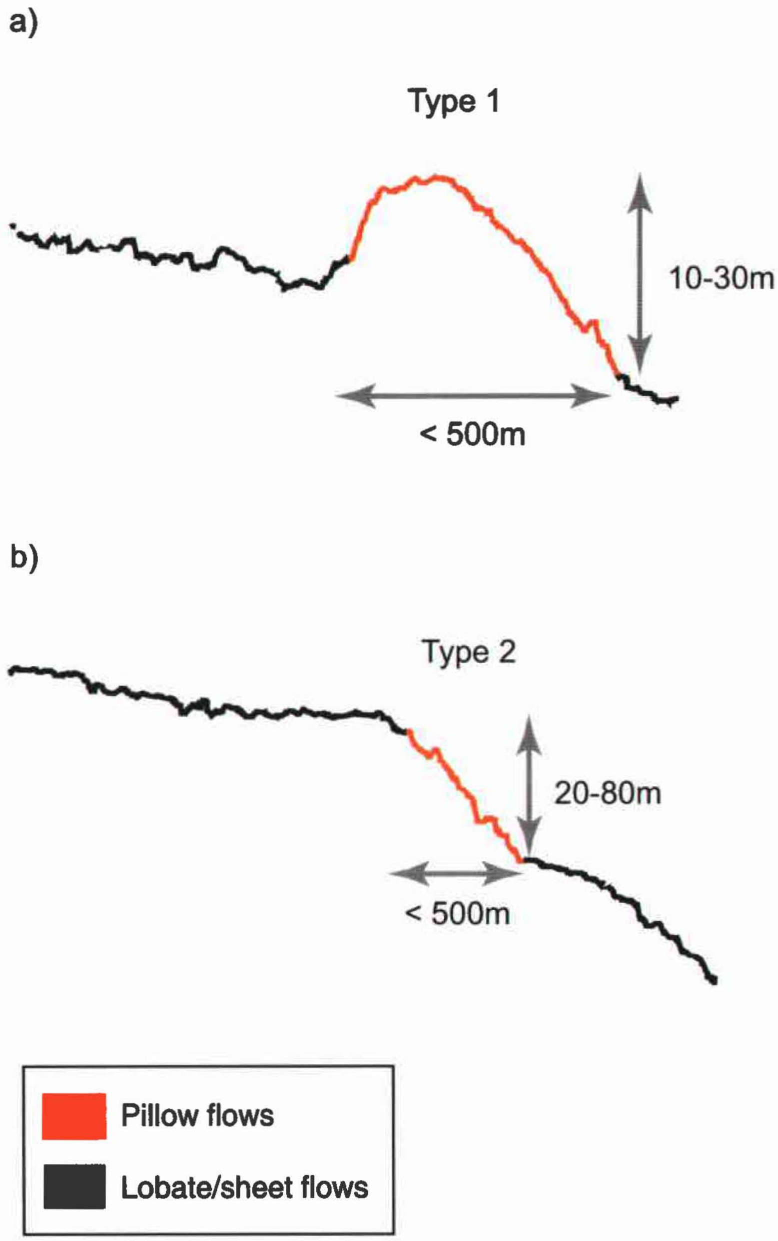
a)
Type 1
10-30m
< 500m
b)
Type 2
20-80m
< 500m
Pillow flows
Lobate/sheet flows

Figure 9

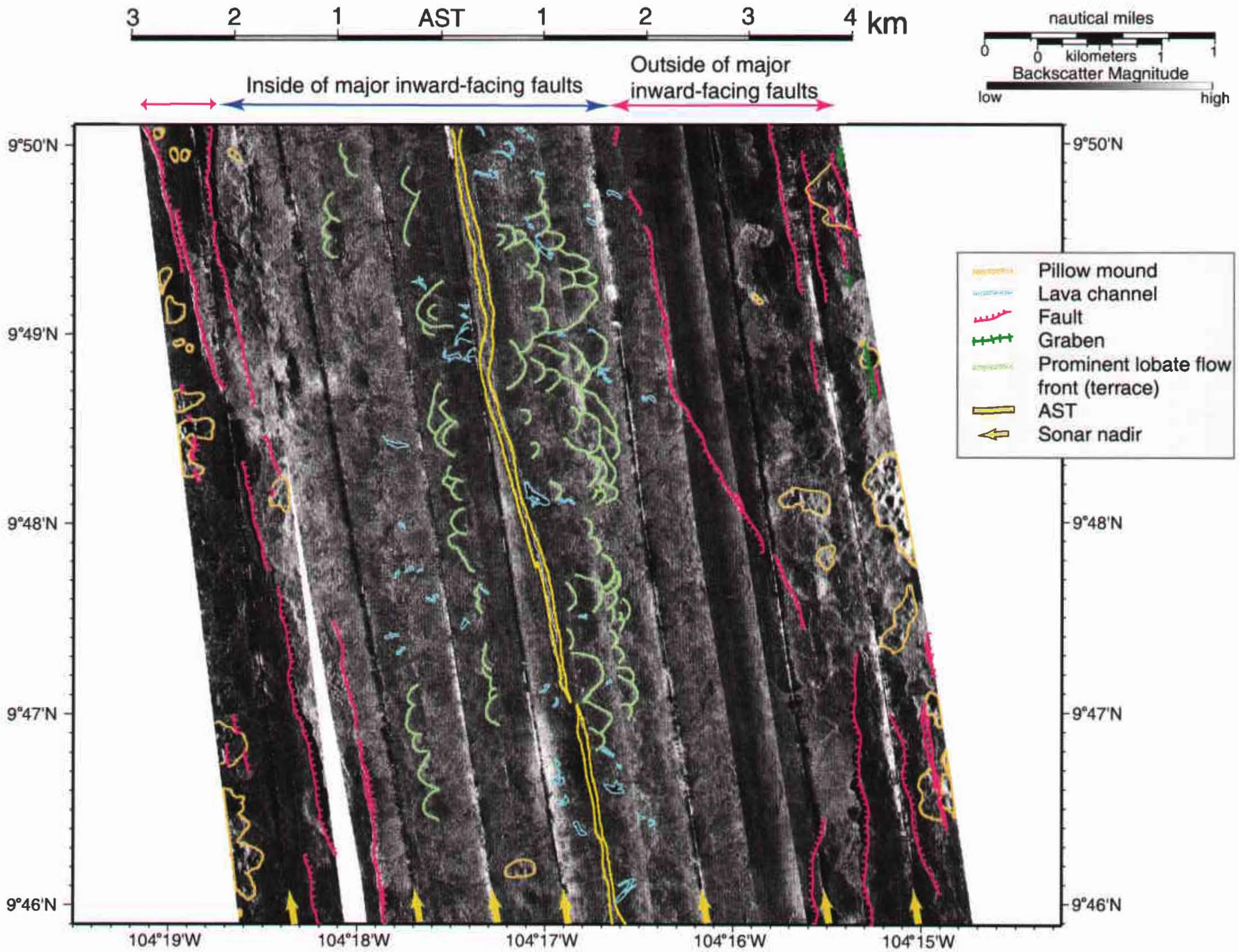
3
2
1
AST
1
2
3
4
km
Inside of major inward-facing faults
Outside of major inward-facing faults
nautical miles
0
1
0
kilometers
1
Backscatter Magnitude
low
high
Pillow mound
Lava channel
Fault
Graben
Prominent lobate flow front (terrace)
AST
Sonar nadir
9°50'N
9°49'N
9°48'N
9°47'N
9°46'N
104°19'W
104°18'W
104°17'W
104°16'W
104°15'W

Figure 10

Figure 11

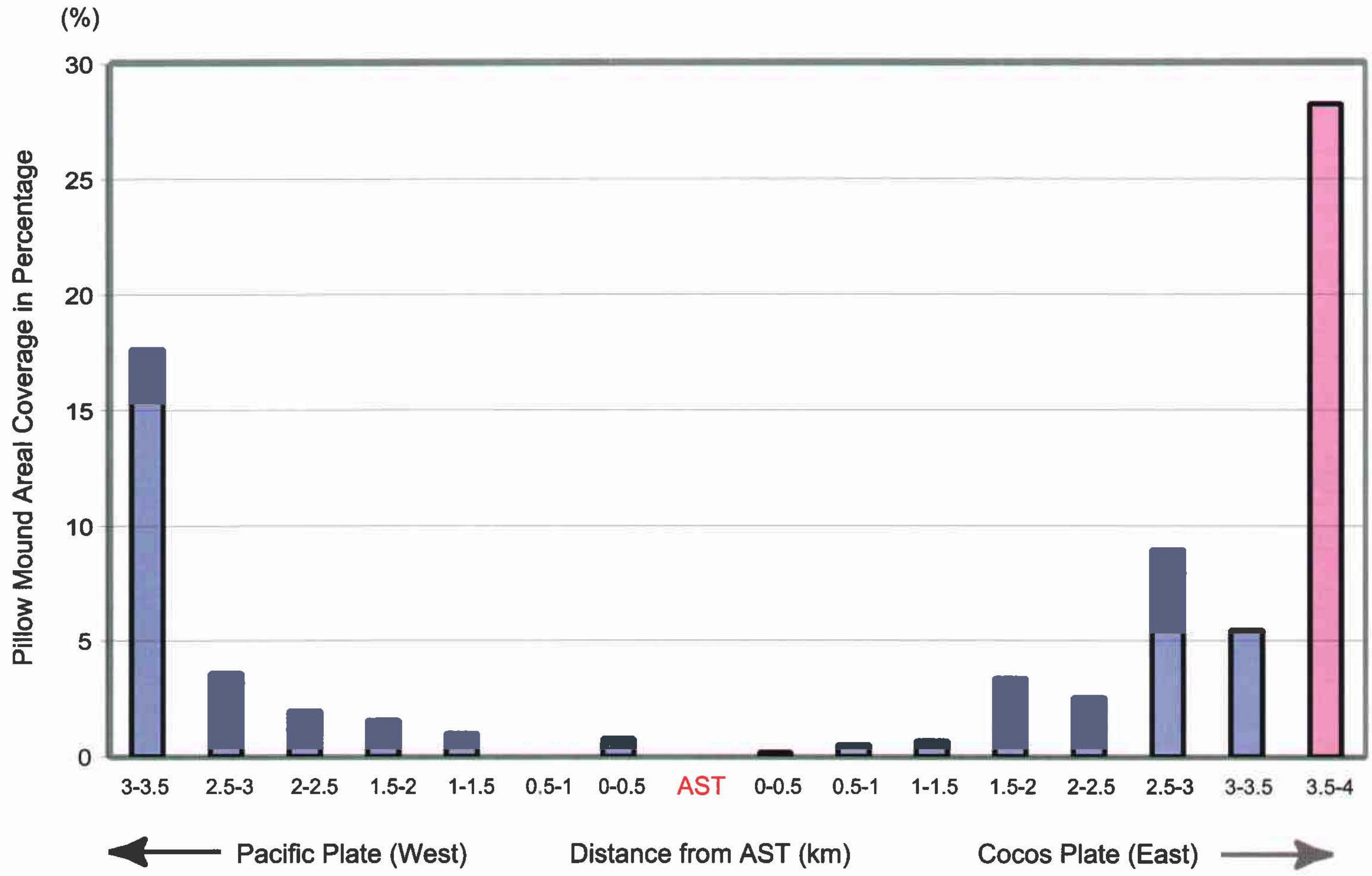

(%)
30
25
20
15
10
5
0
Pillow Mound Areal Coverage in Percentage
3-3.5
2.5-3
2-2.5
1.5-2
1-1.5
0.5-1
0-0.5
AST
0-0.5
0.5-1
1-1.5
1.5-2
2-2.5
2.5-3
3-3.5
3.5-4
Pacific Plate (West)
Distance from AST (km)
Cocos Plate (East)

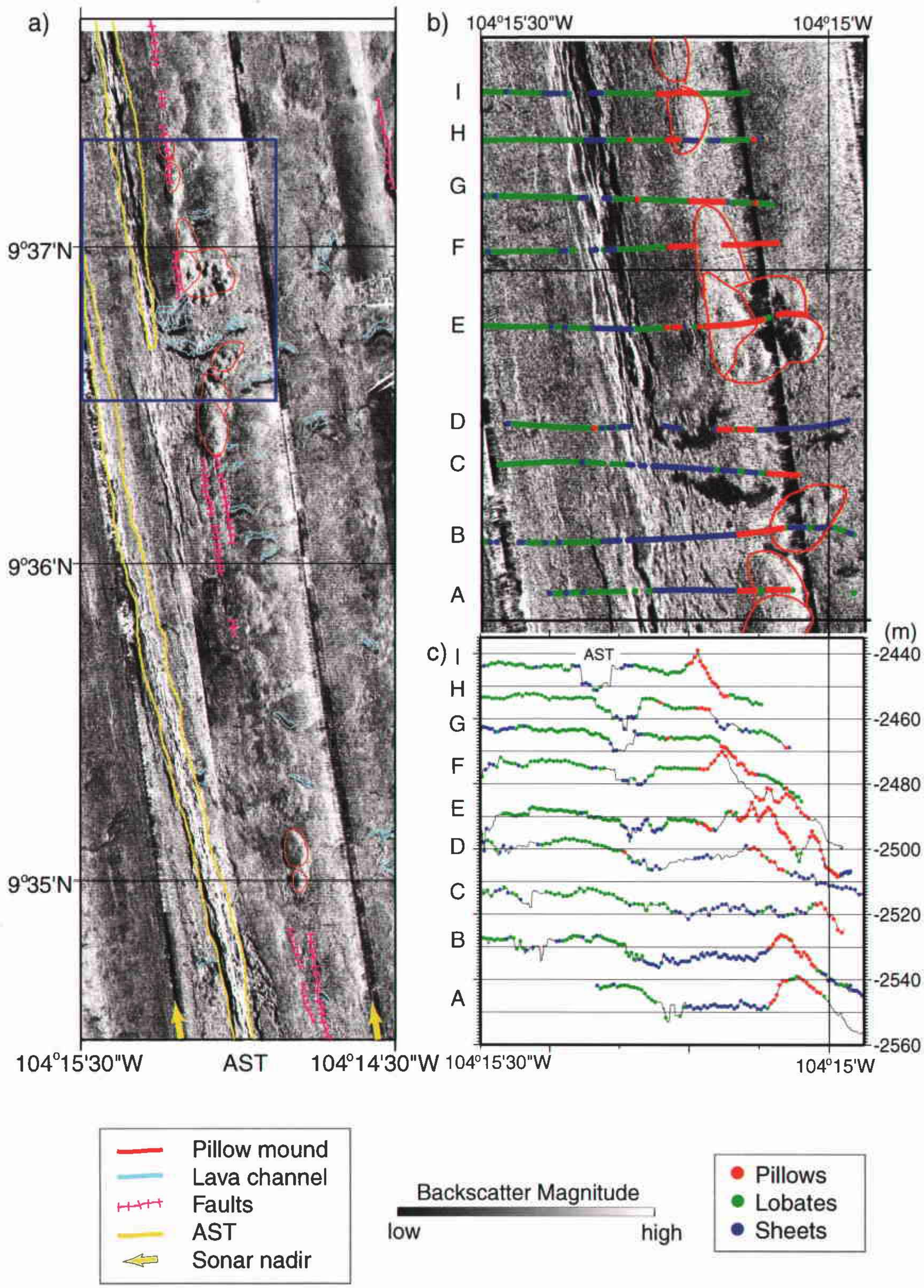

a)
b) 104°15'30"W
104°15'W
9°37'N
9°36'N
9°35'N
I
H
G
F
E
D
C
B
A
c)
AST
(m)
-2440
-2460
-2480
-2500
-2520
-2540
-2560
104°15'30"W
AST
104°14'30"W
104°15'30"W
104°15'W
Pillow mound
Lava channel
Faults
AST
Sonar nadir
Backscatter Magnitude
low
high
Pillows
Lobates
Sheets

Figure 12

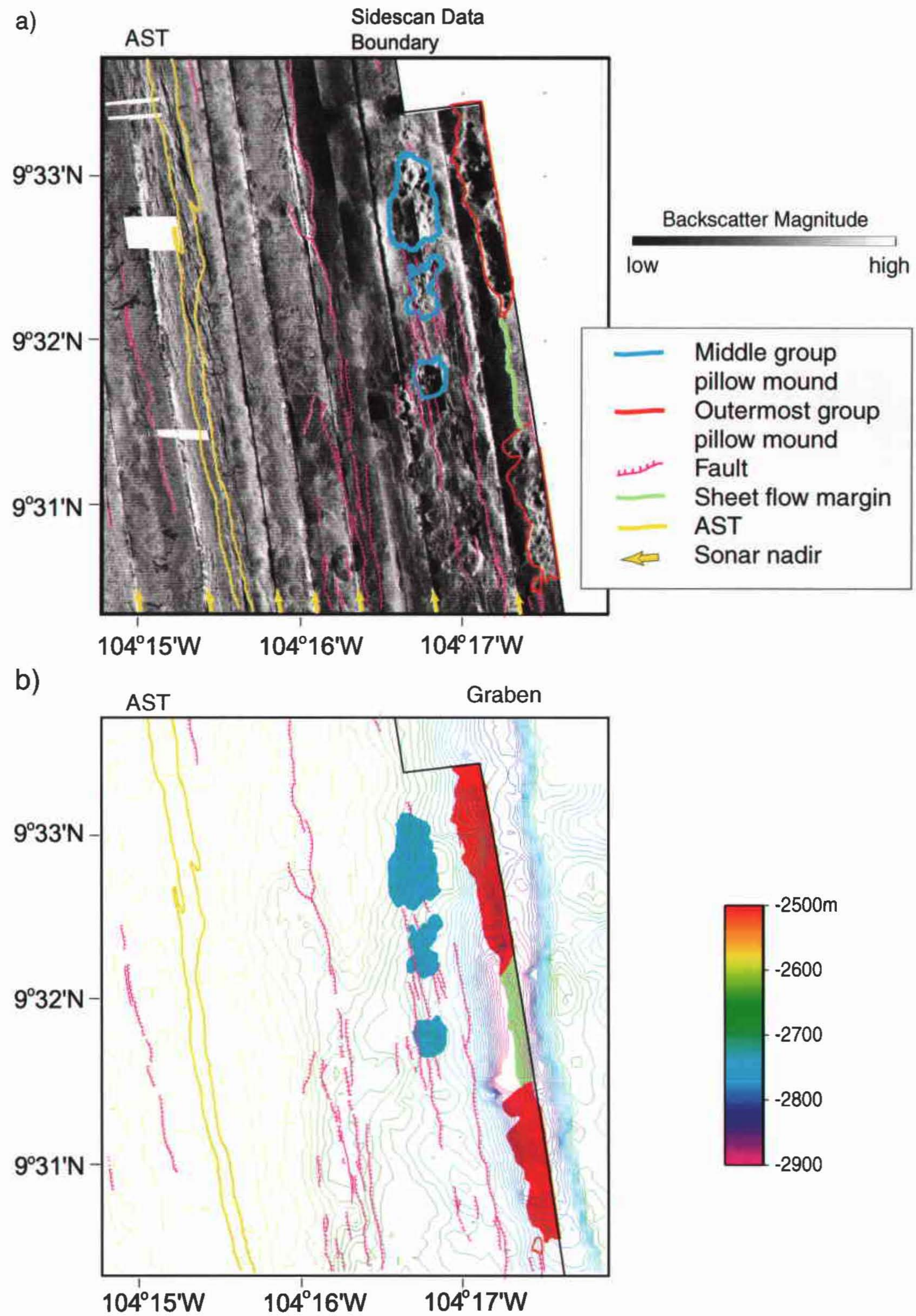

a)
AST
Sidescan Data
Boundary
9°33'N
9°32'N
9°31'N
Backscatter Magnitude
low
high
Middle group
pillow mound
Outermost group
pillow mound
Fault
Sheet flow margin
AST
Sonar nadir
104°15'W
104°16'W
104°17'W
b)
AST
Graben
9°33'N
9°32'N
9°31'N
-2500m
-2600
-2700
-2800
-2900
104°15'W
104°16'W
104°17'W

Figure 13

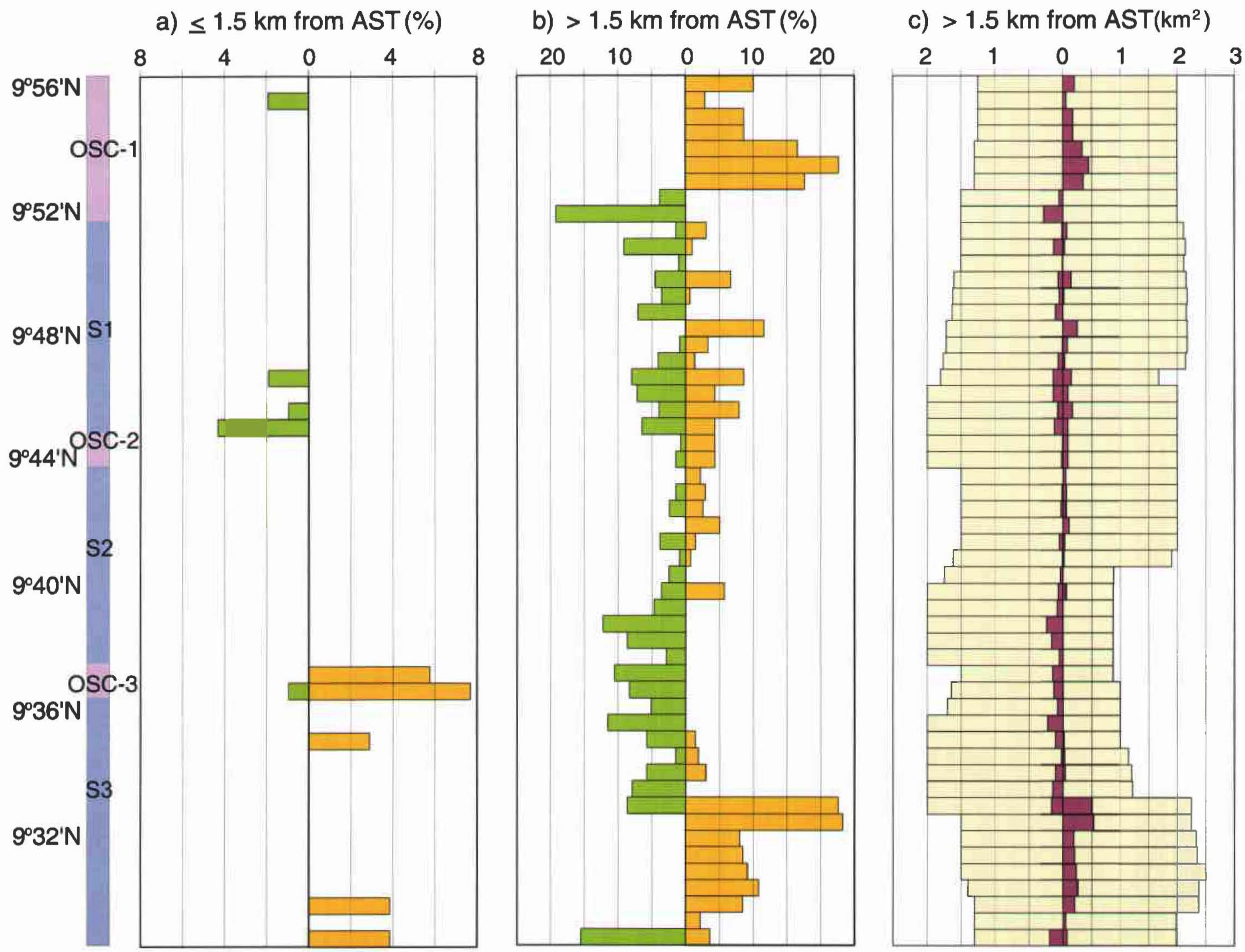
a) ≤ 1.5 km from AST (%)
b) > 1.5 km from AST (%)
c) > 1.5 km from AST (km²)
8
4
0
4
8
20
10
0
10
20
2
1
0
1
2
3
9°56'N
OSC-1
9°52'N
9°48'N
S1
OSC-2
9°44'N
S2
9°40'N
OSC-3
9°36'N
S3
9°32'N

Figure 14

Figure 15

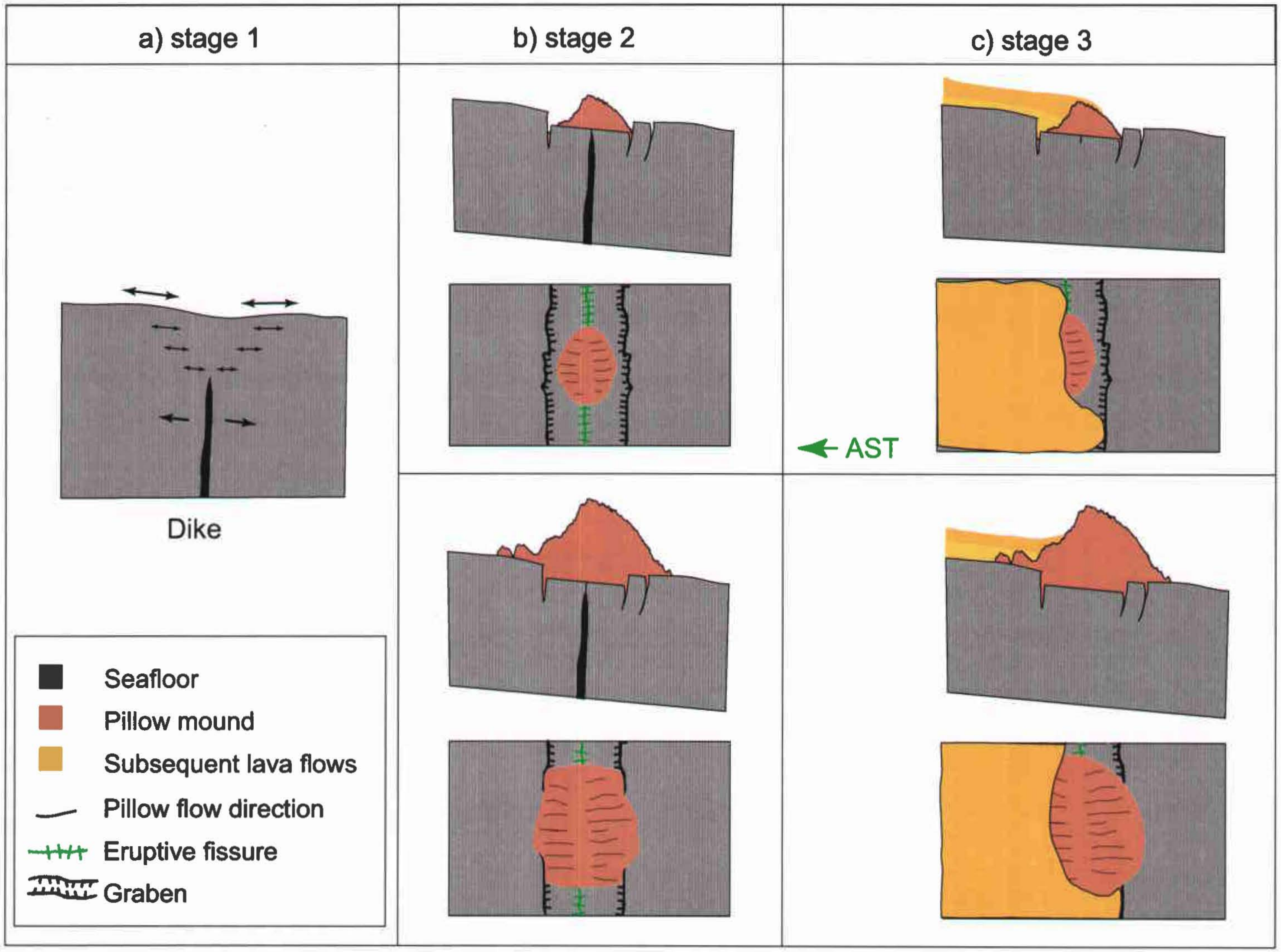

a) stage 1
b) stage 2
c) stage 3
Dike
AST
Seafloor
Pillow mound
Subsequent lava flows
Pillow flow direction
Eruptive fissure
Graben

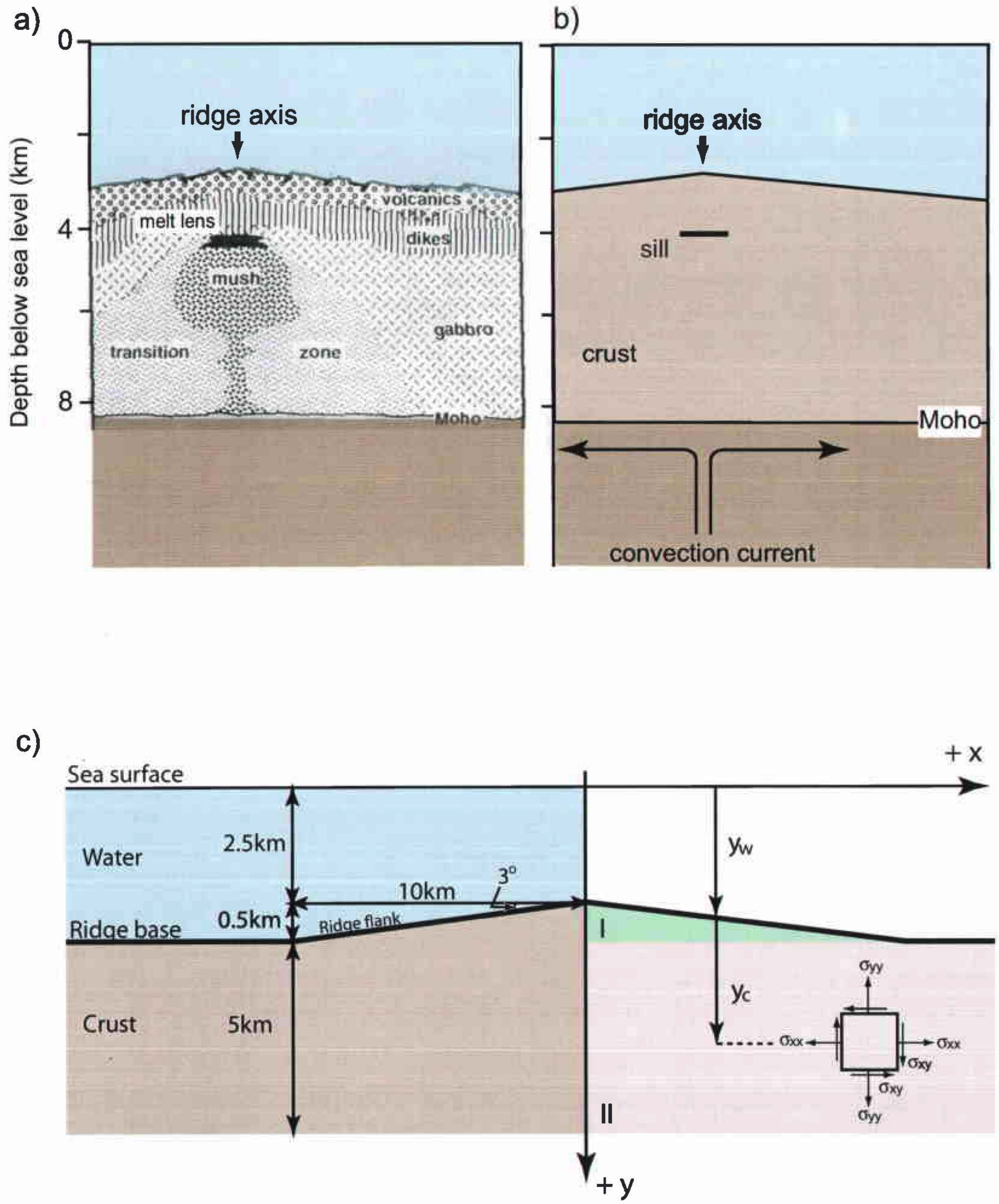

a)
b)
c)
Depth below sea level (km)
0
4
8
ridge axis
volcanics
melt lens
dikes
mush
gabbro
transition
zone
Moho
ridge axis
sill
crust
Moho
convection current
Sea surface
+ x
Water
2.5km
y_w
10km
3°
0.5km
Ridge base
Ridge flank
I
y_c
Crust
5km
σ_{yy}
σ_{xx}
σ_{xy}
II
+ y

Figure 16

Figure 17

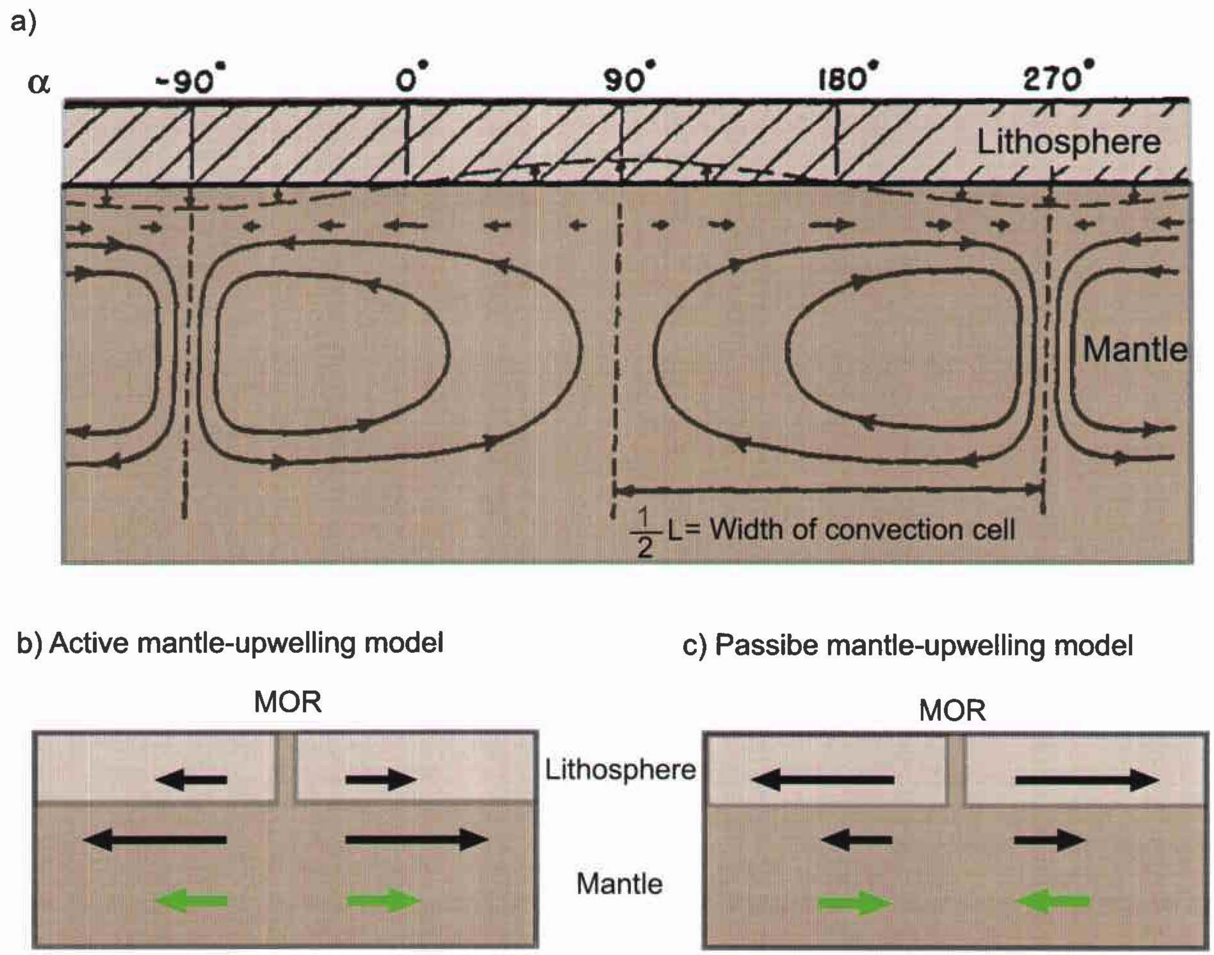
a)
α
-90°
0°
90°
180°
270°
Lithosphere
Mantle
$\frac{1}{2}$L= Width of convection cell
b) Active mantle-upwelling model
MOR
Lithosphere
Mantle
c) Passibe mantle-upwelling model
MOR

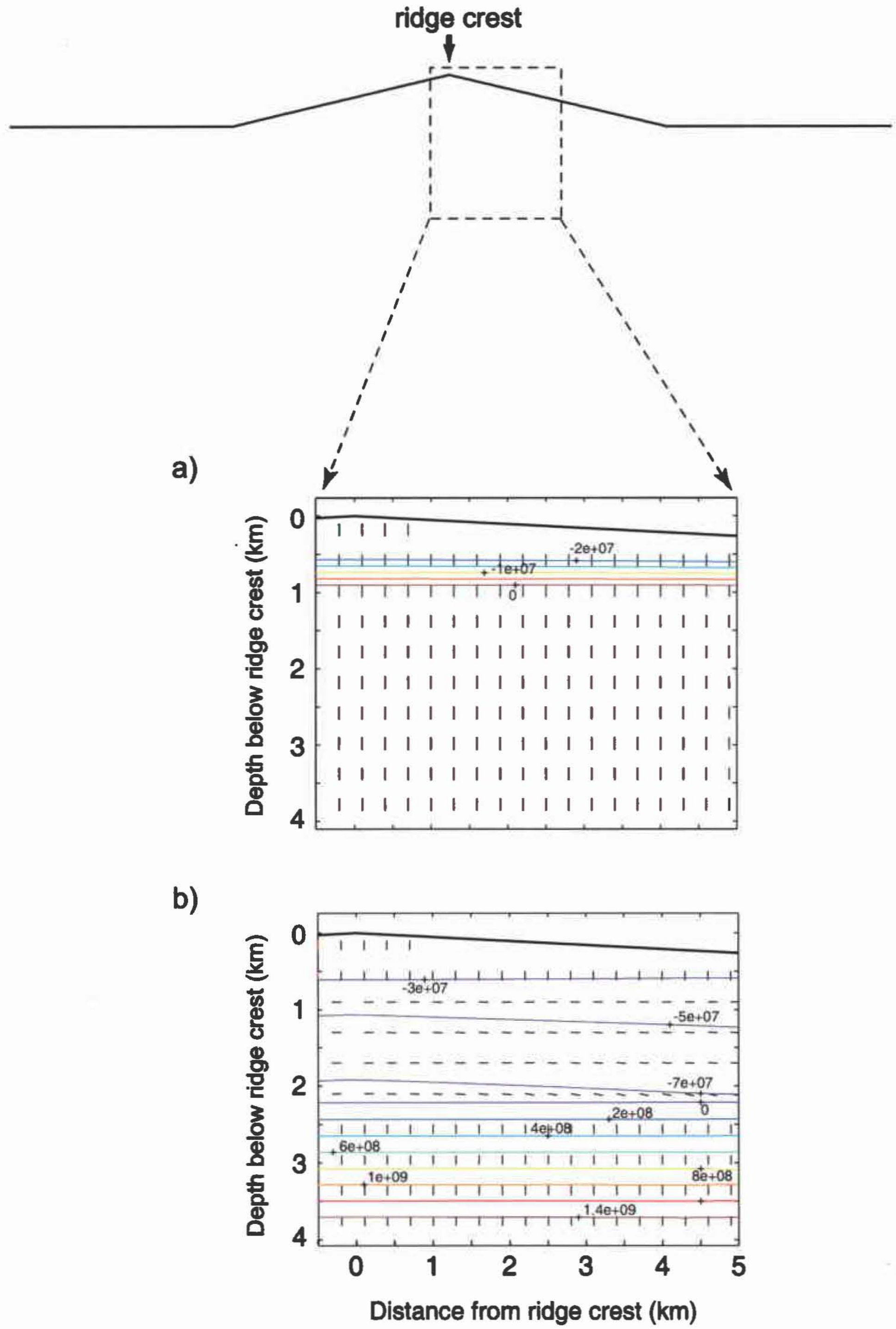
ridge crest
a)
Depth below ridge crest (km)
0
1
2
3
4
-2e+07
-1e+07
0
b)
Depth below ridge crest (km)
0
1
2
3
4
-3e+07
-5e+07
-7e+07
0
2e+08
4e+08
6e+08
1e+09
8e+08
1.4e+09
0
1
2
3
4
5
Distance from ridge crest (km)

Figure 18

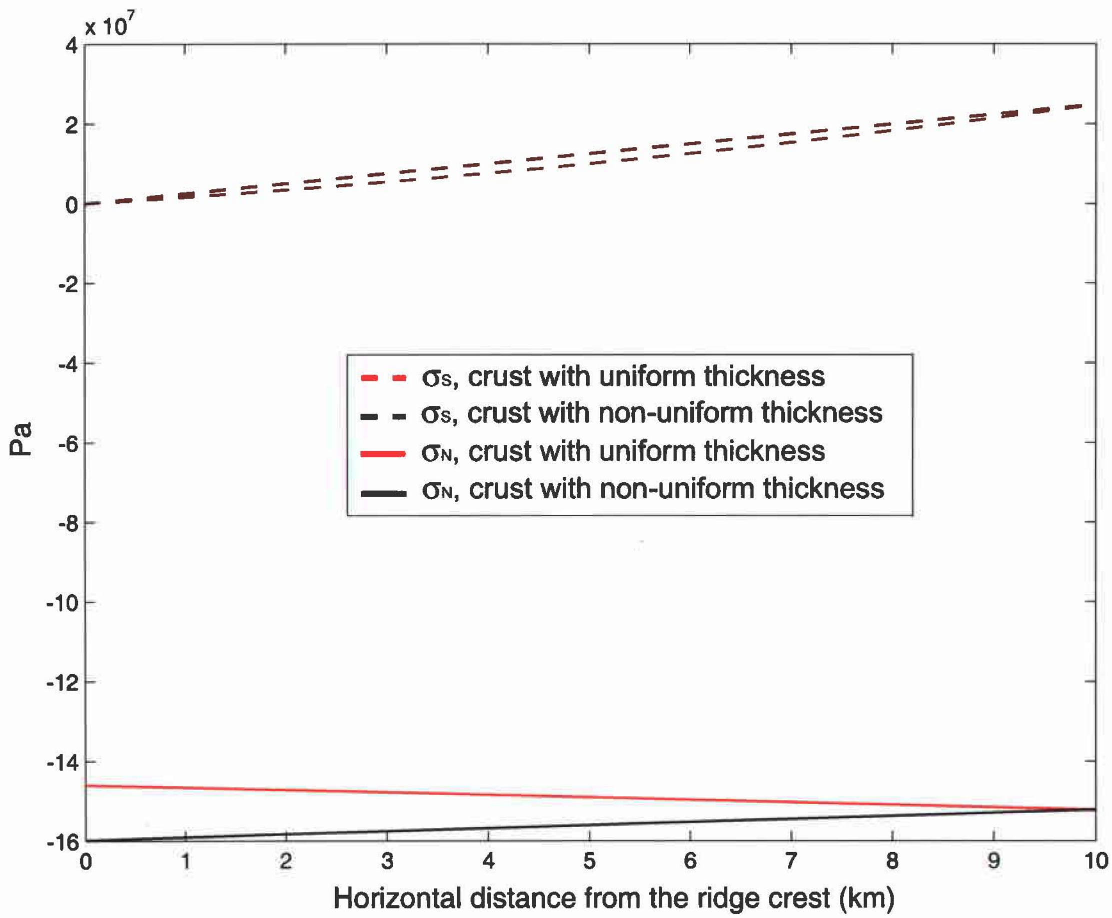
x 10^7
4
2
0
-2
-4
-6
-8
-10
-12
-14
-16
Pa
0
1
2
3
4
5
6
7
8
9
10
Horizontal distance from the ridge crest (km)
σS, crust with uniform thickness
σS, crust with non-uniform thickness
σN, crust with uniform thickness
σN, crust with non-uniform thickness

Figure 19

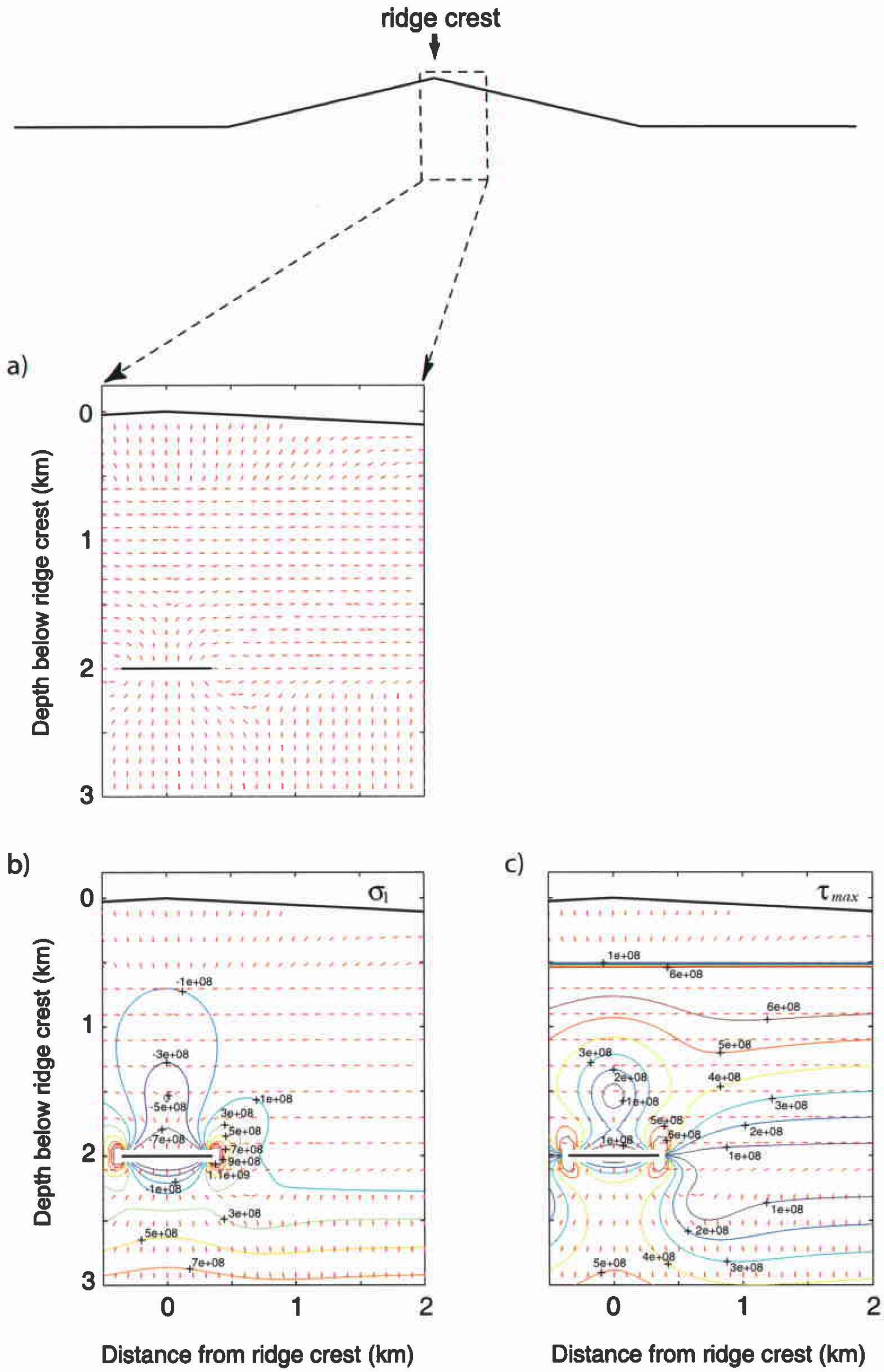
ridge crest
a)
b)
c)
Depth below ridge crest (km)
Distance from ridge crest (km)
σ1
τmax

Figure 20

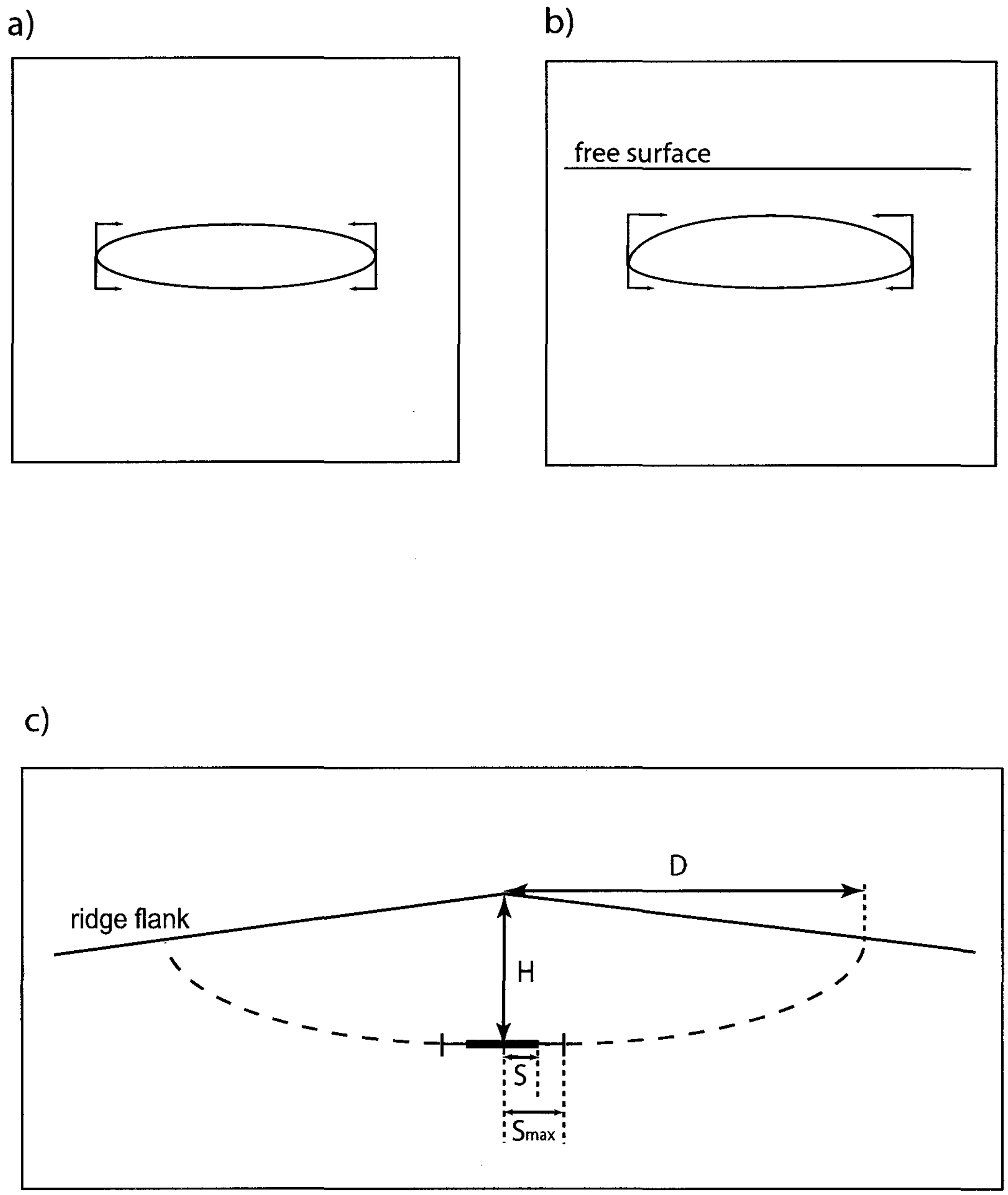

Figure 21

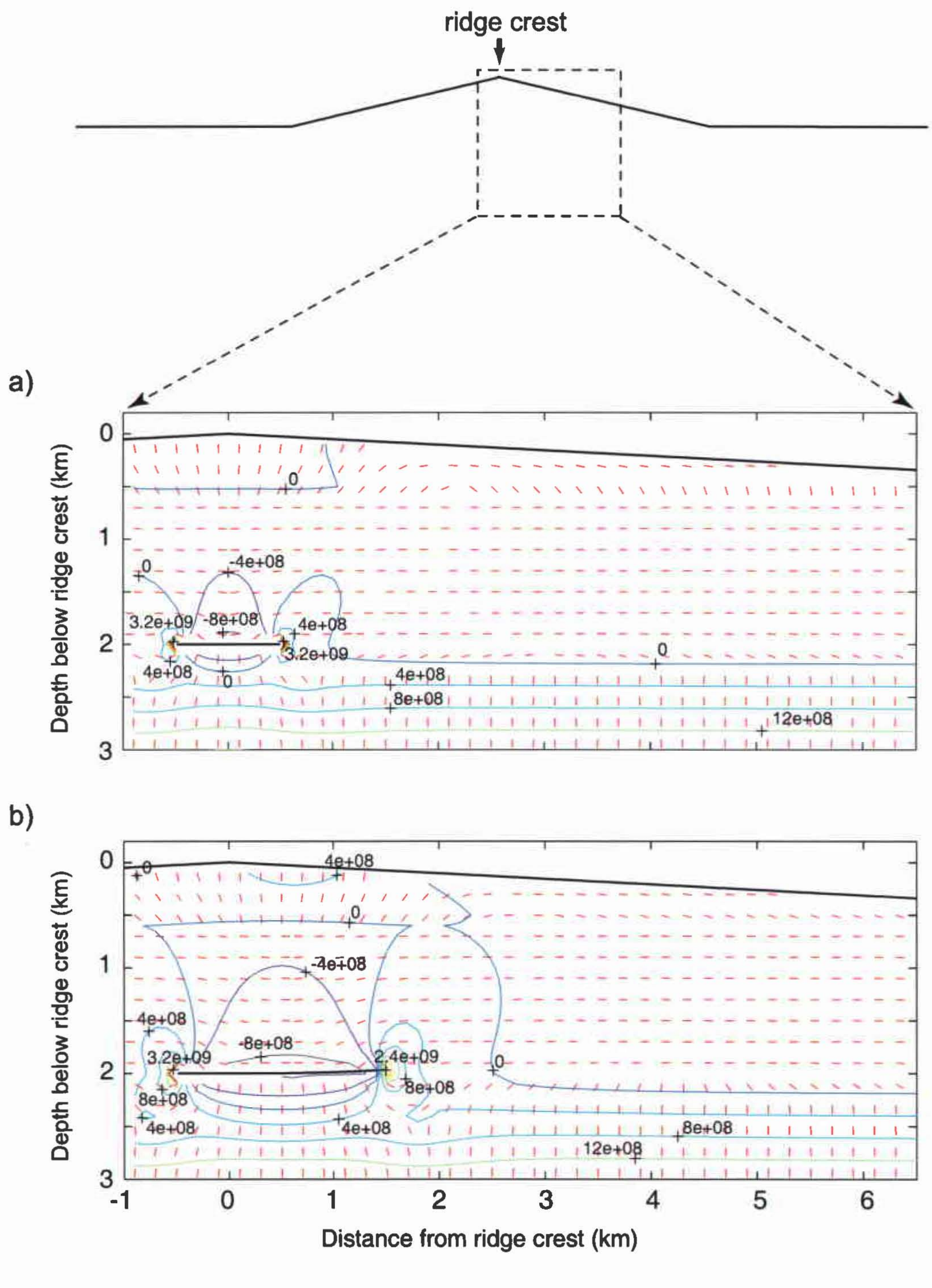

ridge crest
a)
b)
Depth below ridge crest (km)
Distance from ridge crest (km)
-4e+08
-8e+08
3.2e+09
4e+08
8e+08
12e+08
2.4e+09
0

Figure 22

c)

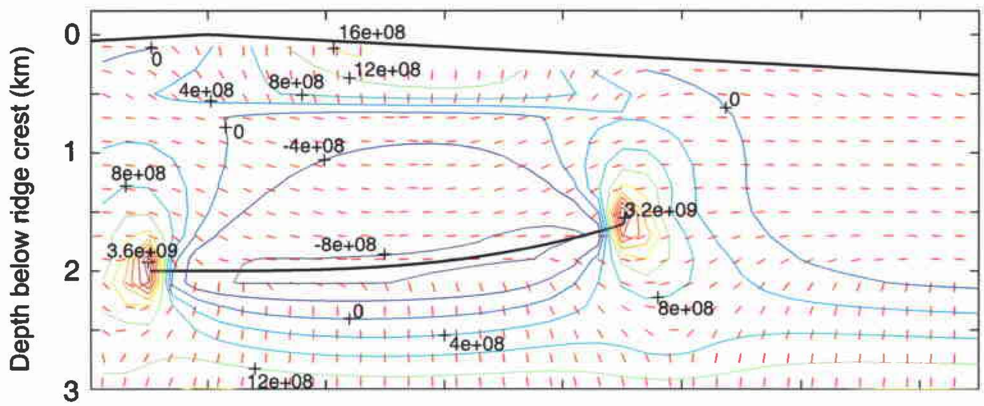
Depth below ridge crest (km)
0
1
2
3
16e+08
12e+08
8e+08
4e+08
0
-4e+08
8e+08
3.2e+09
3.6e+09
-8e+08
8e+08
0
4e+08
12e+08

d)

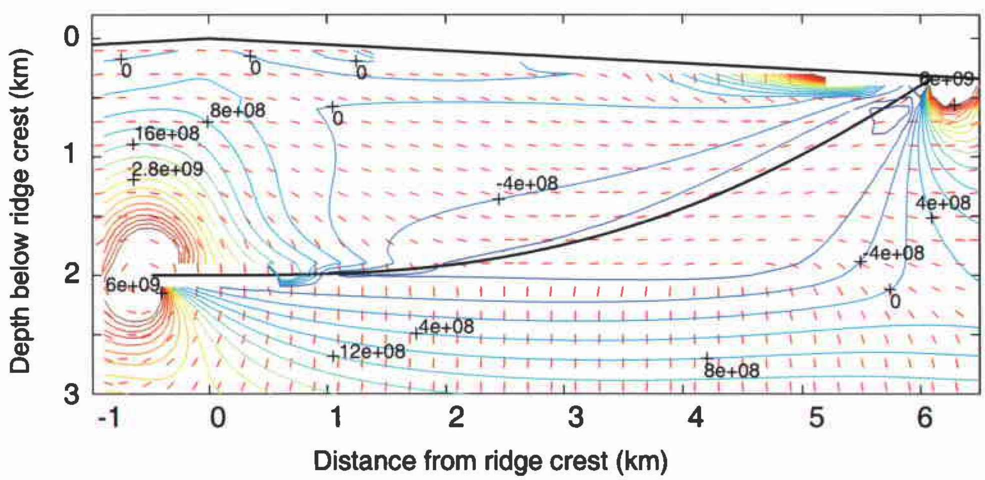
Depth below ridge crest (km)
0
1
2
3
0
8e+08
16e+08
2.8e+09
-4e+08
4e+08
-4e+08
6e+09
4e+08
12e+08
8e+08
-1
0
1
2
3
4
5
6
Distance from ridge crest (km)

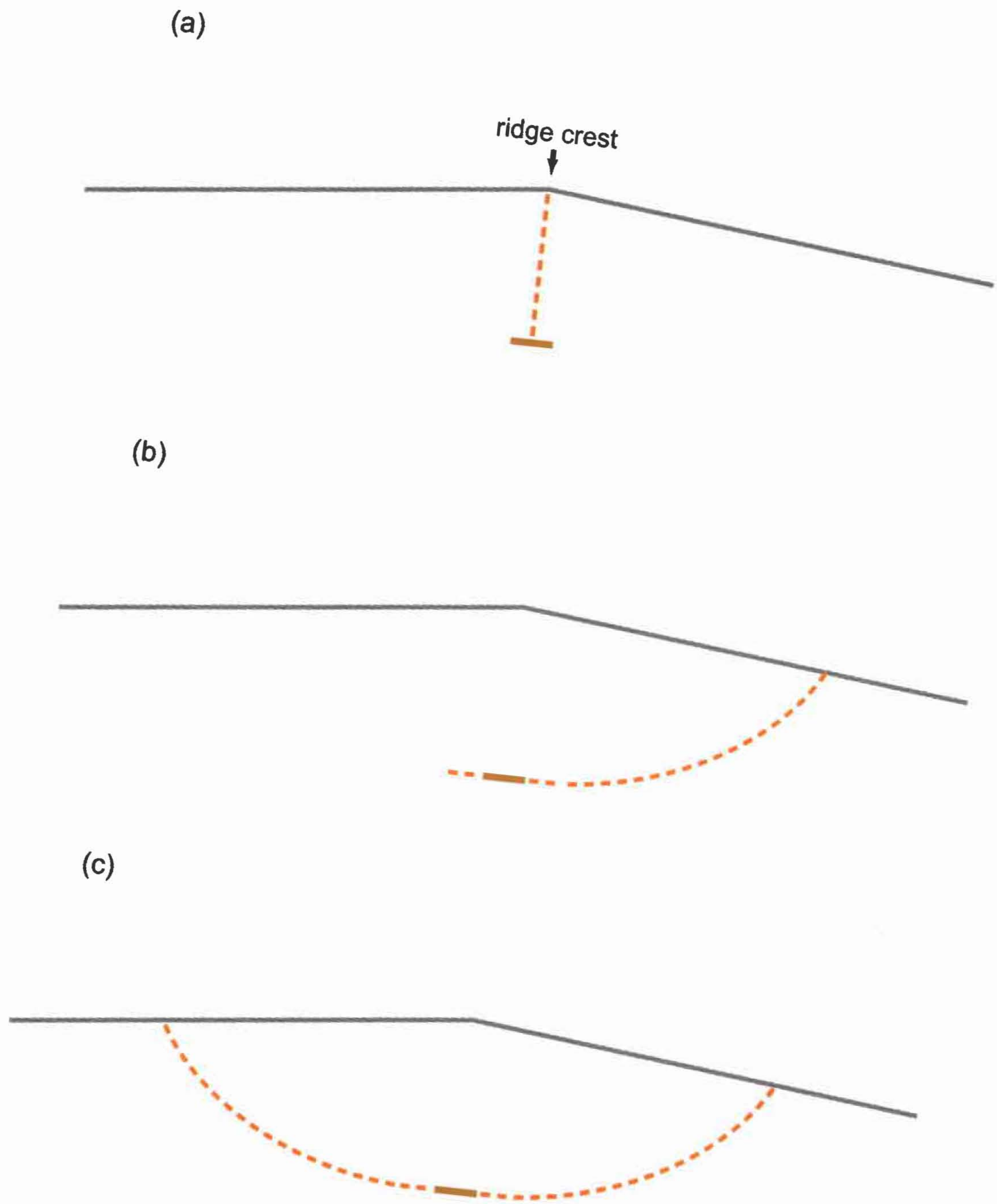

Figure 23

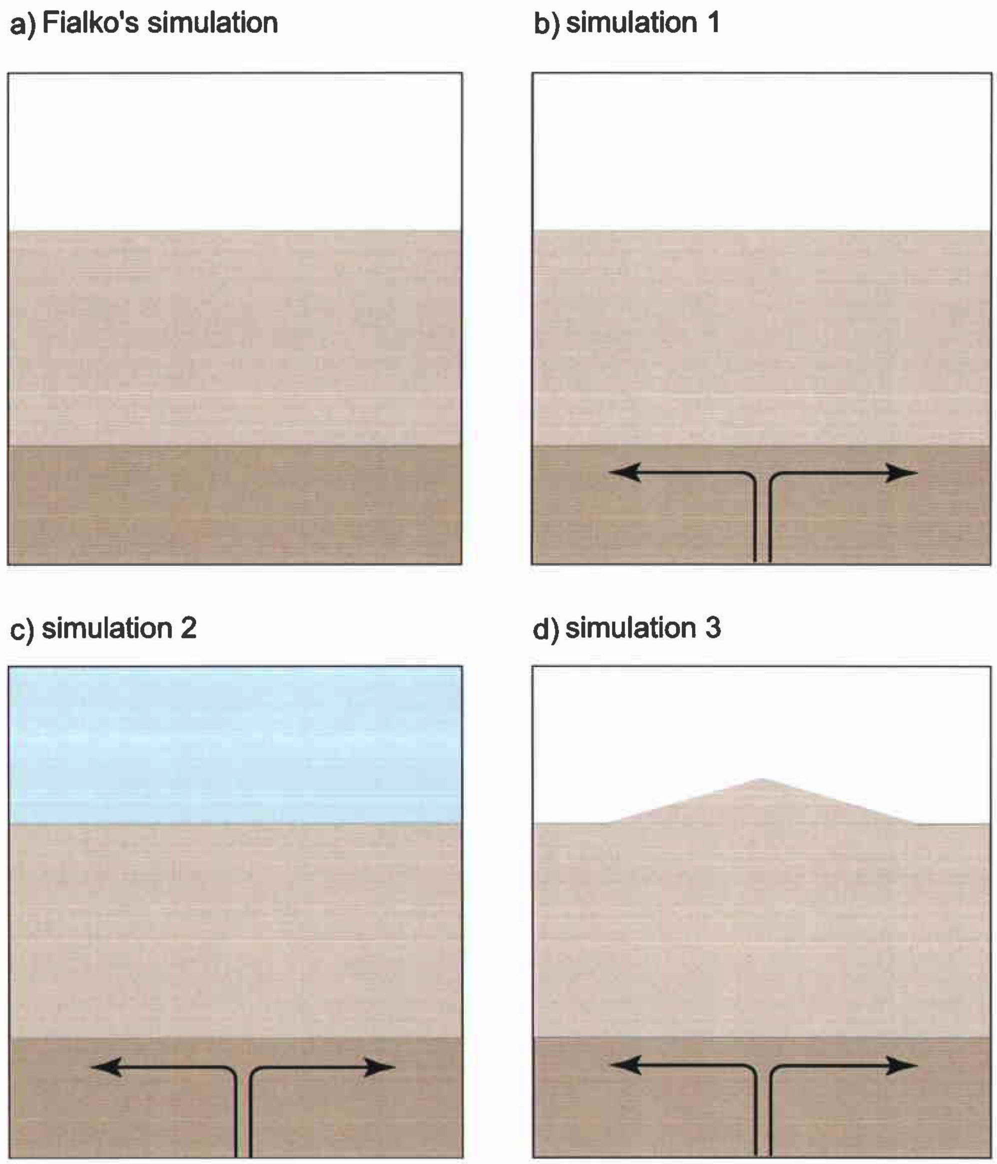
a) Fialko's simulation
b) simulation 1
c) simulation 2
d) simulation 3

Figure 24

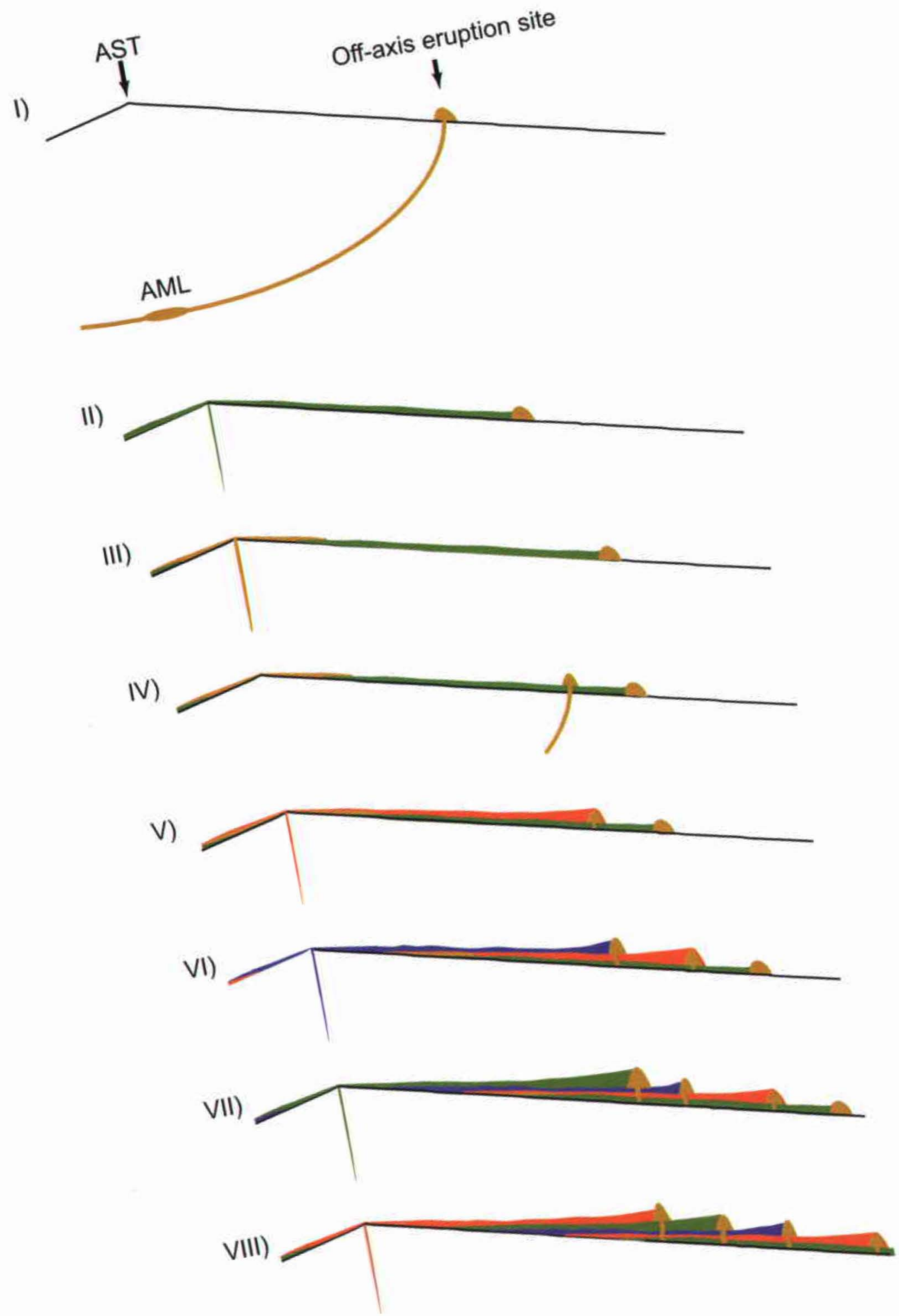

Figure 25

APPENDIX C: Plates

Plate Captions

Plate 1:

(a) DSL-120A sidescan data at a spatial resolution of 2 m per pixel for the survey area.

(b) Interpretative map of the DSL-120A sidescan data overlaid on top of SeaBeam bathymetry [*Cochran et al.*, 1999] contoured at 10 m intervals. R1-R4 show the divisions used in Chapter 3. The 3^{rd}-order segments are labeled as S (segment) and OSC (over spreading center) based on the definitions by Macdonald et al. [1998] and White et al. [2002]. Colored line segments on the left of the map shows termination types of the lobate-dominated regions identified on the Pacific plate. Green, blue, red, and gray represent lobate flows, faults, pillow mounds, and not determined areas, respectively.

APPENDIX D: Codes

Code Captions

Code 1:

Body forces and Hafner's basal tractions

Code 2:

Inserting a pressurized sill

Code 3:

Propagating a sill

Code 4:

TWODD

Code 5:

Base data

Code 6:

Other functions

```
% Code 1
% ambient_stress field 1
% gravitationally-induced stresses, no Hafner's basal tractions.
% Unit in Pa
% The total stress field is created by adding the ambient stress fields
% unit in meters

load base_data
% running twodd
[C,B,Ds,Dn,UxN,UyN,UsN,UnN,UsP,UnP,SIGxx,SIGyy,SIGxy,Ux,Uy,Sxx,Syy,Sxy,S1,S2,tau,mean,theta] =
twodd_func_T('f_6b',e_dat,b_dat,X,Y,rhow,rhob,y0,alpha,dm,m,g,c,AH,BH,L);


%%%%%%%%%%%%%%%%%%%%%%%%%%%%%%%%%%%%%%%%%%%%%%%%%%%%%%%%%%%%
% ambient_stress field 2
% gravitationally-induced stresses plus Hafner's basal tractions.
% Unit in Pa
% The total stress field is created by adding the ambient stress fields
% unit in meters

load base_data
% running twodd
[C,B,Ds,Dn,UxN,UyN,UsN,UnN,UsP,UnP,SIGxx,SIGyy,SIGxy,Ux,Uy,Sxx,Syy,Sxy,S1,S2,tau,mean,theta] =
twodd_func_T('f_6',e_dat,b_dat,X,Y,rhow,rhob,y0,alpha,dm,m,g,c,AH,BH,L);
```

```
% Code 2
% Inserting a pressurized sill into the ambient stress fields
% Unit in Pa
% The total stress field is created by adding the ambient stress fields
% (topography, gravity, Hafner's basal tractions) and
% the perturbation stress field (sill in the same geometry that is
% with the same Topo w/ no shear and normal stress)
% f_6 w/ gravity but no topographpy

% unit in meters

load base_data
%AMBIENT STRESS FIELD
% 1st TWODD run for ambient field (body forces and Hafner's basal traction)
[C,B,Ds,Dn,UxN,UyN,UsN,UnN,UsP,UnP,SIGxx,SIGyy,SIGxy,Ux,Uy,Sxx,Syy,Sxy,S1,S2,tau,mean,theta] =
twodd_func_T('f_6',e_dat,b_dat,X,Y,rhow,rhob,y0,alpha,dm,m,g,c,AH,BH,L);

% save the results as _amb
Camb = C;
Bamb = B;
Ds_amb = Ds;
Dn_amb = Dn;
UxNamb = UxN;
UyNamb = UyN;
UsNamb = UsN;
UnNamb = UnN;
UsPamb = UsP;
UnPamb = UnP;
SIGxxamb = SIGxx;
SIGxyamb = SIGxy;
SIGyyamb = SIGyy;
Uxamb = Ux;
Uyamb = Uy;
Sxxamb = Sxx;
Sxyamb = Sxy;
Syyamb = Syy;
S1_amb = S1;
S2_amb = S2;
tau_amb = tau;
mean_amb = mean;
theta_amb = theta;
X_amb = X;
Y_amb = Y;
b_dat_amb = b_dat;

%%%%%%%%%%%%%%%%%%%%%%%%%%%%%%%%
% PERTURBATION STRESS FIELD
% make observation points along the sill for 1st run of twodd_func_T to have Syy
% for M_sill

ds = 10;            % size of sill boundary element
n = 25;             % the number of elements
ys = 2.0*1000;      % depth of the sill (m) from the ridge summit
Umax_sill = -10;    % Max displacement at the center of the sill to either sides of the sill(km)
[M_sill] = make_b_dat_sill_const_f6(ds,n,ys,y0,L,e_dat,Umax_sill)

% ridge boundary element w/ Normal stress as 0
[M] = make_b_datR_WP_f6_7b_2(a,dm,dp1,dp2,S,rhow,g,m,p1,p2,y0,L);
M(:,6) = 0;

% eliminating observation points which overlap with sill boundary element
```

```
[X,Y] = eliminate_obs_point_f6_7b_2_sill(X,Y,ys,y0,M_sill,n)

% combine M and M_sill to make a new b_dat
clear b_dat
b_dat = [M;M_sill];

% For the 2nd run of twodd_func_T with the sill
% running twodd with f_6c that gives 0 for Pyy, Pxx, Pxy
[C,B,Ds,Dn,UxN,UyN,UsN,UnN,UsP,UnP,SIGxx,SIGyy,SIGxy,Ux,Uy,Sxx,Syy,Sxy,S1,S2,tau,mean,theta] =
twodd_func_T('f_6c',e_dat,b_dat,X,Y,rhow,rhob,y0,alpha,dm,m,g,c,AH,BH,L);

% save the results as _pbt
Cpbt = C;
Bpbt = B;
Ds_pbt = Ds;
Dn_pbt = Dn;
UxNpbt = UxN;
UyNpbt = UyN;
UsNpbt = UsN;
UnNpbt = UnN;
UsPpbt = UsP;
UnPpbt = UnP;
SIGxxpbt = SIGxx;
SIGxypbt = SIGxy;
SIGyypbt = SIGyy;
Uxpbt = Ux;
Uypbt = Uy;
Sxxpbt = Sxx;
Sxypbt = Sxy;
Syypbt = Syy;
S1_pbt = S1;
S2_pbt = S2;
tau_pbt = tau;
mean_pbt = mean;
theta_pbt = theta;
X_pbt = X;
Y_pbt = Y;
b_dat_pbt = b_dat;

% TOTAL STRESS FIELD
Ux = [Uxpbt + Uxamb];
Uy = [Uypbt + Uyamb];
SxxT = [Sxxpbt + Sxxamb];
SxyT = [Sxypbt + Sxyamb];
SyyT = [Syypbt + Syyamb];
S1 = sig1(SxxT,SyyT,SxyT);
S2 = sig2(SxxT,SyyT,SxyT);
tau = taumax(SxxT,SyyT,SxyT);
mean = ave(SxxT,SyyT,SxyT);
theta = angp(SxxT,SyyT,SxyT);
```

```
% Code 3
% Sill_propagation
% Unit in Pa
% Unit in meters

load base_data
Sill_addition

%%%%%%%%%%%%%%%%%%%%%%%%%%%%%%%%%
% calculating Sp in a polar coordinate.
% Sp = S_theta_theta = a_theta_x*a_theta_x*Sxx + a_theta_x*a_theta_y*Sxy +
% a_theta_y*a_theta_x*Syx + a_theta_y*a_theta_y*Syy
% a_theta_x = cos(thata_thata_x) = cos(pi/2-theta) = -sin(theta)
% a_theta_y = cos(thata_thata_y) = cos(theta)
% theta = beta and Sxy = Syx
% therefore, Sp = sin(theta)*sin(theta)*Sxx + 2*(-sin(theta))*cos(theta)*Sxy +
% cos(beta)*cos(beta)*Syy
% Here theta = beta
% beta = -pi/180;                    % resolution of observation points, 1 degree

Sp = zeros(1,90);

num = 0;
j = 1;
while num < 90
   Sp(1,j) = sin(beta*num)*sin(beta*num)*SxxT(1,j) + 2*(-sin(beta*num))*cos(beta*num)*SxyT(1,j) +
cos(beta*num)*cos(beta*num)*SyyT(1,j);
   num = num + 1;
   j = j + 1;
end

% For the 3nd run of twodd_func_T with the sill with a tail

% make b_dat for sill using Syy from the 1st run of twodd_func_T
% k = 10^(-4);                      % k*SyyS is excess stress from the ambient stress.
% [M_sill] = make_b_dat_sill_f6(ds,n,ys,y0,L,W,k,SyyS);

% constant Normal pressure on a sill regardless of AH and BH.
max_Sp = max(Sp)
[i,j] = find(Sp == max_Sp)
Xp = X(i,j)
Yp = Y(i,j)
time = 1;
Sill_Growth = [time j max_Sp (Xp-W)/1000 Yp];

if (Xp-W) > dm*m*cos(a/180*pi)          % Xp is on the ridge flat base
   ymin = y0 + dm*m*sin(a/180*pi);              % ymin is the depth to the ridge flat
                                  base
else                                    % Xp is on the ridge flank
   ymin = y0 + (Xp-W)*tan(a/180*pi);    % ymin is the depth to the ridge flank
                                  at X= Xp
end

while Yp > ymin                                     % while Yp is below the ridge surface
   M_tail = zeros(1,6);
   M_tail(1,1) = xSillTip;
   M_tail(1,2) = ySillTip;
   M_tail(1,3) = Xp;
   M_tail(1,4) = Yp;
   M_tail(1,5) = 0;
   E = e_dat(2);                                    %  E = Young's modulus;
```

```
PR = e_dat(1);                              % PR = Poisson's ratio;
myu = E/(2*(1+PR)); % shear modulus,10^10Pa
h = ys + y0 - Yp;
M_tail(1,6) = (Umax_sill*myu)/(ds*n*(1-PR)) + rhob*g*h ;

[M_sill] = [M_sill;M_tail];

% topo w/ Normal stress as 0
clear M;
[M] = make_b_datR_WP_f6_7b_2(a,dm,dp1,dp2,S,rhow,g,m,p1,p2,y0,L);
M(:,6) = 0;

% combine M and M_sill to make a new b_dat
clear b_dat
b_dat = [M;M_sill];

% making observation points in a circle around the sill tip(s)
xSillTip = Xp;
ySillTip = Yp;

beta = -pi/180; % resolution of obs points, 1 degree
[X] = zeros(1,90);
[Y] = zeros(1,90);

num = 0;
j = 1;
while num < 90
  X(1,j) = [xSillTip + ds*cos(beta*num)];
  Y(1,j) = [ySillTip + ds*sin(beta*num)];
  num = num + 1;
  j = j + 1;
end

% running twodd with f_6b that gives 0 for Pyy, Pxx, Pxy
[C,B,Ds,Dn,UxN,UyN,UsN,UnN,UsP,UnP,SIGxx,SIGyy,SIGxy,Ux,Uy,Sxx,Syy,Sxy,S1,S2,tau,mean,theta]
= twodd_func_T('f_6b',e_dat,b_dat,X,Y,rhow,rhob,y0,alpha,dm,m,g,c,AH,BH,L);

% save the results as _pbt
Cpbt = C;
Bpbt = B;
Ds_pbt = Ds;
Dn_pbt = Dn;
UxNpbt = UxN;
UyNpbt = UyN;
UsNpbt = UsN;
UnNpbt = UnN;
UsPpbt = UsP;
UnPpbt = UnP;
SIGxxpbt = SIGxx;
SIGxypbt = SIGxy;
SIGyypbt = SIGyy;
Uxpbt = Ux;
Uypbt = Uy;
Sxxpbt = Sxx;
Sxypbt = Sxy;
Syypbt = Syy;
S1_pbt = S1;
S2_pbt = S2;
tau_pbt = tau;
mean_pbt = mean;
theta_pbt = theta;
```

```
  X_pbt = X;
  Y_pbt = Y;
  b_dat_pbt = b_dat;

  % TOTAL STRESS FIELD
  Ux = [Uxpbt + Uxamb];
  Uy = [Uypbt + Uyamb];
  SxxT = [Sxxpbt + Sxxamb];
  SxyT = [Sxypbt + Sxyamb];
  SyyT = [Syypbt + Syyamb];
  S1 = sig1(SxxT,SyyT,SxyT);
  S2 = sig2(SxxT,SyyT,SxyT);
  tau = taumax(SxxT,SyyT,SxyT);
  mean = ave(SxxT,SyyT,SxyT);
  theta = angp(SxxT,SyyT,SxyT);

  % calculating Sp in a polar coordinate.
  Sp = zeros(1,90);

  num = 0;
  j = 1;
  while num < 90
    Sp(1,j) = sin(beta*num)*sin(beta*num)*SxxT(1,j) + 2*(-sin(beta*num))*cos(beta*num)*SxyT(1,j) +
cos(beta*num)*cos(beta*num)*SyyT(1,j);
    num = num + 1;
    j = j + 1;
  end

  max_Sp = max(Sp)
  [i,j] = find(Sp == max_Sp)
  Xp = X(i,j);
  Dis_erup = (Xp - W)/1000       %Distance to the extended sill tip from the
                     ridge crest in km
  Yp = Y(i,j)

  time = time + 1
  SG = [time j max_Sp (Xp-W)/1000 Yp];
  Sill_Growth = [Sill_Growth;SG];

  if (Xp-W) > dm*m*cos(a/180*pi)          % Xp is on the ridge flat base
    ymin = y0 + dm*m*sin(a/180*pi);       % ymin is the depth of ridge
                             flat base
  else                        % Xp is on the ridge flank
    ymin = y0 + (Xp-W)*tan(a/180*pi);     % ymin is the depth to the ridge
                             flank at X= Xp
  end
end
```

```
%Code 4
function [C,B,Ds,Dn,UxN,UyN,UsN,UnN,UsP,UnP,SIGxx,SIGyy,SIGxy,...
Ux,Uy,Sxx,Syy,Sxy,S1,S2,tau,mean,theta] =
twodd_func_T(F,e_dat,b_dat,X,Y,rhow,rhob,y0,alpha,dm,m,g,c,AH,BH,L)

%function [C,B,Ds,Dn,UxN,UyN,UsN,UnN,UsP,UnP,SIGxx,SIGyy,SIGxy,...
%Ux,Uy,Sxx,Syy,Sxy,S1,S2,tau,mean,theta] =
twodd_func_T(F,e_dat,b_dat,X,Y,rhow,rhob,y0,alpha,dm,m,g,c,AH,BH,L)
% Function version of Two-dimensional boundary element program
% All the functions twodd_func calls are internally stored subfunctions
% with stress boundary conditions for Matlab 4.1
% This program is modified from Appendix B of the book
% "Boundary element methods in Solid Mechanics"
% by S.L. Crouch and A.M. Starfield, 1983
% Last revised on 6/29/03. By Stephen J. Martel.

% This code has been further modified from twodd_func.m to have variable ambient stress field
% Modified sections have been noted.
% Last revised on 8/8/03. By Tomoko Kurokawa.

% Input F is added and r_dat is removed in this twodd_func_T.m

% Read elastic constants, remote stress field data, and boundary data from
% data files elastic.dat, remote.dat, and boundary.dat, respectively

% Elastic constants. PR and E should be in one row;
        PR = e_dat(1);                  % PR = Poisson's ratio;
        E = e_dat(2);                   % E = Young's modulus;

% % Ambient field. PXX, PYY, PXY should be in one row;(Commented for this
% twodd_func_T.m
%       Pxx = r_dat(1);                 % Remote stress sigma xx;
%       Pyy = r_dat(2);                 % Remote stress sigma yy;
%       Pxy = r_dat(3);                 % Remote stress sigma xy;

% Boundary element geometry and boundary conditions
% Data in each row of this file pertains to one element
% Now separate out data types by column to form column vectors
        XBEG = b_dat(:,1);              % element endpoint coordinate
        YBEG = b_dat(:,2);              % element endpoint coordinate
        XEND = b_dat(:,3);              % element endpoint coordinate
        YEND = b_dat(:,4);              % element endpoint coordinate
        BVs = b_dat(:,5); % Shear traction boundary condition
        BVn = b_dat(:,6); % Normal traction boundary condition

        NUM = length(BVs);                              % NUM = number of elements

% Define new elastic constants to be used internally
        CON = 1/(4*pi*(1-PR));
        CONS = E/(1+PR);
        PR1 = 1-2*PR;
        PR2 = 2*(1-PR);

% Define locations, lengths, orientations, and boundary conditions for boundary elements
% This information is stored here as column vectors of size (NUMx1)
        x = (XBEG + XEND)/2;                            % element midpoints
        y = (YBEG + YEND)/2;                            % element midpoints
        XE = x;
        YE = y;
        XD = XEND-XBEG;
        YD = YEND-YBEG;
```

```
        A = sqrt(XD.*XD +YD.*YD)/2;                  % half-length of element
% In the lines below, B = beta = orientation of element relative to global x-axis
        SINB = YD./(2*A);                            % sine beta
        COSB = XD./(2*A);                            % cosine beta
        SIN2B = 2*SINB.*COSB;                        % sine 2*beta
        COS2B = COSB.*COSB-SINB.*SINB;               % cosine 2*beta
        SINB2 = SINB.*SINB;                          % sine squared of beta
        COSB2 = COSB.*COSB;                          % cosine squared of beta

%       Find the stresses at the element midpoints (ADDED for this
%       twodd_func_T.m version
        [Pxx,Pyy,Pxy] = feval(F,x,y,rhow,rhob,y0,alpha,dm,m,g,c,AH,BH,L);

% Adjust stress boundary conditions to account for remote stresses.
% First resolve components of the remote stress onto the plane of each element...
        SIGs = (Pyy-Pxx).*SIN2B/2 + Pxy.*COS2B;
        SIGn = Pxx.*SINB2 - Pxy.*SIN2B + Pyy.*COSB2;
% and then subtract the resolved remote stress from the boundary stresses.
        BVs = BVs - SIGs;
        BVn = BVn - SIGn;
% The remote stress will be added back at the end of the solution.

% Compute influence coefficients between boundary elements.
% C(i,j) = effect at obs pt i due to a load at element j.
% The organization of the coefficients here is slightly different
% from Crouch & Starfield
%       First dimension the vectors storing the influence coefficients
        nobs=NUM*NUM;
        [Uxsv,Uysv,Uxnv,Uynv,Sxxsv,Syysv,Sxysv,Sxxnv,Syynv,Sxynv] = set1_func(nobs);

        for i=1:NUM
                first = (i-1)*NUM+1;
                last = i*NUM;
                xe = XE(i);
                ye = YE(i);
                COSBe = COSB(i);
                SINBe = SINB(i);
                a = A(i);
                Sd = 1;
                Nd = 1;
                [Uxs,Uys,Uxn,Uyn,Sxxs,Syys,Sxys,Sxxn,Syyn,Sxyn] = ...
                coeff_func(x,y,xe,ye,a,COSBe,SINBe,CON,CONS,PR1,PR2,Sd,Nd);
                % Append sequentially produced vectors to master column vectors
                [Uxsv,Uysv,Uxnv,Uynv,Sxxsv,Syysv,Sxysv,Sxxnv,Syynv,Sxynv] = ...
                append1_func(first,last,Uxs,Uys,Uxn,Uyn,Sxxs,Syys,Sxys,Sxxn,Syyn,Sxyn,...
                Uxsv,Uysv,Uxnv,Uynv,Sxxsv,Syysv,Sxysv,Sxxnv,Syynv,Sxynv);
        end

% Calculate trig functions
% and direction cosine matrices for stress transformations
        [SINNB,COSSB,SINN2B,COSS2B,SINNB2,COSSB2] = ...
        dircos1_func(SINB,COSB,SIN2B,COS2B,SINB2,COSB2,NUM);

% Reshape column vectors into square matrices, then clear column vectors
        dimx = NUM;
        dimy = NUM;
        [Uxs,Uxn,Uys,Uyn,Sxxs,Sxxn,Syys,Syyn,Sxys,Sxyn] = ...
        square1_func(Uxsv,Uxnv,Uysv,Uynv,Sxxsv,Sxxnv,Syysv,Syynv,Sxysv,Sxynv,dimx,dimy);

% Convert xy stresses returned from coeff to normal and shear tractions on elements
        Cisjs = (Syys-Sxxs).*(SINN2B)/2 + Sxys.*COSS2B;
```

```
        Cisjn = (Syyn-Sxxn).*(SINN2B)/2 + Sxyn.*COSS2B;
        Cinjs = Sxxs.*SINNB2 - Sxys.*SINN2B + Syys.*COSSB2;
        Cinjn = Sxxn.*SINNB2 - Sxyn.*SINN2B + Syyn.*COSSB2;

% Solve system of algebraic equations to get the displacement discontinuities
% First regroup the influence coefficient and boundary condition submatrices as shown:
% | [Cisjs]      [Cisjn]   |          | [Ds]   |          =        | [Bs]    |
% | [Cinjs]      [Cinjn] | | [Dn]    |                  | [Bn]    |
        C = [Cisjs, Cisjn; Cinjs, Cinjn];                              % C = influence coefficients;
%       clear Cisjs Cisjn Cinjs Cinjn;
        B = [BVs; BVn];                                                % B= Stress boundary conditions;
% Solve the matrix system [C][D]=[B] to get the displacement discontinuity vector D
        D= C\B;
% Separate the D vector into subvectors Ds and Dn
        Ds = D(1:NUM);                          % Ds elements are in upper half of D
        Dn = D(NUM+1:2*NUM);                    % Dn elements are in lower half of D
%       clear B C D

% Compute displacements and stresses on boundary elements
% The stresses obtained should match the boundary conditions

% First find the stresses and displacements, in an x-y reference frame, by superposition
        UxN = Uxs*Ds + Uxn*Dn;                  % x-displacement on negative side of i;
        UyN = Uys*Ds + Uyn*Dn;                  % y-displacement on negative side of i;
        SIGxx = Pxx + Sxxs*Ds + Sxxn*Dn; % Note that remote stress is added back in;
        SIGyy = Pyy + Syys*Ds + Syyn*Dn; % Note that remote stress is added back in;
        SIGxy = Pxy + Sxys*Ds + Sxyn*Dn; % Note that remote stress is added back in;

% Now resolve DISPLACEMENTS in the xy frame into shear and normal components
% Start by solving for displacements on the NEGATIVE (N) sides of the elements...;
        UsN = UxN.*COSB + UyN.*SINB;
        UnN = -UxN.*SINB + UyN.*COSB;

% and then add the displacement discontinuity at each element to get
% the displacement components on the positive (P) sides of the elements
        UsP = UsN - Ds;
        UnP = UnN - Dn;

% The last step is to resolve the xy STRESSES to normal and shear stresses on the elements.
        SIGs = (SIGyy-SIGxx).*(SIN2B/2)  +  SIGxy.*COS2B;
        SIGn = SIGxx.*SINB2  -  SIGxy.*SIN2B  +  SIGyy.*COSB2;

% COMPUTATION OF DISPLACEMENTS AND STRESSES AT SPECIFIED OBSERVATION POINTS I IN
BODY
% Proceed if output on observation grid X,Y is desired, otherwise end
if nargout > 13
        [dimx,dimy] = size(X);
        NUM2 = dimx*dimy;

%       Determine the ambient field at the grid points (Added for this
%       twodd_func_T.m
  [Pxx,Pyy,Pxy] = feval(F,X,Y,rhow,rhob,y0,alpha,dm,m,g,c,AH,BH,L);

% Calculate influence coefficients at gridpoints
        x = X(:);                   % Grid nodes in column vector form
        y = Y(:);                   % Grid nodes in column vector form
%       First dimension the vectors storing the influence coefficients
        nobs=NUM2*NUM;
        [Uxsv,Uysv,Uxnv,Uynv,Sxxsv,Syysv,Sxysv,Sxxnv,Syynv,Sxynv] = set1_func(nobs);
% Now loop through grid element by element
% The end result will be ten column vectors each having NUM2*NUM rows
```

```
        for i=1:NUM
                first = (i-1)*NUM2+1;
                last = i*NUM2;
                xe = XE(i);
                ye = YE(i);
                COSBe = COSB(i);
                SINBe = SINB(i);
                a = A(i);
                Sd = Ds(i);
                Nd = Dn(i);
                [Uxs,Uys,Uxn,Uyn,Sxxs,Syys,Sxys,Sxxn,Syyn,Sxyn] = ...
                coeff_func(x,y,xe,ye,a,COSBe,SINBe,CON,CONS,PR1,PR2,Sd,Nd);
                % Append sequentially produced vectors to master column vectors
                [Uxsv,Uysv,Uxnv,Uynv,Sxxsv,Syysv,Sxysv,Sxxnv,Syynv,Sxynv] = ...
                append1_func(first,last,Uxs,Uys,Uxn,Uyn,Sxxs,Syys,Sxys,Sxxn,Syyn,Sxyn,...
                Uxsv,Uysv,Uxnv,Uynv,Sxxsv,Syysv,Sxysv,Sxxnv,Syynv,Sxynv);
        end

% Reshape column vectors into square matrices the size of the
% observation grid, and in the process sum the contributions
% from each element
        [Ux,Uy,Sxx,Syy,Sxy] = ...
square2_func(Uxsv,Uxnv,Uysv,Uynv,Sxxsv,Sxxnv,Syysv,Syynv,Sxysv,Sxynv,NUM2,NUM,dimx,dimy);

% Add back the remote field
        Sxx = Pxx + Sxx;
        Syy = Pyy + Syy;
        Sxy = Pxy + Sxy;


        S1 = sig1(Sxx,Syy,Sxy);
        S2 = sig2(Sxx,Syy,Sxy);
        tau = taumax(Sxx,Syy,Sxy);
        mean = ave(Sxx,Syy,Sxy);
        theta = angp(Sxx,Syy,Sxy);
end

%%%%%%%%%%%%%%%%%%%%%%%%%%%%%%%%%%%%%%%%%%%%%%%%%%%%%%%%%%%%%%%%%%%%%%%%%%%%%%%%%%%%%%%
% Alphabetical listing of local subfunctions called in the primary function twodd_func
%%%%%%%%%%%%%%%%%%%%%%%%%%%%%%%%%%%%%%%%%%%%%%%%%%%%%%%%%%%%%%%%%%%%%%%%%%%%%%%%%%%%%%%
function [Pxx,Pyy,Pxy] = f_6(x,y,rhow,rhob,y0,alpha,dm,m,g,c,AH,BH,L)
% function [Pxx,Pyy,Pxy] = ambient_field(x,y)
% Ridge topography (a slope of alpha degrees) with gravity and water
% pressure in addition to tectonic loads defined by W.Hafner
% (Bulletin of the Geological Society of America, vol.62, 1951, page 392).
% Calculates the ambient field given the x and y coordinates of a point
% The tectonic shear stress is zero at the ridge base.
% The positive y-axis points down.

% y0 = the depth from the seafloor to the ridge summit (m)
% y1 = the depth to the flat seafloor from the ridge summit (m)


A = (alpha/180)*pi;
W = L/4;

y1 = dm*m*sin(A);         % y1 = depth to the flat seafloor from the ridge summit (m)
```

```
Pwl_a = (abs(x-W)*tan(A)+y0)*rhow*g;  % Water pressure on the ridge slope but below y = 0 in the ridge
region, Positive value
Pwl_b = y*rhow*g;         % Water pressure above the ridge slope but below y = 0 in the ridge region,
Positive value
Prl = (y-y0-tan(A)*abs(x-W))*rhob*g; % Rocke pressure below the ridge slope in the ridge region, Positive
value
Pwll_a = (y0+y1)*rhow*g;        % Water pressure on the flat seafloor outside of the ridge region due to
water y < 0, Positive value
Pwll_b = y*rhow*g;
Prll = (y-y0-y1)*rhob*g;   % Rock pressure below the flat seafloor outside of the ridge, Positive value

% % % % % from W.Hafner 1951 page 392 % % % % %
beta = (2*pi/L);          % alpha in Hafner's paper
yh = y - y1 - y0;
xh = x;

k1 = ( AH*beta*c*cosh(beta*c) - BH*beta*c*sinh(beta*c) + AH*sinh(beta*c) ) / ( sinh(beta*c)^2-beta^2*c^2 );
k2 = ( AH*beta*c*sinh(beta*c) - BH*beta*c*cosh(beta*c) + BH*sinh(beta*c) ) / ( sinh(beta*c)^2-beta^2*c^2 );

f1 = sinh(beta*yh) + beta*yh.*cosh(beta*yh);   % yh is y in Hafner's paper
f2 = 2*cosh(beta*yh) + beta*yh.*sinh(beta*yh);
f3 = sinh(beta*yh) - beta*yh.*cosh(beta*yh);
f4 = (beta*yh).*sinh(beta*yh);

PxxH = sin(beta*xh).*(-k1*f1 + k2*f2);          % Sxx in Hafner's paper
PyyH = sin(beta*xh).*(-k1*f3 - k2*f4);          % Syy in Hafner's paper
PxyH = cos(beta*xh).*(k1*f4 - k2*f1);           % Sxy in Hafner's paper

% % % % % % %% % % %% % % %% % % %% % % %% % % %
sizeXY = size(x);

Pxx = NaN*ones(size(x));
Pyy = NaN*ones(size(x));
Pxy = NaN*ones(size(x));

limit_i = sizeXY(1) + 1;
limit_j = sizeXY(2) + 1;

i=1 ;
j=1 ;
while i< limit_i
  i;
  while j<limit_j
    j;
    if abs(x(i,j) - W) < dm*m*cos(A)           % Within the ridge area along the x-axis
      if y(i,j) > (abs(x(i,j)-W))*tan(A) + y0
        if y(i,j) < y0 + y1                    % Within the ridge triangle
          Pyy(i,j) = Pwl_a(i,j) + Prl(i,j);
          Pxx(i,j) = Pwl_a(i,j);
          Pxy(i,j) = 0;
        else                                   % In the crust
          Pyy(i,j) = Pwl_a(i,j) + Prl(i,j) + PyyH(i,j);
          Pxx(i,j) = PxxH(i,j);
          Pxy(i,j) = PxyH(i,j);
        end
      else                                     % In water
        Pyy(i,j) = Pwl_b(i,j);
        Pxx(i,j) = Pyy(i,j);
        Pxy(i,j) = 0;
      end
    else   % Otuside of the ridge area along the x-axis
```

```
        if y(i,j) > y0 + y1                          % In the crust
           Pyy(i,j) = PwII_a + PrII(i,j) + PyyH(i,j);
           Pxx(i,j) = PxxH(i,j);
           Pxy(i,j) = PxyH(i,j);
        else                                         % In water
           Pyy(i,j) = PwII_b(i,j);
           Pxx(i,j) = Pyy(i,j);
           Pxy(i,j) = 0;
        end
     end
     j=j+1;
   end
   i=i+1;
   j=1;
end

%%%%%%%%%%%%%%%%%%%%%%%%%%%%%%%%%%%%%%%%%%%%%%%%%%%%%%%%%%%%%%%%%%%%%%%%%%%%%%%%%%%%%%%%%%%%%%%%%%%%%%%%%%%%%%%%%%%%%%%%%%
%%%%%%%%%%%%%%%%%%%%%%%%%%%%%%%%%%%%%%%%%%%%%%%%%%%%%%%%%%%%%%%%
function [Pxx,Pyy,Pxy] = f_6b(x,y,rhow,rhob,y0,alpha,dm,m,g,c,AH,BH,L)
% No Hafner's stress, only gravitationally induced forces.
% function [Pxx,Pyy,Pxy] = ambient_field(x,y)
% Ridge topography (a slope of alpha degrees) with gravity and water
% pressure in addition to tectonic loads defined by W.Hafner
% (Bulletin of the Geological Society of America, vol.62, 1951, page 392).
% Calculates the ambient field given the x and y coordinates of a point
% The tectonic shear stress is zero at the ridge base.
% The positive y-axis points down.

% y0 = the depth from the seafloor to the ridge summit (m)
% y1 = the depth to the flat seafloor from the ridge summit (m)


A = (alpha/180)*pi;
W = L/4;

y1 = dm*m*sin(A);          % y1 = depth to the flat seafloor from the ridge summit (m)

PwI_a = (abs(x-W)*tan(A)+y0)*rhow*g;  % Water pressure on the ridge slope but below y = 0 in the ridge
region, Positive value
PwI_b = y*rhow*g;          % Water pressure above the ridge slope but below y = 0 in the ridge region,
Positive value
PrI = (y-y0-tan(A)*abs(x-W))*rhob*g; % Rocke pressure below the ridge slope in the ridge region, Positive
value
PwII_a = (y0+y1)*rhow*g;        % Water pressure on the flat seafloor outside of the ridge region due to
water y < 0, Positive value
PwII_b = y*rhow*g;
PrII = (y-y0-y1)*rhob*g;   % Rock pressure below the flat seafloor outside of the ridge, Positive value

% % % % % W.Hafner Stresses are set to zeros % % % % %
sizeXY = size(x);
PxxH = zeros(size(x));     % Sxx in Hafner's paper
PyyH = zeros(size(x));     % Syy in Hafner's paper
PxyH = zeros(size(x));     % Sxy in Hafner's paper

% % % % % % % %% % % %% % % %% % % %% % % %% % % %% % % %

Pxx = NaN*ones(size(x));
Pyy = NaN*ones(size(x));
Pxy = NaN*ones(size(x));

limit_i = sizeXY(1) + 1;
```

```
limit_j = sizeXY(2) + 1;

i=1 ;
j=1 ;
while i< limit_i
   i;
   while j<limit_j
      j;
      if abs(x(i,j) - W) < dm*m*cos(A)          % Within the ridge area along the x-axis
         if y(i,j) > (abs(x(i,j)-W))*tan(A) + y0
            if y(i,j) < y0 + y1                 % Within the ridge triangle
               Pyy(i,j) = Pwl_a(i,j) + Prl(i,j);
               Pxx(i,j) = Pwl_a(i,j);
               Pxy(i,j) = 0;
            else                                % In the crust
               Pyy(i,j) = Pwl_a(i,j) + Prl(i,j) + PyyH(i,j);
               Pxx(i,j) = PxxH(i,j);
               Pxy(i,j) = PxyH(i,j);
            end
         else                                   % In water
            Pyy(i,j) = Pwl_b(i,j);
            Pxx(i,j) = Pyy(i,j);
            Pxy(i,j) = 0;
         end
      else   % Otuside of the ridge area along the x-axis
         if y(i,j) > y0 + y1                    % In the crust
            Pyy(i,j) = PwlI_a + PrlI(i,j) + PyyH(i,j);
            Pxx(i,j) = PxxH(i,j);
            Pxy(i,j) = PxyH(i,j);
         else                                   % In water
            Pyy(i,j) = PwlI_b(i,j);
            Pxx(i,j) = Pyy(i,j);
            Pxy(i,j) = 0;
         end
      end
      j=j+1;
   end
   i=i+1;
   j=1;
end
%%%%%%%%%%%%%%%%%%%%%%%%%%%%%%%%%%%%%%%%%%%%%%%%%%%%%%%%%%%%%%%
%%%%%%%%%%%%%%%%%%%%%%%%%%%%%%%%%%%%%%%%%%%
function [Pxx,Pyy,Pxy] = f_6c(x,y,rhow,rhob,y0,alpha,dm,m,g,c,AH,BH,L)
% function [Pxx,Pyy,Pxy] = ambient_field(x,y)
% make ambient_field zeros
Pxx = zeros(size(x));
Pyy = zeros(size(x));
Pxy = zeros(size(x));

%%%%%%%%%%%%%%%%%%%%%%%%%%%%%%%%%%%%%%%%%%%%%%%%%%%%%%%%%%%%%%%
%%%%%%%%%%%%%%%%%%%
function theta=angp(SIGxx,SIGyy,SIGxy)
% function angp.  Calculates a principal stress orientation
theta = 0.5*atan2(SIGxy,(SIGxx-SIGyy)/2);
%%%%%%%%%%%%%%%%%%%%%%%%%%%%%%%%%%%%%%%%%%%%%%%%%%%%%%%%%%%%%%%
%%%%%%%%%%%%%%%%%%%%%%%%%%%%%%%%%%%%%%%%%%%
function [Uxsv,Uysv,Uxnv,Uynv,Sxxsv,Syysv,Sxysv,Sxxnv,Syynv,Sxynv] = ...
append1_func(first,last,Uxs,Uys,Uxn,Uyn,Sxxs,Syys,Sxys,Sxxn,Syyn,Sxyn,...
Uxsv,Uysv,Uxnv,Uynv,Sxxsv,Syysv,Sxysv,Sxxnv,Syynv,Sxynv)
% Function to save influence coeffients from twodd.m in column vectors
% by appending new column vectors generated by the first set of
```

```
% calls to coeff to the previously generated column vectors
Uxsv (first:last) = Uxs;
Uysv (first:last) = Uys;
Uxnv (first:last) = Uxn;
Uynv (first:last) = Uyn;
Sxxsv (first:last) = Sxxs;
Syysv (first:last) = Syys;
Sxysv (first:last) = Sxys;
Sxxnv (first:last) = Sxxn;
Syynv (first:last) = Syyn;
Sxynv (first:last) = Sxyn;
%%%%%%%%%%%%%%%%%%%%%%%%%%%%%%%%%%%%%%%%%%%%%%%%%%%%%%%
%%%%%%%%%%%%%%%%%%%%%%%%%%%%%%%%%%%%
function mean=ave(SIGxx,SIGyy,SIGxy)
mean = (SIGxx+SIGyy)/2;
%%%%%%%%%%%%%%%%%%%%%%%%%%%%%%%%%%%%%%%%%%%%%%%%%%%%%%%
%%%%%%%%%%%%%%%%%%%%%%%%%%%%%%%%%%%%
function [Uxs,Uys,Uxn,Uyn,Sxxs,Syys,Sxys,Sxxn,Syyn,Sxyn] = ...
coeff_func(x,y,xe,ye,a,COSBe,SINBe,CON,CONS,PR1,PR2,Sd,Nd)
%  This is the MATLAB function version of SUBROUTINE COEFF from TWODD
%  It calculates the xy stress and displacement components
%  at all points (x,y) in an observation array
%  due to unit normal and unit shear displacement
%  discontinuities at element j(xe,ye).

% Define trig functions and coordinates pertaining to the element
% and create arrays of the same size as the observation array
unit = ones(size(x));
COS2Be = (COSBe.*COSBe-SINBe.*SINBe).*unit;
SIN2Be = (2.*SINBe.*COSBe).*unit;
COSB2e = (COSBe.*COSBe).*unit;
SINB2e = (SINBe.*SINBe).*unit;
xe = xe.*unit;
ye = ye.*unit;

% Calculate coordinates of observation points in reference frame
% centered at the element and oriented along the element.
% The transformation requires a translation and a rotation
Xb = (x-xe).*COSBe + (y-ye).*SINBe;
Yb = -(x-xe).*SINBe + (y-ye).*COSBe;
% Flag all observation points for which Yb is not 0
i1 = find(Yb);
% Flag any observation points on the element
i2 = find(Yb == 0 & abs(Xb) < a);

% Find squares of the distances from obs. pts. to element ends
R1S = (Xb-a).*(Xb-a) + Yb.*Yb;
R2S = (Xb+a).*(Xb+a) + Yb.*Yb;

%  Calculate intermediate functions F
FL1 = 0.5.*log(R1S);
FL2 = 0.5.*log(R2S);
FB2 = CON.*(FL1-FL2);
% FB3 = 0 for pts colinear with element, CON*pi for pts. on element
% FB3 = difference of arc tangents for all other pts.
FB3 = zeros(size(x));
FB3(i1) =  -1.*CON.*(atan((Xb(i1)+a)./Yb(i1)) - atan((Xb(i1)-a)./Yb(i1)));
FB3(i2) = CON.*pi.*ones(size(i2));
FB4 = CON.*(Yb./R1S - Yb./R2S);
FB5 = CON.*((Xb-a)./R1S - (Xb+a)./R2S);
FB6 = CON.*(((Xb-a).^2 -Yb.*Yb)./R1S.^2 - ((Xb+a).^2-Yb.*Yb)./R2S.^2);
```

```
FB7 = 2.*CON.*Yb.*((Xb-a)./R1S.^2 - (Xb+a)./R2S.^2);

% Calculate DISPLACEMENT components due to unit SHEAR disp. discontinuity
Uxs = -PR1.*SINBe.*FB2 + PR2.*COSBe.*FB3 + Yb.*(SINBe.*FB4-COSBe.*FB5);
Uys =  PR1.*COSBe.*FB2 + PR2.*SINBe.*FB3 - Yb.*(COSBe.*FB4+SINBe.*FB5);

% Calculate DISPLACEMENT components due to unit NORMAL disp. discontinuity
Uxn = -PR1.*COSBe.*FB2 - PR2.*SINBe.*FB3 - Yb.*(COSBe.*FB4+SINBe.*FB5);
Uyn = -PR1.*SINBe.*FB2 + PR2.*COSBe.*FB3 - Yb.*(SINBe.*FB4-COSBe.*FB5);

% Calculate STRESS components due to unit SHEAR disp. discontinuity
Sxxs = CONS.*(2.*COSB2e.*FB4 + SIN2Be.*FB5 + Yb.*(COS2Be.*FB6-SIN2Be.*FB7));
Syys = CONS.*(2.*SINB2e.*FB4 - SIN2Be.*FB5 - Yb.*(COS2Be.*FB6-SIN2Be.*FB7));
Sxys = CONS.*(SIN2Be.*FB4 - COS2Be.*FB5 + Yb.*(SIN2Be.*FB6 + COS2Be.*FB7));

% Calculate STRESS components due to unit NORMAL displacement discontinuity
Sxxn = CONS.*(-FB5 + Yb.*(SIN2Be.*FB6 + COS2Be.*FB7));
Syyn = CONS.*(-FB5 - Yb.*(SIN2Be.*FB6 + COS2Be.*FB7));
Sxyn = CONS.*(-Yb.*(COS2Be.*FB6 - SIN2Be.*FB7));

% Multiply the components by the shear and normal displacement
% discontintuities. For the first pass through coeff, Sd=Nd=1.
Uxs = Sd*Uxs;
Uys = Sd*Uys;
Uxn = Nd*Uxn;
Uyn = Nd*Uyn;
Sxxs = Sd*Sxxs;
Syys = Sd*Syys;
Sxys = Sd*Sxys;
Sxxn = Nd*Sxxn;
Syyn = Nd*Syyn;
Sxyn = Nd*Sxyn;
%%%%%%%%%%%%%%%%%%%%%%%%%%%%%%%%%%%%%%%%%%%%%%%%%%%%%%%%%%%%
%%%%%%%%%%%%%%%%%%%%%%%%%%%%%%%%%%%%%%%%%%%%
function [SINNB,COSSB,SINN2B,COSS2B,SINNB2,COSSB2] = ...
dircos1_func(SINB,COSB,SIN2B,COS2B,SINB2,COSB2,NUM)
% function to calculate direction cosine matrices
% for stress transformations
%axpx = cos(x'x)                    = cos(thetap - theta)
%axpy = cos(x'y) = sin(x'x) = sin(thetap - theta)
%aypx = cos(y'x) = -sin(x'x)
%aypy = cos(y'y) = cos(x'x)
% cos(A-B) = cosA*cosB + sinA*sinB
% sin(A-B) = sinA*cosB - cosA*sinB

%axpx = COSB*(COSB') + SINB*(SINB');
%axpy = COSB*(COSB') + SINB*(SINB');
%aypx = -aypx;
%aypy = axpx;

SINNB = SINB*(ones(1,NUM));
COSSB = COSB*(ones(1,NUM));
SINN2B = SIN2B*(ones(1,NUM));
COSS2B = COS2B*(ones(1,NUM));
SINNB2 = SINB2*(ones(1,NUM));
COSSB2 = COSB2*(ones(1,NUM));
%%%%%%%%%%%%%%%%%%%%%%%%%%%%%%%%%%%%%%%%%%%%%%%%%%%%%%%%%%%%
%%%%%%%%%%%%%%%%%%%%%%%%%%%%%%%%%%%%%%%%%%%%
function [Uxsv,Uysv,Uxnv,Uynv,Sxxsv,Syysv,Sxysv,Sxxnv,Syynv,Sxynv] = set1_func(nobs)
% Function to dimension the vectors storing the influence coefficients
% from the first set of calls to coeff
```

```
Uxsv  = zeros(nobs,1);
Uysv  = Uxsv;
Uxnv  = Uxsv;
Uynv  = Uxsv;
Sxxsv  = Uxsv;
Syysv  = Uxsv;
Sxysv  = Uxsv;
Sxxnv  = Uxsv;
Syynv  = Uxsv;
Sxynv  = Uxsv;
%%%%%%%%%%%%%%%%%%%%%%%%%%%%%%%%%%%%%%%%%%%%%%%%%%%%%%%%%%%
%%%%%%%%%%%%%%%%%%%%%%%%%%%%%%%%%%%%%%%%%
function S1=sig1(Sxx,Syy,Sxy)
% function S1=sig1(SIGxx,SIGyy,SIGxy)
% Calculates the most tensile 2-D principal stress magnitude
% Input parameters
% Sxx = sigma xx
% Syy = sigma yy
% Sxy = sigma xy
% Output parameter
% S1 = most tensile principal stress
% Example
% S1=sig1(4,-4,3)

S1 = (Sxx+Syy)/2 + sqrt( ((Sxx-Syy)/2).^2 + Sxy.^2);
%%%%%%%%%%%%%%%%%%%%%%%%%%%%%%%%%%%%%%%%%%%%%%%%%%%%%%%%%%%
%%%%%%%%%%%%%%%%%%%%%%%%%%%%%%%%%%%%%%%%%
function S2=sig2(Sxx,Syy,Sxy)
% function S1=sig2(Sxx,Syy,Sxy)
% Calculates the most tensile 2-D principal stress magnitude
% Input parameters
% Sxx = sigma xx
% Syy = sigma yy
% Sxy = sigma xy
% Output parameter
% S1 = most tensile principal stress
% Example
% S1=sig2(4,-4,3)

S2 = (Sxx+Syy)/2 - sqrt( ((Sxx-Syy)/2).^2 + Sxy.^2);
%%%%%%%%%%%%%%%%%%%%%%%%%%%%%%%%%%%%%%%%%%%%%%%%%%%%%%%%%%%
%%%%%%%%%%%%%%%%%%%%%%%%%%%%%%%%%%%%%%%%%
function [Uxs,Uxn,Uys,Uyn,Sxxs,Sxxn,Syys,Syyn,Sxys,Sxyn] = ...
square1_func(Uxsv,Uxnv,Uysv,Uynv,Sxxsv,Sxxnv,Syysv,Syynv,Sxysv,Sxynv,dimx,dimy)
% function to turn column vectors into square matrices
% and then clear the unneeded column vectors
Uxs = reshape(Uxsv,dimx,dimy);
Uxn = reshape(Uxnv,dimx,dimy);
Uys = reshape(Uysv,dimx,dimy);
Uyn = reshape(Uynv,dimx,dimy);
Sxxs = reshape(Sxxsv,dimx,dimy);
Sxxn = reshape(Sxxnv,dimx,dimy);
Syys = reshape(Syysv,dimx,dimy);
Syyn = reshape(Syynv,dimx,dimy);
Sxys = reshape(Sxysv,dimx,dimy);
Sxyn = reshape(Sxynv,dimx,dimy);
%%%%%%%%%%%%%%%%%%%%%%%%%%%%%%%%%%%%%%%%%%%%%%%%%%%%%%%%%%%
%%%%%%%%%%%%%%%%%%%%%%%%%%%%%%%%%%%%%%%%%
function [Ux,Uy,Sxx,Syy,Sxy] = ...
square2_func(Uxsv,Uxnv,Uysv,Uynv,Sxxsv,Sxxnv,Syysv,Syynv,Sxysv,Sxynv,NUM2,NUM,dimx,dimy)
% Function square2 to help turn column vectors into square matrices
```

```
% and clears unneeded column vectors.

% First turn the entering column vectors into matrices,
% where the number of rows is the number of observation points (NUM2)
% and the number of columns equals the number of elements.
% The column vectors are cleared once they are done with.
Uxs = reshape(Uxsv,NUM2,NUM);
Uxn = reshape(Uxnv,NUM2,NUM);
Uys = reshape(Uysv,NUM2,NUM);
Uyn = reshape(Uynv,NUM2,NUM);
Sxxs = reshape(Sxxsv,NUM2,NUM);
Sxxn = reshape(Sxxnv,NUM2,NUM);
Syys = reshape(Syysv,NUM2,NUM);
Syyn = reshape(Syynv,NUM2,NUM);
Sxys = reshape(Sxysv,NUM2,NUM);
Sxyn = reshape(Sxynv,NUM2,NUM);

% Next, sum the entries in each row to superpose
% the contributions of all the elements.
% This step will yield column vectors
% See p. 488 of the Matlab manual for this
Uxs = sum(Uxs')';
Uxn = sum(Uxn')';
Uys = sum(Uys')';
Uyn = sum(Uyn')';
Sxxs = sum(Sxxs')';
Sxxn = sum(Sxxn')';
Syys = sum(Syys')';
Syyn = sum(Syyn')';
Sxys = sum(Sxys')';
Sxyn = sum(Sxyn')';

% Now, reshape the column vectors into matrices
% that have the dimensions of the observation grid,
% adding the contributions from the shear and
% normal displacement discontinuities
Ux = reshape(Uxs,dimx,dimy) + reshape(Uxn,dimx,dimy);
Uy = reshape(Uys,dimx,dimy) + reshape(Uyn,dimx,dimy);
Sxx = reshape(Sxxs,dimx,dimy) + reshape(Sxxn,dimx,dimy);
Syy = reshape(Syys,dimx,dimy) + reshape(Syyn,dimx,dimy);
Sxy = reshape(Sxys,dimx,dimy) + reshape(Sxyn,dimx,dimy);
%%%%%%%%%%%%%%%%%%%%%%%%%%%%%%%%%%%%%%%%%%%%%%%%%%
%%%%%%%%%%%%%%%%%%%%%%%%%%%%%%%%
function tau=taumax(Sxx,Syy,Sxy)
% function tau=taumax(Sxx,Syy,Sxy)
% Calculates maximum shear stress magnitude (2-D)
% Input parameters
% Sxx = sigma xx
% Syy = sigma yy
% Sxy = sigma xy
% Output parameter
% tau = maximum shear stress
% Example
% tau=taumax(4,-4,3)

tau = sqrt( ((Sxx-Syy)/2).^2 + Sxy.^2);
%%%%%%%%%%%%%%%%%%%%%%%%%%%%%%%%%%%%%%%%%%%%%%%%%%
%%%%%%%%%%%%%%%%%%%%%%%%%%%%%%%%
```

```
% Code 5
% base_data
% the following contains the basic input required to run TWODD in this
% analysis
%
% AMBIENT FIELD
% making boundary element for a ridge topography
clear
a = 3;            % slope of the ridge, in positive degrees
dm = 100;         % boundary element size for a ridge topography
dp1 = 1000;       % number of boundary element along the ridge slope
dp2 = 10*1000;    % number of boundary element along the ridge base
S = 0;            % shear stress
rhow = 1000;      % density of water (kg/km3)
g = -9.8;         % gravitational acceleration

m = 100;
p1 = 50;
p2 = 10;
y0 = 2500;        % depth from the sea surface to the ridge summit (m)
L = 200*1000;     % wavelength in Hafner's traction (m)
W = L /4;

[M] = make_b_datR_WP_f6_7b_2(a,dm,dp1,dp2,S,rhow,g,m,p1,p2,y0,L);
b_dat=M;

% making observation points
xmin = -500 + W;
xmax = 5000 + W;
dx = 100;
ymin = 100 + y0;
ymax = 4000 + y0;
dy = 100;
xgrid = xmin:dx:xmax;
ygrid = ymin:dy:ymax;
[X,Y] = meshgrid(xgrid,ygrid);

% eliminating unnecessary observation points
[X,Y] = eliminate_obs_point_f6_7b_2(X,Y,a,m,dm,L,y0);

% running twodd
e_dat = [0.25  2.5*10^10];

rhob = 2500;          % density of basalt (kg/m3)
alpha = a;
c = 5000;             % depth to the moho in m
AH = 10^(3);          % Hafner's A
BH = 10^(8);          % Hafner's B
```

```
% Code 6
% Other functions

%%%%%%%%%%%%%%%%%%%%%%%%%%%%%%%%%%%%%%%%%%%%%%%%%%%%%%%%%%
%%%%%%%%%%%%%
function [M] = make_b_datR_WP_f6_7b_2(a,dm,dp1,dp2,S,rhow,g,m,p1,p2,y0,L)

% Make a boundary element in a ridge shape with a slope of a 'a' angle in
% degree with water pressure (rhow*g*y).
% One ridge flank consists of m elements with a size of d. The ridge base
% consists of p elements with a size of d.
% The ridge summit is offset for W (L/4) to position the summit at 90 degrees.
% The ridge summit is at y0 m.

% boundary element size for dm and dp1, dp2 are not equal , dp2 > dp1 >= dm

A = (a/180)*pi;
dx = dm*cos(A);
dy = dm*sin(A);

M=zeros((2*(m+p1+p2)),6);
M(:,5)=[S];

% begining point at the corner of the ridge flank and ridge base on the right side of the ridge
xbeg = dx*m + W;
ybeg = dy*m + y0;

% ridge base on the right side of the ridge and p2 portion
i = p2-1;
q = 1;
for i = (p2-1):-1:0
   M(q,1) = [xbeg+dp1*p1+dp2*(i+1)];
   M(q,2) = [ybeg];
   M(q,3) = [xbeg+dp1*p1+dp2*i];
   M(q,4) = [ybeg];
   M(q,6) = [rhow*g*(m*dy + y0)];
   i = i-1;
   q = q+1;
end

% the ridge base on the right side of the ridg and p1 portion
i = p1-1;
q = p2+1;
for i = (p1-1):-1:0
   M(q,1) = [xbeg+dp1*(i+1)];
   M(q,2) = [ybeg];
   M(q,3) = [xbeg+dp1*i];
   M(q,4) = [ybeg];
   M(q,6) = [rhow*g*(m*dy + y0)];
   i = i-1;
   q = q+1;
end
% the ridge flank on the right side of the ridge
i = 0;
j = p2+p1+1;
for i = 0:(m-1)
   M(j,1) = [xbeg-dx*i];
   M(j,2) = [ybeg-dy*i];
   M(j,3) = [xbeg-dx*(i+1)];
   M(j,4) = [ybeg-dy*(i+1)];
   M(j,6) = [rhow*g*(dm*(m-(i+0.5))*sin(A)+y0)];
```

```
    i = i-1;
    j = j+1;
end

% % the ridge flank on the left side of the ridge
i = 0;
k = m+p1+p2+1;
for i = 0:m-1
    M(k,1) = [xbeg-m*dx-(dx*i)];
    M(k,2) = [ybeg-m*dy+dy*i];
    M(k,3) = [xbeg-m*dx-dx*(i+1)];
    M(k,4) = [ybeg-m*dy+dy*(i+1)];
    M(k,6) = [rhow*g*(dm*(i+0.5)*sin(A)+y0)];
    i = i+1;
    k = k+1;
end

% % the ridge base on the left side of the ridge and p1 portion
i = 0;
q = 2*m+p1+p2+1;
for i = 0:p1-1
    M(q,1) = [xbeg-(dx*m*2)-(dp1*i)];
    M(q,2) = [ybeg];
    M(q,3) = [xbeg-(dx*m*2)-dp1*(i+1)];
    M(q,4) = [ybeg];
    M(q,6) = [rhow*g*(m*dy+y0)];
    i = i+1;
    q = q+1;
end

% % the ridge base on the left side of the ridge and p2 portion
i = 0;
q = 2*(m+p1)+p2+1;
for i = 0:p2-1
    M(q,1) = [xbeg-(dx*m*2)-dp1*p1-(dp2*i)];
    M(q,2) = [ybeg];
    M(q,3) = [xbeg-(dx*m*2)-dp1*p1-dp2*(i+1)];
    M(q,4) = [ybeg];
    M(q,6) = [rhow*g*(m*dy+y0)];
    i = i+1;
    q = q+1;
end

%%%%%%%%%%%%%%%%%%%%%%%%%%%%%%%%%%%%%%%%%%%%%%%%%%%%%%%%%%%%
%%%%%%%%%%%%%%
function [X,Y] = eliminate_obs_point_f6_7b_2(X,Y,a,m,dm,L,y0)
% change any observation points which overlap with the boundary element into NaN
% used for a boundary element made with make_b_datR_WP_f6_7b_2.m

A = (a/180)*pi;
W = L/4;

sizeXY = size (X);
limit_i = sizeXY(1) + 1;
limit_j = sizeXY(2) + 1;

i=1;
j=1;
while i< limit_i
    i;
    while j<limit_j
```

```
        j;
        if (abs(X(i,j)-W)) < dm*m*cos(A)
            if Y(i,j) < (abs(X(i,j)-W))*tan(A) + y0 + dm/2
                X(i,j) = [NaN];
                Y(i,j) = [NaN];
                j=j+1;
            else
                j=j+1;
            end
        else
            if Y(i,j) < dm*m*sin(A) + y0 +dm/2
                X(i,j) = [NaN];
                Y(i,j) = [NaN];
                j=j+1;
            else
                j=j+1;
            end
        end
    end
    i=i+1;
    j=1;
end
```

REFERENCES

Baker, E. T., G. J. Massoth, and R. A. Feely, Cataclysmic venting on the Juan de Fuca Ridge, Nature, 329, 149-151, 1987.

Baker, E. T., W. Lavelle, R. A. Feely, G. J. Massoth, and S. L. Walker, Episodic venting on the Juan de Fuca Ridge, Journal of Geophysical Research, 94, 9237-9250, 1989.

Ballard, R. D. and J. G. Moore, Photographic atlas of the Mid-Atlantic Ridge rift valley, Springer-Verlag, New York, 1977.

Barth, G. A. and J. C. Mutter, Variability in oceanic crustal thickness and structure: Multichannel seismic reflection results from the northern East Pacific Rise, Journal of Geophysical Research, 101, 17,951-975, 1996.

Carbotte, S. and K.C. Macdonald, East Pacific Rise 8°-10°30'N: Evolution of ridge segments and discontinuities from SeaMARC II and three-dimensional magnetic studies, Journal of Geophysical Research, 97, 6959-6982, 1992.

Chadwick, W. W. Jr. and R. W. Embley, Lava flows from a mid-1980s submarine eruption on the Cleft segment, Juan de Fuca Ridge, Journal of Geophysical Research, 99, 4761-4776, 1994.

Chadwick, W. W. Jr. and R. W. Embley, Graven formation associated with recent dike intrusions and volcanic eruptions on the mid-ocean ridge, Journal of Geophysical Research, 103, 9,807-9825, 1998.

Chadwick, W.W., T. K. P. Gregg, R. W. Embley, Submarine lineated sheet flows: A unique lava morphology formed on subsiding lava ponds, Bulletin of Volcanology, 61, 194-206, 1999

Christeson, G.L., G. M. Purdy, and G. J. Fryer, Structure of young upper crust at the East Pacific Rise near 9°30'N, Geophysical Research Letters, 19, 1945-1048, 1992.

Christeson, G.L., G. M. Kent, G. M. Purdy, and R. S. Detrick, Extrusive thickness variability at the East Pacific Rise, 9°-10°N: Constraints from seismic techniques, Journal of Geophysical Research, 101, 2859-2873, 1996.

Cochran, J. R., D. J. Fornari, B. J. Coakley, R. Herr, and M. A. Tivey, Continuous near-bottom gravity measurements made with a BGM-3 gravimeter in DSV *Alvin* on the East Pacific Rise crest near 9°31'N and 9°50'N, Journal of Geophysical Research, 104, 10,841-861, 1999.

Crouch, S. L., and A. M. Starfield, Boundary element methods in solid mechanics, Allen and Unwin, London, 1983.

DeMets, C, R. G. Gordon, D. F. Argus, and S. Stein, Effect of recent revisions to the geomagnetic reversal time scale on estimates of current plate motions, Geophysical Research Letters, 21, 2191-2194, 1994.

Detrick, R. S., P. Buhl, E. Vera, J. Mutter, J. Orcutt, J. Madsen, and T. Brocher, Multi-channel seismic imaging of a crustal magma chamber along the East Pacific Rise, Nature, 326, 35-41, 1987.

Duffield W.A., Christiansen R.L., Koyanagi R.Y., and Peterson D.W., Storage, migration, and eruption of magma at Kilauea Volcano, Hawaii, 1971-1972, Journal of Volcanology & Geothermal Research 13, 273-307, 1982.

Dunn, R.A., and D. R. Toomey, Three-dimensional seismic structure and physical properties of the crust and shallow mantle beneath the East Pacific Rise at 9°30'N, Journal of Geophysical Research, 105, 23,537-555, 2000.

Eberle, M. A., and D. W. Forsyth, An alternative, dynamic model of the axial topographic high at fast spreading ridges, Journal of Geophysical Research, 103, 12,309-320, 1998.

Edwards, M. H., The morphotectonic fabric of the East Pacific Rise: Implications for fault generation and crustal accretion, Ph.D. thesis, Columbia University, New York, 1991.

Embley, R. W., W. W. Jr. Chadwick, M. R. Perfit, and E. T. Baker, Geology of the northern Cleft segment, Juan de Fuca Ridge: Recent lava flows, sea-floor spreading, and the formation of magaplumes, Geology, 19, 771-775, 1991.

Engels, J. L., M. H. Edwards, D. J. Fornari, M. R. Perfit and J. R. Cann, A new model for submarine volcanic collapse formation, Geochemistry Geophysics Geosystems, 4, 2003.

ENVI (version 4) [Computer Software] Boulder, CO: Research Systems, Inc., 2004.

Fialko, Y., On origin of near-axis volcanism and faulting at fast spreading mid-ocean ridges, Earth and Planetary Science Letters, 190, 31-39, 2001.

Fornari, D. J., R. M. Haymon, M. H. Edwards, and K. C. Macdonald, Volcanic and tectonic characteristics of the East Pacific Rise crest 9°09'N to 9°54'N: Implications for fine-scale segmentation of the plate boundary, EOS Transactions. AGU, 71, 625, 1990.

Fornari, D. J., R. M. Haymon, M.R. Perfit, T.K. Gregg, and M. H. Edwards, Axial summit trough of the East Pacific Rise 9°-10°N: Geological characteristics and evolution of the axial zone on fast spreading mid-ocean ridges, Journal of Geophysical Research, 103, 9827-9855, 1998.

Francis, E. H., Emplacement mechanism of late Carboniferous tholeiite sills in northern Britain, Journal of Geological Society of London, 139, 1-20, 1982.

Geyer, R. A., Handbook of geophysical exploration at sea, CRC Press Inc., Boca Raton, 1992.

Goldstein, S. J., Perfit, M. R., Batiza, R., Fornari., D. J., and Murrell, M. T., Off-axis volcanism at the East Pacific Rise detected by uranium-series dating of basalts, Nature, 367, 1994.

Gregg, T.K., and J. H. Fink, Quantification of submarine lava-flow morphology through analog experiments, Geology, 23, 73-76, 1995.

Gregg, T.K., D. J. Fornari, M. R. Perfit, R. M. Haymon, and J. H. Fink, Rapid emplacement of a mid-ocean ridge lava flow on the East Pacific Rise at 9°46'-51'N, Earth and Planetary Science Letters, 144, E1-E7, 1996.

Gregg, T.K., and J. H. Fink, A laboratory investigation into the effects of slope on lava flow morphology, Journal of Volcanology and Geothermal Research, 96, 145-159, 2000.

Hafner, W., Stress distributions and faulting, Bulletin of the Geological Society of America, 62, 373-398, 1951.

Harding, A. J., G. M. Kent, and J. A. Orcutt, A multichannel seismic investigation of upper crustal structure at 9°N on the East Pacific Rise: Implications for crustal accretion, Journal of Geophysical Research, 98, 13,925-13,944, 1993.

Haymon, R. M., Growth history of hydrothermal black smoker chimneys, Nature, 301, 695-698, 1983.

Haymon, R. M., D. J. Fornari, M. H. Margo, S. Carbotte, D. Wright, and K. C. Macdonald, Hydrothermal vent distribution along the East Pacific Rise crest (9°09'-54'N) and its relationship to magmatic and tectonic processes on fast-spreading mid-ocean ridges, EOS, 104, 513-104,534, 1991.

Haymon, R. M., D. J. Fornari, K., L. Von Damm, M. D. Lilley, M. R. Perfit, J. M. Edmond, W. C. Shanks, III, R. A. Lutz, J. M. Grebmeier, S. Carbotte, D. Wright, E. McLaughlin, M. Smith, N. Beedle, and E. Olson, Volcanic eruption of the mid-ocean ridge along the East Pacific Rise crest at 9°45-52'N: Direct submersible observations of seafloor phenomena associated with an eruption event in April, 1991, Earth and Planetary Science Letters, 119, 85-101, 1993.

Herron, T. J., Lava flow layer-East Pacific Rise, Geophysical Research Letter, 9, 17-20, 1982.

Hooft, E. E., H. Schouten, and R. S. Detrick, Constraining crustal emplacement processes from the variation in seismic layer 2A thickness at the East Pacific Rise, Earth and Planetary Science Letters, 142, 289-309, 1996.

Houtz, R. and J. I. Ewing, Upper crustal structure as a function of plate age, Journal of Geophysical Research, 81, 2490-2498, 1976.

Kent, G. M., A. J. Harding, and J. A. Orcutt, Distribution of magma beneath the East Pacific Rise between the Clipperton transform and the 9°17'N deval from forward modeling of common depth point data, Journal of Geophysical Research, 98, 13,945-969, 1993.

Kent, G. M., A. J. Harding, J. A. Orcutta, R. S. Detrick, J. C., Mutter, and P. Buhl, Uniform accretion of oceanic-crust south of the Garretta transform at 14°15'S on the East Pacific Rise, Journal of Geophysical Research, 99, 9097-9116, 1994.

Kiltgord, K. D. and J. Mammerick, Northern East Pacific Rise: Magnetic anomaly and bathymetric framework, Journal of Geophysical Research, 87, 6725-6750, 1982.

Kurras, G. J., D. J. Fornari, M. H. Edwards, M. R. Perfit, and M. C. Smith, Volcanic Morphology of the East Pacific Rise Crest 9°49'-52': Implications for volcanic emplacement processes at fast-spreading mid-ocean ridges, Marine Geophysical Researches, 21, 23-41, 2000.

Langley, J. S., Processes of normal faulting and surface deformation along the Koae fault system, Hawaii, M.S. Thesis, University of Hawaii, 2000.

Lipman P.W. and N. G. Banks, Aa flow dynamics, Mauna Loa 1984 (Hawaii), US Geological Survey Professional Paper, 1350, 1527-1567, 1987

Lonsdale, P, Structural geomorphology of a fast spreading rise crest: The East Pacific Rise near 3°25'S, Marine Geophysical Researches, 3, 251-293, 1977.

Macdonald, K. C., K. Becker, F. N. Spiess, R. D. Ballard, Hydrothermal heat flux of the 'Black Smoker' vents on the East Pacific Rise, Earth and Planetary Science Letters, 48, 1-7, 1980.

Macdonald K.C., Mid-ocean ridges: fine scale tectonic, volcanic and hydrothermal processes within the plate boundary zone, Annual Review of Earth and Planetary Sciences, 10, 155-190, 1982

Macdonald, K. C., D. S. Scheirer, and S. M. Carbotte, Mid-ocean ridges: Discontinuities, segments and giant cracks, Science, 253, 986-994, 1991.

Macdonald, K. C., P. J. Fox, R. T. Alexander, R. Pockalny, and P. Gente, Volcanic growth faults and the origin of Pacific abyssal hills, Nature, 380, 125-129, 1996.

Macdonald, K. C., Linkages between faulting, volcanism, hydrothermal activity and segmentation on fast spreading centers, Buck, W. P., P. T. Delaney, J. A. Karson, and Y. Lagabrielle (Ed.) Geophysical Monograph, 106, 27-45, 1998.

Madsen, J.A., D. W. Forsyth, and R. S. Detrick, A new isostatic model for the East Pacific Rise crest, Journal of Geophysical Research, 89, 9,9997-10,015, 1984.

Martel, S. J. and J. R. Muller, A two-dimensional boundary element method for calculating elastic gravitational stresses in slopes, Pure and Applied Geophysics, 157, 989-1007, 2000.

Martel, S. J., Modeling elastic stresses in long ridges with the displacement discontinuity method, Pure and Applied Geophysics, 157, 1039-1057, 2000.

Mastin, L. G., and D. D. Pollard, Surface deformation and shallow dike intrusion processes at Inyo Craters, Long Valley, California, Journal of Geophysical Research, 93, 13,221-13,235, 1988.

Moore, J. G., Mechanism of formation of pillow lava, American Scientist, 63, 269-277, 1975.

Nicolas, A., F. Boudier, and B. Ildefonse, Variable crustal thickness in the Omen ophiolite: Implication for oceanic crust, Journal of Geophysical Research, 101, 17,941-950, 1996.

O'Neill, J. M. H., Geologic controls on distribution of hydrothermal vents on the superfast-spreading southern East Pacific Rise, M. A. thesis, University of California, Santa Barbara, 1998.

Perfit, M. R., D.J. Fornari, M. C. Smith, J. F. Bender, C. H. Languir, R. M. Haymon, Small-scale spatial and temporal variations in mid-ocean ridge crest magmatic processes, Geology, 22, 375-22,379, 1994.

Perfit, M. R. and W.W. Chadwick, Magmatism at mid-ocean ridges: Constraints from volcanological and geochemical investigations. Buck, W. P., P. T. Delaney, J. A. Karson, and Y. Lagabrielle (Ed.) Geophysical Monograph, 106, 59-115, 1998.

Pollard, D. D. and A. M. Johnson, Mechanics of growth of some laccolithic intrusions in the Henry Mountains, Utah, I; field observations, Gilbert's model, physical properties and flow of the magma, Tectonophysics, 18, 261-309, 1973.

Pollard, D. D. and G. Holzhausen, On the mechanical interaction between a fluid-filled fracture and the earth's surface, Tectonophysics, 53, 27-57, 1979.

Pollard, D. D., P. T. Delaney, P. T. Duffield, E. T. Endo, and A. T. Okamura, Surface deformation in volcanic rift zones, Tectonophysics, 94, 541-584, 1983.

Pollard, D. D. and P. Segall, Theoretical displacements and stresses near fractures in rock: with applications to faults, joints, veins, dikes, and solution surfaces, Fracture Mechanics of Rock, Academic Press Inc. (London) Ltd, 277-349, 1987.

Richer, D. H., Eaton, J. P., Murata, K. J., Ault, W. U., and Krivoy, H. L., Chronological narrative of the 1959-1960 eruption of Kilauea volcano, Hawaii, U.S. Geological Survey Professional Paper, 537-E, 73pp., 1970.

Rosendahl, B. R., Raitt, R. W., Dorman, L. M., Bibee, L. D., Hussong, D. M., and Sutton, G. H., 1976, Evolution of the Oceanic crust 1: Physical Model of the East Pacific Rise Crest derived from seismic refraction data, Journal of Geophysical Research, 81, 5294-5304, 1976.

Rubin, A. M. and D. D. Pollard, Dike-induced faulting in rift zones of Iceland and Afar, Geology, 16, 413-417, 1988.

Rubin, A. M., Dike-induced faulting and graben subsidence in volcanic rift zones, Journal of Geophysical Research, 97, 1839-1858, 1992.

Schouten, H., M. A. Tivey, and D. J. Fornari, AT7-4 Cruise Report, at: http://imina.soest.Hawaii.edu/HMRG/EPR/index.htm under AT7-4 Cruise Report, 2001.

Schouten, H., M. A. Tivey, D. J. Fornari, A. Bradley, P. Johnson, M. Edwards, and T. Kurokawa, Lava transport and accumulation processes on EPR 9°27'N to 10°N: Interpretations based on recent near-bottom sonar imaging and seafloor observations using ABE, Alvin, and a new digital deep sea camera, Eos Transition, AGU, 83(47), Fall Meeting Supplement, Abstract T11C-1262, 2002.

Shah, A. K., and W. R. Buck, Plate bending stresses at axial highs, and implications for faulting behavior, Earth and Planetary Science Letters,

Sigurdsson O., Surface deformation of the Krafla fissure: swarm in two rifting events, Journal of Geophysics - Zeitschrift fur Geophysik 47, 154-159, 1980.

Sinton, J. M., and R. S. Detrick, Mid-ocean ridge magma chambers, Journal of Geophysical Research, 97, 197-216, 1992.

Spiess, F. N. (with RISE project group), East Pacific Rise: hot springs and geophysical experiments, Science, 207, 1421-1433, 1980.

Swanson, D. A., Duffield, W. A., Jackson, D. B., and Peterson, D. W., Chronological narrative of the 1969-71 Mauna Ulu eruption of Kilauea Volcano, Hawaii, U.S. Geological Survey Professional Paper, 1056, 55 pp., 1979.

Talwani, M., C.C. Windisch, and M. G. Langseth, Reykjanes ridge crest: A detailed geophysical study, Journal of Geophysical Research, 76, 463-517, 1976.

Turcotte, D. L. and J. P. Morgan, The physics of magma migration and mantle flow beneath a mid-ocean ridge, Geophysical Monograph, 71, 155-182, 1992.

Vera, E. E. and J. B. Diebold, Seismic imaging of oceanic layer 2A between 9°30'N and 10°N on the East Pacific Rise from two-ship wide-aperture profiles, Journal of Geophysical Research, 99, 3031-3041, 1994.

Von Damm, K. L., S. E. Oosting, R. Kozlowski, Short term chemical and temperature changes in seafloor hydrothermal vents at 9°46.5'N EPR following a volcanic eruption, Nature, 375, 47-50, 1995.

Wessel, P. and W. H. F. Smith, Free software helps map and display data, Eos, Transactions, AGU 72, 445-446, 1991.

Wilson, D. S., D. A. Clague, N. H. Sleep, and J. L. Morton, Implications of magma convection for the size and temperature of magma chambers at fast spreading ridges, Journal of Geophysical Research, 93, 11,974-984, 1988.

White, S. M., K. C. Macdonald, and R. M. Haymon, Basaltic lava domes, lava lakes, and volcanic segmentation on the southern East Pacific Rise, Journal of Geophysical Research, 105, 23,519-23,536, 2000.

White, S. M., R. M. Haymon, D. J. Fornari, M. R. Perfit, and K. C. Macdonald, Correlation between volcanic and tectonic segmentation of fast-spreading ridges: Evidence from volcanic structures and lava flow morphology on the East Pacific Rise at 9°-10°N, Journal of Geophysical Research, 2002.

Wright, D. J., R. M. Haymon, and D. J. Fornari, Crustal fissuring and its relationship to magmatic and hydrothermal processes on the East Pacific Rise crest (9°12' to 54'N), Journal of Geophysical Research, 100, 6097-6120, 1995.

Yoerger, D. R., A. M. Bradley, M. Cormier, W. B. F. Ryan, and B. B. Walden, High resolution mapping of fast spreading mid ocean ridge with the Autonomus Benthic Explorer, Proceedings of the 11th International Symposium on Unmanned Untethered Submersible Technology, Durham, NH, August 1999.

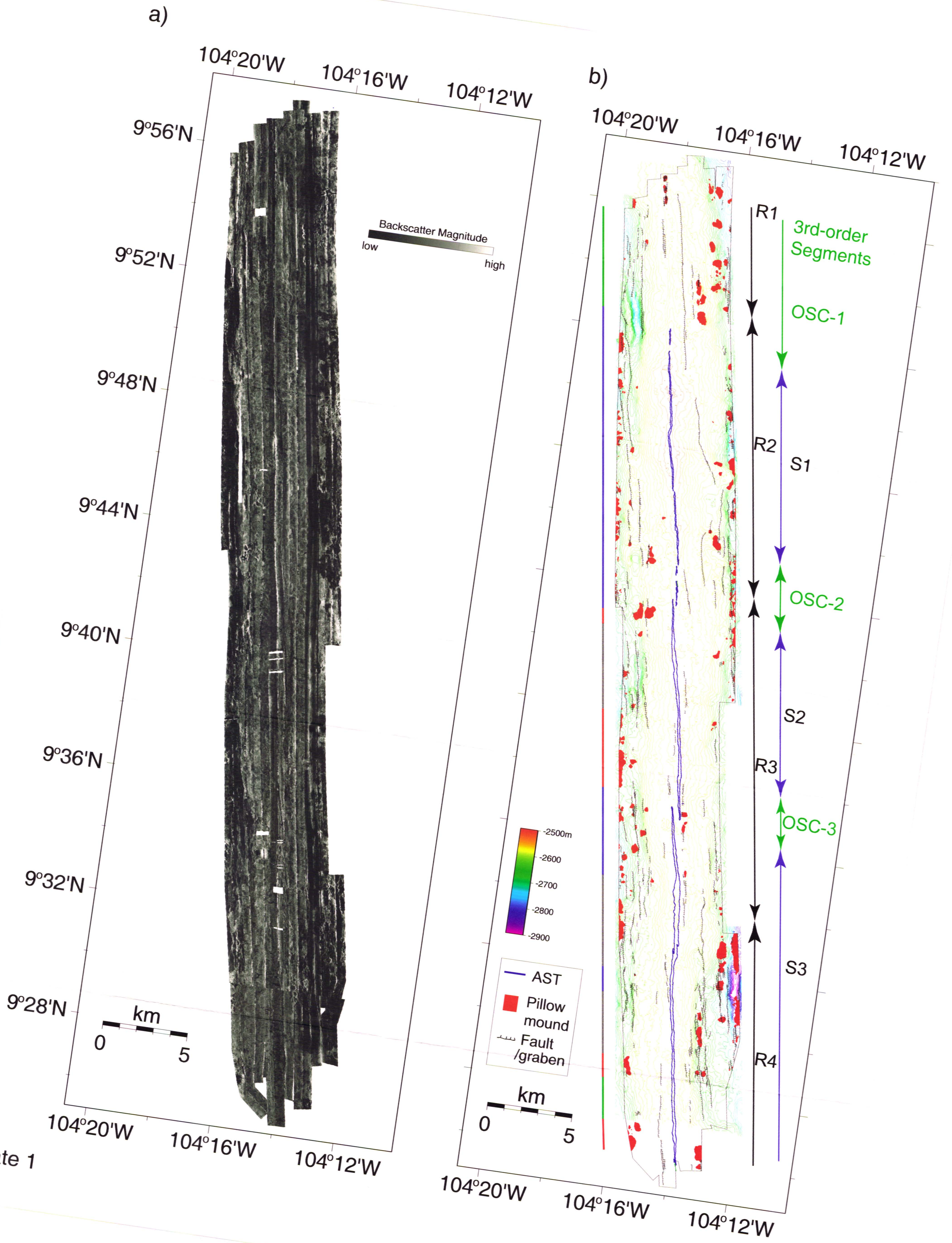

a)
b)
104°20'W
104°16'W
104°12'W
9°56'N
9°52'N
9°48'N
9°44'N
9°40'N
9°36'N
9°32'N
9°28'N
Backscatter Magnitude
low
high
km
0
5
R1
R2
R3
R4
3rd-order
Segments
OSC-1
OSC-2
OSC-3
S1
S2
S3
-2500m
-2600
-2700
-2800
-2900
AST
Pillow mound
Fault /graben

Plate 1